AN ABSTRACT OF THE DISSERTATION OF

Larry A. Gratton for the degree of Doctor of Philosophy in Mathematics presented on August 23, 2005.

Title: Nonuniform Sampling Problems in Computed Tomography.

Abstract approved: Signature redacted for privacy.

Adel Faridani

Two problems involving high-resolution reconstruction from nonuniformly sampled data in x-ray computed tomography are addressed. A technique based on the theorem for sampling on unions of shifted lattices is introduced which exploits the symmetry property in two-dimensional fan beam computed tomography and permits the reconstruction of images with twice the resolution as the standard reconstruction by increasing only the number of views per rotation. An estimate is given for the aliasing error committed in the case of non-bandlimited data. Numerical results are presented which demonstrate the improvement in the quality of images from real and simulated data.

A mathematical framework is presented for analyzing the longitudinal interpolation problem in three-dimensional multislice helical computed tomography. The problem is viewed as a collection of one-dimensional nonuniform but periodic sampling problems. An accurate interpolation formula based on the periodic sampling theorem is introduced. A measure of suitability of a sampling scheme is presented and candidates for so-called preferred helical pitch are identified. Numerical results from simulated data are presented which confirm the theoretical predictions.

Nonuniform Sampling Problems in Computed Tomography

by

Larry A. Gratton

A DISSERTATION

submitted to

Oregon State University

in partial fulfillment of
the requirements for the
degree of

Doctor of Philosophy

Presented August 23, 2005
Commencement June 2006

Doctor of Philosophy dissertation of Larry A. Gratton presented on August 23, 2005

APPROVED:

Signature redacted for privacy.

Major Professor, representing Mathematics

Signature redacted for privacy.

Chair of the Department of Mathematics

Signature redacted for privacy.

Dean of the Graduate School

I understand that my dissertation will become part of the permanent collection of Oregon State University libraries. My signature below authorizes release of my dissertation to any reader upon request.

Signature redacted for privacy.

Larry A. Gratton, Author

ACKNOWLEDGMENTS

The author wishes to express his gratitude to Patrick J. LaRivière and Xiaochuan Pan as well as Steven H. Izen, David P. Rohler and K.L.A. Sastry for their original investigations which inspired this work, and to Frank Natterer for providing insights into the practical aspects of computed tomography. The author expresses sincere appreciation to Adel Faridani for offering a thoughtful and sophisticated view of Applied Mathematics and for his patient guidance along the path of discovery. Finally, the author offers his deepest appreciation to Rebecca, Mathew and James for the love, support and motivation that made this work possible. Thank you.

TABLE OF CONTENTS

LIST OF FIGURES

NONUNIFORM SAMPLING PROBLEMS IN COMPUTED TOMOGRAPHY

1 INTRODUCTION

1.1 Overview

Computed Tomography (CT) refers to the reconstruction of a function from its set of line integrals. The basic problem was solved in principle by J. Radon in 1917. The idea gained new interest with the introduction of diagnostic radiology in the later part of the twentieth century. Here, line integrals model the attenuation of x-rays as they pass through the tissues of the body. In a typical CT scanner, a narrow beam of x-rays illuminate a patient or test object, and the intensity of the transmitted rays is measured by an array of detectors opposite of the x-ray source. Measurements are made for various source position, or views, about the patient or object. Reconstructing the attenuation function from these projection data allows a non-invasive view inside the body of the patient or test object. A three dimensional image may be reconstructed slice by slice from a series of two dimensional projection. The basic problem has been studied extensively and has been extended to integrals over planes, spheres, and arbitrary manifolds. The principles have been applied to a variety of imaging modalities such as MRI (magnetic resonance imaging), emission tomography, electrical impedance tomography, ultrasound, radar, and many others. Advances in technology and the development of new imaging modalities continue to drive the need for sophisticated analysis. The author suggests the text by Nat-

terer [25] for a comprehensive mathematical description of CT. For a more practical treatment, see Kak and Slaney [15]. For a survey of applications of tomography in medical imaging, see Natterer and Wübbeling [28].

Tomographic reconstruction presents many mathematical challenges. Like all inverse problems, CT is inherently ill-posed. Of paramount importance in obtaining a reliable reconstruction are stability and uniqueness. Radon's inversion formula did not lead directly to a stable and practical reconstruction algorithm. The well known filtered back-projection algorithm produces an approximate solution by computing the convolution of the attenuation function with a low-pass filter function. The filter is designed to suppress high frequency information in the data, like that corresponding to sharp boundaries and randomly oscillating noise, that may be amplified during exact reconstruction. The choice of filter effects the resolution of the approximate solution. That is, it effects the ability to accurately reconstruct sharp boundaries and recover the true value of small features in the attenuation function.

We do not measure integrals over all lines intersecting the support of the object. Given a finite set of lines, null functions exist which are not identically zero, but the integral of which is zero for every line in the set. (See e.g. Smith, Solmon, and Wagner [39]) Consequently, we can not uniquely determine the solution of the reconstruction problem from a finite number of measurements. These null functions, however, tend to be high frequency functions and therefore may be suppressed by the proper choice of filter in the filtered back-projection algorithm. Which line integrals should we measure to obtain a desired reconstruction i.e. one with the desired resolution? Sampling theory is a natural tool for answering this question.

The scanning geometry refers to the parameterization of lines over which data are to be measured. The parallel beam scanning geometry is the standard example

in two dimensions. It consists of sets of equispaced parallel lines in a finite number of directions. The divergent beam geometry, or fan beam geometry in two dimensions, is more convenient in practice and involves sets of half lines, or rays, emanating from finitely many source points lying on a curve about the patient or object. A sampling scheme is a particular choice of lines in a given scanning geometry. Classical sampling schemes involve measuring data on a regular grid in the coordinate domain, or uniform sampling. Cormack [2] and Rattey and Lindgren [33] applied the classical sampling theorem to determine sufficient sampling conditions in parallel beam CT and propose so called efficient sampling schemes which recover desired resolution from minimum amount of data. Faridani [6, 9], extended the analysis to generalize efficient schemes in 2D parallel beam geometry. Natterer [26] applied similar analysis in fan beam geometry. Desbat et al. [5] applied similar analysis to three dimensional parallel and fan beam geometries.

In practice we do not often have such freedom in the choice of sampling scheme. Very often physical scanner design and practical constraints such as reduced scanning time and lower patient dosage determine which sets of data we may acquire. The sampling question then becomes, what information about the patient or object can we recover from a given set of data? We consider in this work two such sampling problems. In each problem we attempt to utilize all available information from the particular sampling scheme. This leads to irregular, or nonuniform, sampling sets in which case the classical sampling theorem does not apply. We must first characterize the available sampling sets and then apply the appropriate nonuniform sampling theorem to obtain the most faithful reconstruction possible.

The first problem arises from an attempt to utilize the reflection property of the 2D Radon transform in the fan beam scanning geometry. The integral over

the line L with direction $\theta \in S^2$ is numerically equal to the integral over L in the opposite direction, but the two measurements correspond to distinct points in the sampling domain. Thus, utilizing the reflection property may effectively double the number of sampling points. In parallel beam geometry this property is routinely used to reduce the amount of actual measurements by scanning only half the data and assuming the values on the remaining sampling points. Alternatively, it may also be used to produce an efficient, interlaced sampling scheme discussed by Rattey and Lindgren [33] and analyzed by Faridani and Ritman [10].

In the fan beam geometry, however, the union of the standard and reflected sampling sets do not form a uniform set, and the classical sampling theorem does not apply. How then do we utilize this information? Izen, Rohler and Sastry [13] introduce a new reconstruction method in which the sampling sets are viewed as a union of possibly many cosets, or shifted copies, of a single lattice. The new reconstruction algorithm is derived from a simplified version of a theorem for sampling on nonuniform but periodic sets. The simplification places further demands on the sampling conditions. Consequently, the application of this technique generally requires oversampling the number of views. Recent results by Mitchell [24] showed that the general periodic sampling theorem of Faridani [8] can be applied to accurately interpolate the data on a dense set suitable for the standard reconstruction algorithm with superior results.

In this work we address the problem in the more natural framework of nonperiodic sampling theory. We treat the sampling set as a union of two cosets of different lattices and apply the theorem of Behmard and Faridani [1] to accurately interpolate the values on a dense uniform set suitable for the standard reconstruction algorithm. We propose a novel decomposition of the data function in Fourier

space and show that the interpolation process is stable by proving an estimate for the aliasing error committed in the case of non-bandlimited data. This is a new result and stands alone as a significant advance in the area of nonperiodic sampling theory. We present numerical results from real and mathematically generated data which demonstrate the increase in resolution of the reconstruction.

The second problem we consider involves nonuniform sampling in 3D CT in the helical scanning geometry. A 3D image can be reconstructed slice-by-slice from a sequence of 2D cross sections or slices. Actually scanning slice-by-slice proves to be too time consuming for medical applications. Crawford and King [3] and Kalender et al. [16] introduced a scanning technique in which the patient or object is translated continuously through the scanning plane while the scanner rotates around the patient or object. The x-ray source then follows a helical path about a stationary object. The continuous translation decreases the scanning time, but projections from only one source position are measured at each position in the direction of the longitudinal axis of the helix. A complete set of projections is necessary to reconstruct the cross section. To obtain a complete set of projection data it is necessary to interpolate between corresponding data measured on either side of the reconstruction plane.

In an effort to reduce scanning times further and increase volume coverage, multi-row detector arrays are used to simultaneously acquire multiple slices per projection. Slices are not parallel, but the cone angle is ignored in practical situations. See Schaller et al. [36] for a description of scanning and reconstruction in multislice helical CT and see Hu [12] and Taguchi and Aradate [40] for analysis of reconstruction techniques. Scanning multiple slices per view complicates the interpolation process by producing interlaced sampling patterns. Understanding these complex

sampling patterns is necessary for effective use of this technique. Studies by Yen et al. [44, 45] and Wang and Vannier [42] concluded that the performance of the interpolation process varies irregularly with helical pitch. Attempts to identify preferred helical pitches were empirical in nature and focused primarily on performance only at the center of the scanning system. LaRivière and Pan [19, 20, 21] expanded the performance analysis to the entire field of view and shed light on the complex nature of the problem.

In this work we present a mathematical framework in which to analyze the theoretical and practical aspects of the problem of longitudinal interpolation in multislice helical CT. We present the interpolation problem as a collection of 1D nonuniform but periodic sampling problems. In this framework we analyze the interpolation problem over the entire field of view and shed considerable light on the role of helical pitch in the resolution of the reconstruction. Using an amplification factor in the estimate by Faridani [8] for the aliasing error committed in the case of non-bandlimited data, we identify choices of helical pitch which produce sets of stable interpolation across the scanner field of view. We also use the amplification factor to predict the performance of the interpolation scheme for a given choice of helical pitch, identifying where the interpolation may be unstable or unreliable. We identify the preferred helical pitch as that which permits uniformly stable interpolation across the scanner field of view. We present an accurate interpolation algorithm based on the periodic sampling theorem of Faridani [8] and present numerical results which demonstrate the performance of the interpolation process.

In the remainder of Chapter 1, we introduce the necessary definitions and notation. We follow the method of Faridani and present the standard definitions and theorems for Fourier analysis on locally compact abelian groups. This generalization

permits the application of the resulting theorems in a variety of situations by first identifying the underlying topology. We introduce the classical sampling theorem as well as theorems for sampling on unions of cosets of lattices. We introduce the mathematics of computed tomography in a notation consistent with that used in the sampling theory.

In Chapter 2 we solve the problem of utilizing the reflection property of the 2D Radon transform in the fan-beam geometry. We describe the sampling set as a union of cosets of two different lattices. We prove a corollary of the theorem by Behmard and Faridani [1] for sampling on unions of shifted lattices in the case of sampling on two cosets of different lattices with a compatibility condition and prove an estimate for the aliasing error committed in the case of non-bandlimited functions. We present a novel decomposition of the fan beam CT data function in Fourier space and an algorithm for interpolating the data on a dense uniform grid. We present numerical results from simulated and real data which show the improvement in image resolution.

In Chapter 3 we present the problem of longitudinal interpolation in multi-slice helical CT as a collection of 1D periodic sampling problems. We apply the theorem of Faridani [8] for periodic sampling and present an accurate interpolation algorithm. We identify a measure of suitability for the sampling scheme, i.e. choice of helical pitch, using an amplification factor in the estimate for the aliasing error given by Faridani. We identify candidates for the preferred helical pitch and present numerical results which demonstrate the performance of the interpolation process.

In Chapter 4 we make some concluding comments.

1.2 Standard Definitions and Theorems

Let $\mathbb{Z}$, $\mathbb{R}$, and $\mathbb{C}$ denote the integers, reals, and complex numbers respectively. For $x, y \in \mathbb{C}^n$ denote the scalar product by $x \cdot y = \sum_{i=1}^{n} x_i \overline{y_i}$. For $a, b \in \mathbb{R}$, mod (a, b) is the real number satisfying $0 \leq \text{mod}(a, b) < |b|$, and $a - \text{mod}(a, b) \in b\mathbb{Z}$. Denote by $[a]$ the fractional part of $a \in \mathbb{R}$, i.e. $[a] = \text{mod}(a, 1)$. We proceed in the manner of Faridani in [8] and of Behmard and Faridani in [1] and present Fourier analysis on locally compact abelian (LCA) groups. In this general framework we may apply the resulting theorems to a variety of problems by simply identifying the underlying topology.

Let G denote an LCA group written additively. Define the indicator function χ_s of $S \subset G$ by

$$\chi_S(x) = \begin{cases} 1, & \text{if} \quad x \in S, \\ 0, & \text{otherwise.} \end{cases} \tag{1.1}$$

The character group $\widehat{G}$ consists of the continuous homomorphisms of G into the circle group $\mathbb{T} = \mathbb{R}/\mathbb{Z}$. The value of the character $\xi \in \widehat{G}$ at the point $x \in G$ is written $\langle x, \xi \rangle$. $\widehat{G}$ has a natural addition and a natural topology relative to which it is an LCA group. If G is compact then $\widehat{G}$ is discrete. The Pontryagin duality theorem [35] states that

$$\widehat{\widehat{G}} = G. \tag{1.2}$$

Standard examples include $G = \mathbb{R}^n, \widehat{G} = \mathbb{R}^n$ and $G = \mathbb{T}^n, \widehat{G} = \mathbb{Z}^n$. In both examples, $\langle x, \xi \rangle = [x \cdot \xi]$.

On every LCA group there exists a nonnegative regular measure m_G, the Haar measure, which is translation invariant and not identically zero. The Haar measure is uniquely determined up to multiplication by a constant. If G is compact then we

normalize the measure m_G so that $m_G(G) = 1$. If G is discrete then m_G is a constant multiple of the counting measure. Let $L^p(G)$ denote the space of all Borel functions on G such that $\|f\|_p = (\int_G |f(x)|^p \, dm_G(x))^{1/p}$ is finite. The Fourier transform of a function $f \in L^1(G)$ is a continuous function $\hat{f}$ on $\widehat{G}$ with

$$\hat{f}(\xi) = \int_G f(x) e^{-2\pi i \langle x, \xi \rangle} \, dm_G(x). \tag{1.3}$$

We say a function f is *bandlimited with bandregion* K, or simply *bandlimited*, if $\hat{f}(\xi)$ vanishes for a.e. ξ outside a compact set $K \subset \widehat{G}$. We normalize the Haar measure on $\widehat{G}$ such that the following inversion formula holds.

Theorem 1. *If $f \in L^1(G)$ is continuous and $\hat{f} \in L^1(\widehat{G})$, then*

$$f(x) = \int_{\widehat{G}} \hat{f}(\xi) e^{2\pi i \langle x, \xi \rangle} \, dm_{\widehat{G}}(\xi) = \hat{\hat{f}}(-x). \tag{1.4}$$

The Fourier transform can be uniquely extended to a linear isomorphism of $L^2(G)$ onto $L^2(\widehat{G})$ by the Plancherel theorem.

Theorem 2. *The Fourier transform restricted to $L^1(G) \cap L^2(G)$ is an isometry (with respect to the L^2-norms) onto a dense linear subspace of $L^2(\widehat{G})$. Hence, it may me extended in a unique manner to an isometry of $L^2(G)$ onto $L^2(\widehat{G})$.*

Proof. For a proof, see [35]. □

The convolution $f * g$ of two functions $f, g \in L^2(G)$ is given by $(f * g)(x) = \int_G f(y)\overline{g(x-y)} \, dm_G(y)$. If $f * g \in L^2(G)$, then $(f * g)\hat{} \, (\xi) = \hat{f}(\xi)\hat{g}(\xi)$. The inversion formula

$$(f * g)(x) = \int_{\widehat{G}} \hat{f}(\xi)\hat{g}(\xi) e^{2\pi i \langle x, \xi \rangle} \, dm_{\widehat{G}}(\xi) \tag{1.5}$$

holds for all $f, g \in L^2(G)$.

Let H be a closed subgroup of an LCA group G. The annihilator of H is the set $H^\perp \subset \widehat{G}$ given by $H^\perp = \{\eta \in \widehat{G} : \langle y, \eta \rangle = 0 \text{ for all } y \in H\}$. $H^\perp$ is isomorphically homeomorphic to the character group of G/H, i.e.

$$H^\perp = (G/H)\widehat{\ }.$$

Furthermore,

$$(H^\perp)^\perp = H \quad \text{and} \quad \widehat{H} = \widehat{G}/H^\perp.$$

$H, H^\perp, G/H$, and $\widehat{G}/H^\perp$ are themselves LCA groups on which there exist Haar measures $m_H, m_{H^\perp}, m_{G/H}$, and $m_{\widehat{G}/H^\perp}$ respectively.

A closed discrete subgroup H of G such that $H^\perp$ is also discrete is called a *lattice*. A measurable subset R of $\widehat{G}$ is a *fundamental domain* of $H^\perp$ if for every $\xi \in \widehat{G}$ there exists a unique $\xi' \in R$ such that $\xi = \xi' + \eta$ with $\eta \in H^\perp$. Throughout this paper, when H is a lattice we adopt the following:

Convention 3. *We assume the measure m_G to be given and normalize the Haar measure on $\widehat{G}$ so that the Fourier inversion formula holds. For a lattice H we normalize the Haar measures on $H, H^\perp$, and $\widehat{G}/H^\perp$ according to the following:*

(i) m_H is the counting measure,

(ii) $m_{H^\perp}$ is $m_{\widehat{G}}(R)$ times the counting measure, and

(iii) $m_{\widehat{G}/H^\perp}(\widehat{G}/H^\perp) = 1$.

We always have $0 < m_{\widehat{G}}(R) < \infty$. The above normalizations imply that the inversion formula holds for the Fourier transform on H, and that for every $F \in L^1(\widehat{G})$

$$\int_{\widehat{G}} F \, dm_{\widehat{G}} = m_{\widehat{G}}(R) \int_{\widehat{G}/H^\perp} \sum_{\eta \in H^\perp} F(\xi + \eta) \, dm_{\widehat{G}/H^\perp}(\xi + H^\perp). \tag{1.6}$$

Multiplying $F(\xi)$ in (1.6) by $e^{2\pi i\langle y,\xi\rangle}$ for $y \in H$ gives

$$\begin{aligned} f(y) &= \int_{\widehat{G}} F(\xi) e^{2\pi i\langle y,\xi\rangle}\, dm_{\widehat{G}}(\xi) \\ &= m_{\widehat{G}}(R) \int_{\widehat{G}/H^\perp} e^{2\pi i\langle y,\xi\rangle} \sum_{\eta\in H^\perp} F(\xi+\eta)\, dm_{\widehat{G}/H^\perp}(\xi + H^\perp). \end{aligned} \tag{1.7}$$

Taking the Fourier transform on H leads to the Poisson summation formula (cf. [25]).

Theorem 4. *Let H be a lattice and R a fundamental domain of $H^\perp$. Assume $f \in L^1(G)$, that every function $y \mapsto f(x+y)$ belongs to $L^1(H)$, that $R_H f = \sum_{y\in H} f(x+y)$ is a continuous function on G/H, and that $(R_H f)^\wedge \in L^1(H^\perp)$. Then*

$$\sum_{y\in H} f(x+y) = m_{\widehat{G}}(R) \sum_{\eta\in H^\perp} \hat{f}(\eta) e^{2\pi i\langle x,\eta\rangle}. \tag{1.8}$$

If Theorem 4 can be applied to the function $x \mapsto f(x)e^{-2\pi i\langle x,\xi\rangle}$, $\xi \in \widehat{G}$, then we obtain

$$\sum_{y\in H} f(x+y) e^{-2\pi i\langle x+y,\xi\rangle} = m_{\widehat{G}}(R) \sum_{\eta\in H^\perp} \hat{f}(\xi+\eta) e^{2\pi i\langle x,\eta\rangle}. \tag{1.9}$$

Poisson's formula is a key element in error analysis for interpolation and numerical methods. If we let $\widehat{G} = \mathbb{T}^n$ then $H^\perp$ is a "multiple-integration lattice" as defined by Sloan and Kachoyan [38]. Recognizing that $f(0) = \int_{\widehat{G}} F(\xi)\, dm_{\widehat{G}}(\xi)$, we obtain the formula

$$m_{\widehat{G}}(R) \sum_{\eta\in H^\perp} F(\eta) - \int_{\widehat{G}} F(\xi)\, dm_{\widehat{G}}(\xi) = \sum_{y\in H\setminus\{0\}} f(y) \tag{1.10}$$

which describes the error committed by lattice rules for numerical integration.

Suppose $f \in L^1(G)$ is continuous, that the function $y \mapsto f(x_0+y)$ belongs to $L^1(H)$, and that $\hat{f} \in L^1(\widehat{G})$. Then by applying Theorem 4 to the function

$\xi \mapsto \hat{f}(\xi)e^{2\pi i\langle x_0,\xi\rangle}$ we obtain the formula

$$\sum_{y\in H} f(x_0+y)e^{-2\pi i\langle x_0+y,\xi\rangle} = m_{\widehat{G}}(R)\Big(\hat{f}(\xi) + \sum_{\eta\in H^\perp\setminus\{0\}} \hat{f}(\xi+\eta)e^{2\pi i\langle x_0,\eta\rangle}\Big). \tag{1.11}$$

This formula, we shall see, is the basis for analyzing the aliasing error committed when reconstructing f from values sampled on a coset of the lattice H. We see directly that if $\hat{f}$ vanishes outside a compact set $K \subset R$, then we recover $\hat{f}(\xi)$ for $\xi \in K$. An exact interpolation formula follows from the inverse Fourier transform.

Assume $G = \mathbb{T}^s \times \mathbb{R}^{n-s}$ and let $H \subset G$ be a lattice. The n-by-n nonsingular matrix W is said to *generate* the lattice H if $H = \{Wz : z \in \mathbb{Z}^n\}$, where Wz is computed modulo 1 in the first s components. The generator matrix W is not uniquely determined by the lattice H but $|\det(W)|$ is independent of the choice of generator. We say W is *feasible* for sampling on G if $e_j \in W\mathbb{Z}^n$ for $j = 1,\ldots,s$, where e_j are the canonical basis vectors of $\mathbb{R}^n$ (cf. [7]). The annihilator of H is generated by $H^\perp = W^{-T}\mathbb{Z}^n$ where $W^{-T} = (W^{-1})^T$.

1.3 Sampling Theorems

The classical sampling theorem permits reconstruction of a bandlimited function f with bandwidth Ω from its values on an equispaced set of points in $\mathbb{R}$. f is recovered by the formula

$$f(x) = \sum_{k\in\mathbb{Z}} f(k/2\Omega)\frac{\sin\pi(2\Omega x-k)}{\pi(2\Omega x-k)}. \tag{1.12}$$

It has been extended in many directions. The multidimensional sampling theorem of Petersen and Middleton [32] states that a function f on an N-dimensional Euclidean space "whose spectrum is restricted to a finite region in wave-number space" may

be reconstructed from its samples on a suitably dense lattice. Let $K = \text{supp}(\hat{f})$ be compact. The condition on the sampling lattice H is that translates of K by elements of $H^\perp$ are mutually disjoint. Petersen and Middleton go on to propose the existence of efficient sampling lattices which exactly reconstruct a bandlimited function from a minimal number of samples.

Kluvánek [17] introduced an important generalization by replacing $\mathbb{R}$ with an arbitrary LCA group G. The sampling set H is a closed subgroup of G. Assume the normalizations previously established for lattices. The following lemma appears as Lemma 1 in [1] and is proved in [17]. It provides the form of the reconstruction kernel.

Lemma 5. *Let H be a lattice and R and fundamental domain of $H^\perp$. The function ϕ_R defined by*

$$\phi_R(x) = \frac{1}{m_{\hat{G}}(R)} \int_R e^{2\pi i \langle x,\xi \rangle} \, dm_{\hat{G}}(\xi), \quad x \in G, \tag{1.13}$$

is continuous on G and satisfies $\phi_R(0) = 1$, $\phi_R(y) = 0, \quad 0 \neq y \in H$,
$\| \phi_R \|_2 = 1/\sqrt{m_{\hat{G}}(R)}$ and

$$\int_G \phi_R(x) \overline{\phi_R(x-y)} \, dm_G(x) = 0 \quad \textit{for} \quad 0 \neq y \in H.$$

Kluvánek's theorem as stated in Theorem 2 of [1] reads:

Theorem 6. *Let H be a lattice and R a fundamental domain of $H^\perp$. Suppose $f \in L^2(G)$ and $\hat{f}(\xi) = 0$ for almost all $\xi \notin R$. Then f is equal almost everywhere to a continuous function. If f itself is continuous then*

$$f(x) = \sum_{y \in H} f(y) \phi_R(x-y) \tag{1.14}$$

uniformly on G and in the sense of the convergence on $L^2(G)$. Furthermore

$$\|f\|_2^2 = \frac{1}{m_{\widehat{G}}(R)} \sum_{y \in H} |f(y)|^2. \tag{1.15}$$

The above handles uniform sampling on a single lattice. We now consider reconstruction from nonuniform sampling. The first approach, introduced by Kohlenberg [18] and developed further by Yen [43] and Faridani [6, 8], involves periodic sampling on unions of finitely many cosets of a single lattice H. We use the term periodic because the sampling points occur in a repeating pattern. The second approach introduced by Behmard and Faridani [1] from results by Walnut [41] involves nonperiodic sampling on unions of cosets of different lattices. In both cases we begin by considering the problem of reconstructing a function with Fourier transform supported on a set K that is larger than a fundamental domain R of $H^\perp$.

Let G be an LCA group, $H \subset G$ a lattice, and R a fundamental domain of $H^\perp$. Assume $f \in L^1(G)$ is continuous, every function $y \mapsto f(x+y)$ belongs to $L^1(H)$, and $\hat{f} \in L^1(\widehat{G})$ vanishes outside a compact set $K \subset \widehat{G}$. It follows that the Poisson summation formula holds with $F = \hat{f}$. Suppose H is too sparse to satisfy the sampling condition that translates of K by elements of $H^\perp$ are mutually disjoint. Then for some $\xi' \in K$ the set $M_{\xi'} = (H^\perp \setminus \{0\}) \cap (K - \xi')$ is nonempty. The value $\hat{f}(\xi')$ is then not recovered from samples of f on a single coset of H. The set $M_{\xi'} = \{\eta_j\}_{j=1}^{m-1}$ is finite since $H^\perp$ is discrete and $K - \xi'$ compact. Consider sampling f on a union of finitely many cosets of H and select $\{x_0, \ldots, x_{N-1}\} \subset G$ such that there exist constants $\beta_n \in \mathbb{C}$ for $n = 0, \ldots, N-1$ for which

$$\hat{f}(\xi') = \frac{1}{m_{\widehat{G}}(R)} \sum_{n=0}^{N-1} \beta_n \sum_{y \in H} f(x_n + y) e^{-2\pi i \langle x_n + y, \xi' \rangle} \tag{1.16}$$

where R is a fundamental domain of $H^\perp$. It follows that the weights β_n, $n =$

$0, \ldots, N-1$ must satisfy

$$\begin{aligned} \sum_{n=0}^{N-1} \beta_n &= 1, \\ \sum_{n=0}^{N-1} \beta_n e^{2\pi i \langle x_n, \eta_j \rangle} &= 0, \qquad j = 1, \ldots, m-1, \end{aligned} \tag{1.17}$$

with $\{\eta_j\}_{j=1}^{m-1} = M_{\xi'}$.

We now consider the problem of recovering $\hat{f}$ on all of $K \subset \widehat{G}$. For $\xi \in K$ the set $M_\xi = (H^\perp \setminus \{0\}) \cap (K - \xi)$ is contained in $H^\perp \cap (K - K)$, which is finite since $H^\perp$ is discrete and $(K - K)$ compact. Hence, as ξ runs through K, M_ξ will assume only finitely many values $M^{(1)}, \ldots, M^{(L)}$. The relation $\xi \equiv \xi' \leftrightarrow M_\xi = M_{\xi'}$ is an equivalence relation induced by the subgroup H. The equivalence classes are $K_l = \{\xi \in K : M_\xi = M^{(l)}\}$, $l = 1, \ldots, L$. The sets K_l are mutually disjoint and we have $K = \cup_{l=1}^{L} K_l$. The sets K_l consist of the points ξ for which $\xi + \eta \in K$ if $\eta \in M^{(l)} \cup \{0\}$ and $\xi + \eta \notin K$ if $\eta \in H^\perp \setminus (M^{(l)} \cup \{0\})$.

With H a lattice and normalizing the Haar measures on H, $H^\perp$, and $\widehat{G}/H^\perp$ according to Convention 3 we obtain the following version of Theorem 3.5 in [8].

Theorem 7. *Assume $f \in L^1(G)$ is continuous, every function $y \mapsto f(x+y)$ belongs to $L^1(H)$, and that $\hat{f}$ vanishes outside a compact set $K \subset \widehat{G}$. Let $M^{(l)} = \{\eta_1^{(l)}, \ldots, \eta_{m_l-1}^{(l)}\}, l = 1, \ldots, L$, be the values assumed by $(H^\perp \setminus \{0\}) \cap (K - \xi)$ as ξ runs through K. Let χ_{K_l} be the indicator function of $K_l = \{\xi \in K : M_\xi = M^{(l)}\}$. Assume $(x_0 + H), \ldots, (x_{N-1} + H) \in G/H$ are such that for $l = 1, \ldots, L$ the systems of equations*

$$\begin{aligned} \sum_{n=0}^{N-1} \beta_n^{(l)} &= 1, \\ \sum_{n=0}^{N-1} \beta_n^{(l)} e^{2\pi i \langle x_n, \eta_j^{(l)} \rangle} &= 0, \qquad j = 1, \ldots, m_l - 1, \end{aligned} \tag{1.18}$$

admit solutions $\beta_n^{(l)}$, $n = 0, \ldots, N-1$. *Define* $(Sf)\widehat{\ }$ *by*

$$(Sf)\widehat{\ }(\xi) = \frac{1}{m_{\widehat{G}}(R)} \sum_{n=0}^{N-1} \sum_{l=1}^{L} \beta_n^{(l)} \chi_{K_l}(\xi) \sum_{y \in H} f(x_n + y) e^{-2\pi i \langle x_n + y, \xi \rangle} \tag{1.19}$$

and $Sf(x) = \int_{\widehat{G}} (Sf)\widehat{\ }(\xi) e^{2\pi i \langle x, \xi \rangle} \, dm_{\widehat{G}}(\xi)$. *Then*

$$\hat{f}(\xi) = (Sf)\widehat{\ }(\xi) \quad \textit{for} \quad \xi \in \widehat{G} \tag{1.20}$$

and

$$f(x) = Sf(x) = \sum_{n=0}^{N-1} \sum_{y \in H} f(x_n + y) k_n(x - x_n - y) \tag{1.21}$$

with

$$k_n(z) = \frac{1}{m_{\widehat{G}}(R)} \sum_{l=1}^{L} \beta_n^{(l)} \int_{K_l} e^{2\pi i \langle z, \xi \rangle} \, dm_{\widehat{G}}(\xi). \tag{1.22}$$

Proof. Follow the proof in [8] for H a lattice and with the normalizations in Convention 3. □

Faridani also gives an estimate for the error committed when (1.21) is used to approximate f in the case when $\hat{f}$ does not vanish outside the set K. The following appears as Corollary 3.7 in [8].

Theorem 8. *Assume that the hypotheses of Theorem 7 hold except the condition that* $\hat{f}$ *vanishes outside the set* K. *Assume instead that* $\hat{f} \in L^1(\widehat{G})$ *and that the Poisson summation formula (1.8) holds for all* $x \in \{x_0, \ldots, x_{N-1}\}$ *and almost all* $\xi \in K$. *Then*

$$|(Sf)(x) - f(x)| \leq (1 + \gamma) \int_{\widehat{G} \setminus K} |\hat{f}(\xi)| \, dm_{\widehat{G}}(\xi) \tag{1.23}$$

for all $x \in G$, *where*

$$\gamma = \overline{m} \left(\max_{l=1,\ldots,L} \sum_{n=0}^{N-1} \left| \beta_n^{(l)} \right| \right), \qquad \overline{m} = \max_{l=1,\ldots,L} (m_l). \tag{1.24}$$

Proof. Follow the proof in [8]. □

The error estimate contains an amplification factor γ, the value of which depends on the solutions of the systems (1.18). In Chapter 3 we will use this factor to determine whether a periodic sampling scheme, i.e. choice of $\{x_n\}_{n=0}^{N-1}$, is suitable for a stable interpolation purposes. A low value of γ would indicate a good choice of sampling scheme.

Let G be an LCA group, $H \subset G$ a lattice and R a fundamental domain of $H^\perp$. Consider the situation where $\hat{f}$ vanishes a.e. outside a set K which is contained in a union of finitely many translates of R by elements of $H^\perp$. Behmard and Faridani present the following corollary to Kluvánek's theorem. It appears as Corollary 1 in [1].

Corollary 9. *Let H be a lattice and R a fundamental domain of $H^\perp$. Let $f \in L^2(G)$ be continuous and $\hat{f}(\xi) = 0$ a.e. outside a measurable subset K of $\widehat{G}$. Assume that there is $P < \infty$ such that $K \subseteq \cup_{j=1}^{P}(\eta_j + R)$ with $\eta_1, \ldots, \eta_P$ distinct elements of $H^\perp$. Let $M = x_0 + H$ be a coset of H then the function $S_M f$ defined by*

$$(S_M f)(x) = \sum_{y \in H} f(x_0 + y)\phi_R(x - x_0 - y) \tag{1.25}$$

is continuous and square integrable on G, and satisfies $(S_M f)(z) = f(z)$ for all $z \in M$.

Suppose the set K is contained in the union of R and one of its translates by an element of $H^\perp$. Behmard and Faridani [1] show that overcoming aliasing due to undersampling a function f on H amounts to reconstructing a function h with $\hat{h}(\xi) = 0$ for a.e. $\xi \in K' \subset R$. The following appears as Lemma 2 in [1].

Lemma 10. *Let H be a lattice and R a fundamental domain of $H^\perp$. Let $K = R \cup (\eta' + K')$ with $K' \subset R$ measurable and $0 \neq \eta' \in H^\perp$. Assume that $f \in L^2(G)$ is continuous, that f vanishes on the coset $x_0 + H$, and that $\hat{f}$ vanishes a.e. outside K. Then*

$$f(x) = h(x)\left(1 - e^{2\pi i \langle x - x_0, \eta' \rangle}\right) \tag{1.26}$$

with $h \in L^2(G)$ continuous and $\hat{h}$ vanishing a.e. outside K'.

The following nonperiodic sampling theorem appears as Theorem 3 in [1].

Theorem 11. *Let H be a lattice and R a fundamental domain of $H^\perp$. Let $K = R \cup (\eta' + K')$ with $K' \subset R$ measurable and $0 \neq \eta' \in H^\perp$. Assume that $f \in L^2(G)$ is continuous and that $\hat{f}$ vanishes almost everywhere outside K. Let $M' \subset G$ be such that continuous functions $h \in L^2(G)$ whose Fourier transforms vanish a.e. outside K' can be reconstructed from their samples $h(z'), z' \in M'$. Let x_0 be such that*

$$\langle z' - x_0, \eta' \rangle \neq 0 \quad \text{for all} \quad z' \in M'. \tag{1.27}$$

Then f can be reconstructed from its samples $f(z), z \in M \cup M'$, where $M = x_0 + H$.

A reconstruction algorithm presented in [1] follows from the proof of the theorem.

Algorithm 12. *1. Compute $S_M f(x)$, $x \in G$ from the samples $f(z)$, $z \in M$ according to (1.25).*

2. Compute the samples $h(z')$, $z' \in M'$ according to

$$h(z') = \frac{f(z') - S_M f(z')}{1 - e^{2\pi i \langle z' - x_0, \eta' \rangle}}. \tag{1.28}$$

3. Reconstruct $h(x)$, $x \in G$, from these samples, which is possible by hypothesis.

4. Compute $f(x)$, $x \in G$ according to

$$f(x) = S_M f(x) + h(x)\big(1 - e^{2\pi i\langle x - x_0, \eta'\rangle}\big). \tag{1.29}$$

Applying Theorem 11 to the problem of reconstructing h leads to a recursive algorithm presented in [1] which permits reconstruction of a function f from samples measured on a union of cosets of a finite number of lattices. The algorithm is more complex than is needed for the present application, so it is not discussed here. Consider the problem of reconstruction of a function f from samples on just two lattices H_1 and H_2. We apply Theorem 11 with $M = x_2 + H_2$ and $M' = x_1 + H_1$. The following appears as Corollary 2 in [1].

Corollary 13. *Let H_1, H_2 be lattices, and $R_1 \subset R_2$ fundamental domains of $H_1^\perp$ and $H_2^\perp$, respectively. Let $f \in L^2(G)$ be continuous and such that $\hat{f}$ vanishes a.e. outside the set $K = R_2 \cup (\eta' + R_1)$, where $0 \neq \eta' \in H_2^\perp$. Let x_1, x_2 be such that*

$$\langle x_1 - x_2 + y, \eta'\rangle \neq 0 \quad \textit{for all} \quad y \in H_1. \tag{1.30}$$

Then,

$$\begin{aligned} f(x) = (S_M f)(x) + \Big(1 - e^{2\pi i\langle x - x_2, \eta'\rangle}\Big) \\ \times \sum_{y \in H_1} \frac{f(x_1 + y) - S_M f(x_1 + y)}{1 - e^{2\pi i\langle x_1 - x_2 + y, \eta'\rangle}} \phi_{R_1}(x - x_1 - y) \end{aligned} \tag{1.31}$$

with $M = x_2 + H_2$,

$$S_M f(x) = \sum_{z \in H_2} f(x_2 + z)\phi_{R_2}(x - x_2 - z), \tag{1.32}$$

and ϕ_{R_j}, $j = 1, 2$ as defined in (1.13).

1.4 Computed Tomography

The mathematical problem in computed tomography (CT) is to accurately reconstruct a function from a finite number of its line integrals. We parameterize the line $l(\theta, x)$ in $\mathbb{R}^n$ by its direction $\theta \in S^{n-1}$ and the point x where l intersects the hyperplane $\Theta^\perp$ through the origin and orthogonal to θ. The x-ray transform of $f \in C_0^\infty(\mathbb{R}^n)$ is defined by

$$Pf(\theta, x) = P_\theta f(x) = \int_{\mathbb{R}} f(x + t\theta)\, dt, \quad x \in \Theta^\perp. \tag{1.33}$$

The set $H = \{t\theta : t \in \mathbb{R}\}$ is a closed subgroup of $G = \mathbb{R}^n$. We may identify both the coset group G/H and the annihilator $H^\perp$ with the hyperplane $\Theta^\perp$. We let m_G be the Lebesgue measure on $\mathbb{R}^n$ and normalize the Haar measures on H and G/H so that m_H and $m_{G/H}$ are the Lebesgue measures on $\mathbb{R}^1$ and $\mathbb{R}^{n-1}$ respectively. Then the formula

$$\int_G f(x)\, dm_G(x) = \int_{G/H} \int_H f(x + y)\, dm_H(y) dm_{G/H}(x + H) \tag{1.34}$$

holds for all $f \in L^1(G)$. Multiplying $f(x)$ by $e^{-2\pi i \langle x, \eta \rangle}$ with $\eta \in H^\perp$ and recognizing that $P_\theta f(x) = \int_H f(x + y)\, dm_H(y)$, we obtain the formula

$$\hat{f}(\eta) = (P_\theta f)\hat{}(\eta), \quad \eta \in H^\perp. \tag{1.35}$$

Note that the Fourier transform on the left is with respect to G while the Fourier transform on the right is with respect to G/H. This is the well known projection-slice theorem (cf. [25]) and serves as an important link between the x-ray and Fourier transforms. This particular presentation is discussed in [8].

In two-dimensional CT, $n = 2$, we parameterize $\theta \in S^1$ by the angle $0 \leq \phi < 2\pi$ and $x \in \Theta^\perp$ by the real number s such that $\theta = (\cos\phi, \sin\phi)^T$ and $x = s\theta^\perp =$

$s(-\sin\phi, \cos\phi)^T$. The inverse Fourier transform of f on $\mathbb{R}^2$ in polar coordinates and the projection slice theorem (1.35) lead to an inversion formula

$$f(x) = \int_0^{2\pi} \int_0^{\infty} (Pf_\theta)\hat{}(\sigma) e^{2\pi i \sigma (x \cdot \theta^\perp)} \sigma \, d\sigma d\phi. \tag{1.36}$$

Exact inversion is considered numerically unstable since the factor σ amplifies high frequency components of the data function, including noise or round-off errors. Instead, we reconstruct an approximate solution $(W_b * f)(x)$ where W_b is a low-pass filter with cut-off frequency b. That is, W_b approximates the Dirac δ-distribution and $\widehat{W_b}$ is radially symmetric with $\widehat{W_b}(\xi) = 0$ for $|\xi| > b$. The approximate inversion formula is

$$(W_b * f)(x) = \int_0^{2\pi} \int_{\mathbb{R}} w_b(x \cdot \theta^\perp - s) Pf(\phi, s) \, ds d\phi, \tag{1.37}$$

where $\widehat{W_b}(\xi) = 2|\xi|^{-1} \hat{w}_b(|\xi|)$ (cf. [25]). We use a low-pass filter attributed to Shepp and Logan [37].

In practice there is a trade-off between resolution and stability. If the cut-off frequency, b, is chosen to be relatively low, then the reconstruction is stable but lacking in detail. If b is chosen to be relatively high, the reconstruction will contain sharper details but may be obscured by large, highly oscillating errors. It is important to choose a cut-off frequency which produces the optimal reconstruction for a given set of data.

In modern CT scanners, x-rays emanate from a point source which is then moved about, capturing different "views" of the object. It is convenient to consider a geometry in which we measure integrals over rays diverging from a single point. The divergent beam transform of $f \in C_0^\infty(\mathbb{R}^n)$ is defined by

$$Df(a, \theta) = \int_0^{\infty} f(a + t\theta) \, dt, \quad a \in \mathbb{R}^n, \ \theta \in S^{n-1}. \tag{1.38}$$

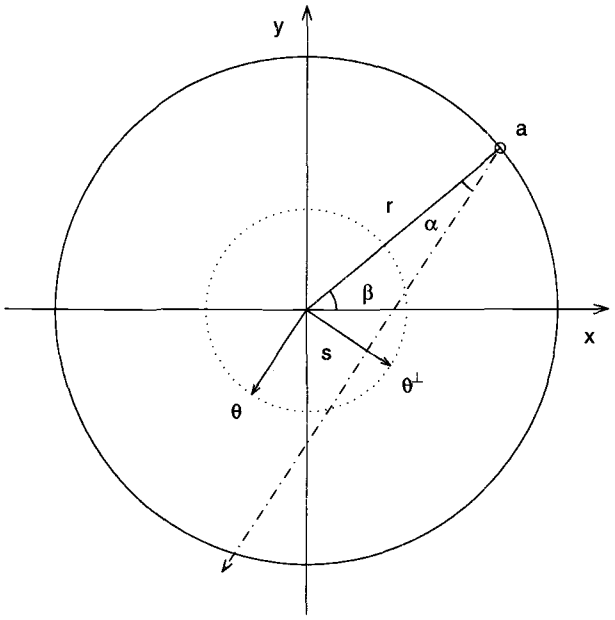

Figure 1.1: Fan beam scanning geometry.

We then consider source points lying on a curve in $\mathbb{R}^n$.

Assume that f vanishes outside the unit disc in $\mathbb{R}^2$ and consider source points on a circle of radius $r > 1$ about the origin. Parameterize the source point a by the angle $0 \leq \beta < 2\pi$ and each ray emanating from a by the angle $-\pi/2 \leq \alpha < \pi/2$ measured counter clockwise from the line connecting the source point and the origin. See Figure 1.1. This is referred to as the "fan beam" geometry. We abuse the notation and let $Df(\beta, \alpha) = Df(a, \theta)$. The following identity holds:

$$Df(\beta, \alpha) = Pf(\beta + \alpha + \pi, r \sin \alpha), \ 0 \leq \beta < 2\pi, \ -\pi/2 \leq \alpha < \pi/2. \tag{1.39}$$

We apply a change of variables to (1.37) and make an approximation for $|x| \ll r$ ([25] pp. 112-113) which reduces the dependency of w_b on the reconstruction point

x to obtain the approximate inversion formula

$$(W_b * f)(x) \approx r \int_0^{2\pi} |a-x|^{-2} \int_{-\pi/2}^{\pi/2} w_{rb}(\sin(\gamma-\alpha)) Df(\beta,\alpha) \cos\alpha \, d\alpha d\beta, \quad (1.40)$$

where γ is the angle made by the line connecting the source point and the reconstruction point x as measured from the central line connecting a and the origin. To remove the dependency of w_b on the reconstruction point x entirely, we compute $w_{rb}(t)$ at select t and interpolate the values for each reconstruction angle γ.

In practice, we measure only a finite number of integrals for finitely many views. It remains to determine what information about Df we can expect to recover from a finite sample set, and what sampling scheme to use in order to reconstruct a desired image. The standard sampling scheme in fan beam CT measures the samples $Df(\beta_j, \alpha_l)$, with

$$\beta_j = \frac{2\pi j}{M}, \; j = 0, \ldots, M-1, \text{ and } \alpha_l = \frac{\pi(l+\delta)}{N}, \; l = -q, \ldots, q-1, \quad (1.41)$$

for integers M and N with $N(\arcsin(1/r)/\pi) \leq q \leq N/2$, and detector offset $\delta \in \{0, \pm 1/4\}$. Other, non rectangular, sampling schemes have been proposed that are more efficient in that they recover the same information about Df from fewer samples (see e.g. [26] and [11]), but they are difficult to implement in practice. In order to determine an appropriate sampling scheme we must first consider the Fourier transform of Df.

We view Df as a function on the two dimensional torus group $G = \mathbb{T}^2$. Take as a model for $\mathbb{T}$ the set $[0,1)$ with addition modulo 1. Define for $(u,v) \in \mathbb{T}^2$ the function

$$g(u,v) = Df(2\pi u, \pi(v-1/2)). \quad (1.42)$$

The Haar measure on G is the Lebesgue measure on $\mathbb{R}^2$ restricted to $[0,1)^2$. Then

the Fourier transform of g is the continuous function $\hat{g}$ on $\widehat{G} = \mathbb{Z}^2$ given by

$$\begin{aligned}\hat{g}(k,m) &= \int_0^1 \int_0^1 g(u,v) e^{-2\pi i(uk+vm)}\, du dv \\ &= \int_0^1 \int_0^1 Df(2\pi u, \pi(v-1/2)) e^{-i(2\pi vk + \pi v(2m))}\, du dv \\ &= \frac{(-1)^m}{2\pi^2} \int_0^{2\pi} \int_{-\pi/2}^{\pi/2} Df(\beta,\alpha) e^{-i(\beta k + \alpha(2m))}\, d\alpha d\beta.\end{aligned} \tag{1.43}$$

Estimates by Palamodov [30] imply that $|\hat{g}|$ decays exponentially in the region where $|k|$ is larger than $|k-2m|/r$. (See Theorem 2 in [30].) Let $0 < \rho < 1$ be such that $f(x) = 0$ for $|x| > \rho$. Then Natterer [26, 28] states that if $|\hat{f}(\xi)|$ is small for $|\xi| > \Omega$ then $|\hat{g}|$ is small outside the set $K = \{(k,m) \in \mathbb{Z}^2 : |k-2m| < r\Omega,\ |k|r < |k-2m|\rho\}$. For computational purposes we consider a slightly larger set; one which includes a small region about the origin and wider boundaries to account for dense features of f located near $|x| = \rho$. We define the set K_τ for $0 < \tau < 1$ by

$$K_\tau(r,\rho,\Omega) = \{(k,m) : |k-2m| < r\Omega,\ |k|r < \tau^{-1}\max(|k-2m|\rho, (1-\tau)\rho r\Omega)\}. \tag{1.44}$$

(See [11].) For convenience we may write K_τ for $K_\tau(r,\rho,\Omega)$ when the scanning and object parameters are understood. In practice we choose τ close to one. See Figure 1.2.

The standard sampling scheme on $\mathbb{T}^2$ measures values of g at the points $\{(u_j, v_l)\}_{j,l}$ with

$$\begin{aligned} u_j &= \frac{j}{M},\ j = 0,\ldots,M-1, \\ v_l &= \frac{(l+\delta)}{N},\ l = 0,\ldots,N-1. \end{aligned} \tag{1.45}$$

Then the sampling set is a coset of the standard sampling lattice H_S is generated

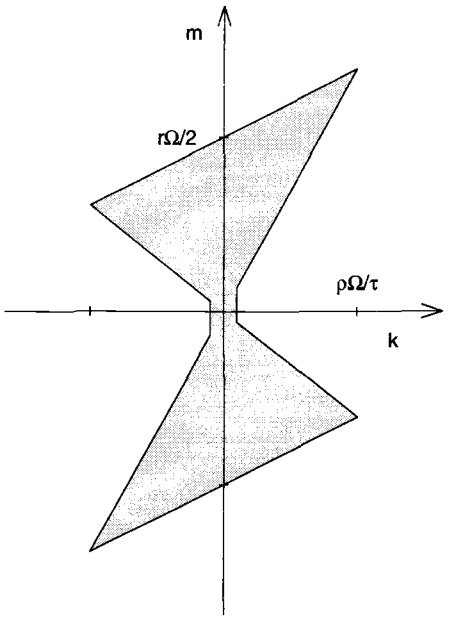

Figure 1.2: The set $K_\tau(r, \rho, \Omega)$ with $r = 2.868$, $\rho = 1$, and $\tau = 0.9$.

by the matrix

$$W_S = \begin{pmatrix} 1/M & 0 \\ 0 & 1/N \end{pmatrix}. \tag{1.46}$$

and shifted by $x_S = (0, \delta/N)^T$. The annihilator $H_S^\perp$ of the standard sampling lattice is generated by the matrix

$$W_S^{-T} = (W_S^{-1})^T = \begin{pmatrix} M & 0 \\ 0 & N \end{pmatrix}. \tag{1.47}$$

We wish to choose integers M and N such that translates of the set K_τ by elements of $H_S^\perp$ do not intersect. Then K_τ is contained in a fundamental domain R of $H_S^\perp$ and the function g is essentially recovered by Theorem 6. The minimum sampling

conditions are

$$M = r\Omega\left(\frac{2\vartheta}{1+\vartheta}\right) \quad \text{and} \quad N = r\Omega, \tag{1.48}$$

where $\vartheta = \tau^{-1}(\rho/r)$ (cf. [26]). Due to the shape of the set K_τ, care must be taken when selecting M and N near the minimal values. If $M = r\Omega(2\vartheta)/(1+\vartheta)$, and N is chosen slightly larger than the minimal value of $r\Omega$, then translates of K_τ by elements of $H_S^\perp$ are no longer disjoint, and we do not recover the function g from samples on H_S. This is similar to the counter-intuitive situation discussed in [7] where increasing the density of the interlaced sampling lattice actually leads to increased aliasing error. More comprehensive sampling conditions are given by the following:

$$\begin{aligned} &\text{If} \quad r\Omega\left(\frac{2\vartheta}{1+\vartheta}\right) \leq M \leq 2\vartheta r\Omega, \\ &\text{then choose either} \\ &r\Omega \leq N \leq M\left(\frac{1+\vartheta}{2\vartheta}\right) \quad \text{or} \quad N \geq (2r\Omega + M/2). \end{aligned} \tag{1.49}$$

If $M > 2\vartheta r\Omega$ then we may simply choose $N > r\Omega$ to satisfy the sampling criterion (cf. [11]).

With the sampling conditions satisfied, we can now discretize the integrals in the reconstruction formula (1.40) and reconstruct a filtered version of the function f from finitely samples of g. This is the commonly used filtered backprojection algorithm. If we measure g with the standard sampling scheme, then we simply use the same discretization in the reconstruction formula and reconstruct f directly from the measurements. Studies suggest that, with other sampling schemes, reconstructing directly from the measured data may not give optimal results. A better method is to first interpolate the values of g on a more dense lattice and then reconstruct f from the interpolated data. Accurate interpolation of bandlimited data

is possible since the sampling conditions are satisfied. For a discussion of sampling errors and reconstruction properties in fan beam tomography see [11] and [14]. The following version of the filtered backprojection algorithm is adapted from Natterer and Wübbeling [28]. It uses the Shepp-Logan filter with a modification involving the *sinc* function and suggested by Kak and Slaney [15].

Algorithm 14. *Let* $g_{j,l} = Df(2\pi j/M, \pi((l+\delta)/N - 1/2))$. *For* $j = 0, \ldots, M-1$ *perform the following:*

1. *Compute for* $k = 0, \ldots, N-1$ *the discrete convolution*

$$h_{j,k} = \frac{\pi}{N} \sum_{l=0}^{N-1} \frac{w_{rb}(\pi(v_k - v_l))}{(sinc(\pi(v_k - v_l))/\pi)^2} \, g_{j,l} \cos(\pi(v_l - 1/2)), \tag{1.50}$$

   where $sinc(\theta) = \sin(\theta)/\theta$.

2. *For each* x *in the reconstruction compute the interpolated backprojection*

$$f_j = (1-\omega)h_{j,k} + (\omega)h_{j,k+1} \tag{1.51}$$

   where $k = k(j,x)$ *and* $\omega = \omega(j,x)$ *are determined by*

$$\begin{aligned} &\gamma = \pm \arccos \frac{(a_j - x) \cdot a_j}{r|a_j - x|}, \quad \text{“+” for } x \cdot a_j^{\perp} \le 0, \ \text{“−” for } x \cdot a_j^{\perp} > 0, \\ &t = N\left(\frac{\gamma}{\pi} + \frac{1}{2}\right) - \delta, \quad \omega = [t], \quad k = t - \omega. \end{aligned} \tag{1.52}$$

The approximation $f_{FB}(x)$ *of* $f(x)$ *is given by*

$$f_{FB} = \frac{2\pi r}{M} \sum_{j=0}^{M-1} f_j. \tag{1.53}$$

We use the filtered back projection algorithm in both Chapters 2 and 3 to reconstruct filtered versions of f from measured and interpolated data.

2 EXPLOITING SYMMETRY IN FAN BEAM CT

The x-ray transform possesses a symmetry in the sample domain. The integral of $f \in C_0^\infty(\mathbb{R}^n)$ over the line parameterized by direction $\theta \in S^{n-1}$ and passing through the point $a \in \mathbb{R}^n$ is equal to the integral of f over the line through a with direction $-\theta$. In the 2-dimensional fan beam geometry this symmetry property reads:

$$Df(\beta, \alpha) = Df(\beta + 2\alpha + \pi, -\alpha). \tag{2.1}$$

This means that each measurement of Df may be used twice, giving its value at a point in the regular sampling lattice and at a corresponding "reflected" point in the domain. The reflected points form a coset of a second sampling lattice. We present a technique which utilizes the reflected sampling set to improve the quality of the reconstruction from data acquired by the standard sampling scheme in fan beam CT.

2.1 Sampling and Reconstruction

The standard scheme for sampling a function g on $\mathbb{T}^2$ measures the values $g(u_j, v_l)$, with $u_j = [j/N_1]$ and $v_l = [(l + \delta)/N_2]$ for $j, l \in \mathbb{Z}$, with N_1, N_2 integers and $\delta \in \{0, \pm 1/4\}$. The symmetry property (2.1) of Df and identity (1.42) imply $g(u, v) = g(u + v, 1 - v)$. Then the reflected set associated with the standard sampling scheme is given by $\{(u'_{j,l}, v'_l)\}$, where $u'_j = [j/N_1 + l/N_2 + \delta/N_2]$, and $v'_l = [(N_2 - l - \delta)/N_2]$ for $j, l \in \mathbb{Z}$. By a change of index, $l' = N_2 - l$, we have that

the reflected sampling set is a coset of a lattice H_R generated by the matrix

$$W_R = \begin{pmatrix} 1/N_1 & -1/N_2 \\ 0 & 1/N_2 \end{pmatrix} \tag{2.2}$$

and shifted by $x_R = (\delta/N, -\delta/N)^T$. The annihilator $H_R^\perp$ of the reflected lattice H_R is generated by the matrix

$$W_R^{-T} = \begin{pmatrix} N_1 & 0 \\ a & N_2 \end{pmatrix}, \tag{2.3}$$

where $a =$ mod (N_1, N_2). Since $\det(W_S) = \det(W_R)$, the standard and reflected sampling lattices have the same density in $\mathbb{T}^2$. Employing a quarter-detector offset, $\delta = \pm 1/4$, insures that the standard sampling set $(x_S + H_S)$ and the reflected sampling set $(x_R + H_R)$ are disjoint and prohibits redundancy in the data. The union of the standard and reflected sampling sets is a set with twice the density of the standard sampling scheme alone. The combined sampling set, however, is generally nonuniform. That is to say, it is not a coset of a single lattice, H. The classical sampling theorem then does not apply, and we can not perform the standard reconstruction Algorithm 14 with this more dense set of data.

Izen, Rohler, and Sastry [13] discovered that one may decompose the combined sampling set into a union of $2N'$ cosets of a single rectangular lattice L_P, where N' is the denominator of the ratio N_1/N_2 when in reduced form. Izen et al. use this decomposition to propose a new discretization of the integrals in the reconstruction formula (1.40). Alternatively, Theorem 7 may be applied to interpolate the values of g on a sufficiently dense uniform set, then the standard FBP algorithm may be used. Recent results by Mitchell [24] suggest that this approach gives optimal results. The decomposition of the sampling set depends on the values of the scanning

parameters N_1 and N_2. The simplest case occurs when $N_1 = kN_2$ for $k \in \mathbb{Z}$. Then $N' = 1$ and the original and reflected sampling sets are both cosets of the lattice H_S. In many cases, however, N' is large. Viewed in this manner, the sampling set is a union of many cosets of a sparse lattice L_P. The fact that L_P is sparse means that translates of K_τ by elements of $L_P^\perp$ overlap in many regions. Also, since K_τ is non-convex, the overlapping regions partition the set K_τ into a union of subsets K_l, $l = 1, \ldots, L$ with L large and involving many elements of $L_P^\perp$ that may be nonzero in either component. The reconstruction method proposed by Izen et al. requires that the a 'shift convexity' condition be met by the set K_τ with respect to the sampling lattice L_P (see [13], Section 3.2.3). It requires that all overlapping regions of K_τ correspond to shifts by elements of $L_P^\perp$ that are nonzero only in the second coordinate. Satisfying this condition amounts to oversampling in the number of views per rotation. A naive application of Theorem 7 to overcome the undersampling on a sparse lattice L_P and interpolate the values of G on a dense uniform lattice leads to a complex interpolation process involving the solution for $l = 1, \ldots, L$ large, the systems (1.18) with m_l large. It is more natural to treat the sampling set as a union of cosets of just two different lattices, H_S and H_R, and apply the nonperiodic sampling Theorem 11. This is the approach taken here.

We begin by developing the mathematical tools necessary to recover the scanning data function on a suitably dense set and to analyze the results. We present a version of Corollary 13 of Chapter 1 in the case that the bandregion $K = R_2 \cup (\eta' + K')$, where $K' \subseteq R_1 \cap R_2$ and $\eta' \in H_1^\perp \cap H_2^\perp$. Then $\langle x_1 - x_2 + y, \eta' \rangle = \langle x_1 - x_2, \eta' \rangle$ for all $y \in H_1^\perp$ and a simpler reconstruction formula results.

Corollary 15. *Let H_1, H_2 be lattices and R_1, R_2 fundamental domains of $H_1^\perp, H_2^\perp$ respectively. Let $f \in L^2(G)$ be continuous and such that $\hat{f}$ vanishes a.e. outside the*

set $K = R_2 \cup (\eta' + K')$ *with* $K' \subseteq R_1 \cap R_2$ *measurable and* $0 \neq \eta' \in H_1^\perp \cap H_2^\perp$. *Let* x_1, x_2 *be such that* $\langle x_1 - x_2, \eta' \rangle \neq 0$. *Then*

$$f(x) = S_M f(x) + \beta \left(1 - e^{2\pi i \langle x - x_2, \eta' \rangle}\right) \times \sum_{y \in H_1} (f - S_M f)(x_1 + y) \phi_{R_1}(x - x_1 - y), \tag{2.4}$$

where $\beta = (1 - e^{2\pi i \langle x_1 - x_2, \eta' \rangle})^{-1}$ *and*

$$S_M f(x) = \sum_{z \in H_2} f(x_2 + z) \phi_{R_2}(x - x_2 - z), \tag{2.5}$$

with $M = x_2 + H_2$ *and* ϕ_{R_j}, $j = 1, 2$ *defined in (1.13).*

Proof. We follow the proof of Corollary 2 in [1] and apply Theorem 11 with $M = x_2 + H_2$ and $M' = x_1 + H_1$. It follows from (1.13) and Corollary 9 that the function $(f - S_M f)$ is continuous, square integrable on G, vanishes on the coset M, and that $(f - S_M f)\hat{}$ vanishes a.e. outside the set K. Then by Lemma 10,

$$(f - S_M f)(x) = h(x) \left(1 - e^{2\pi i \langle x - x_2, \eta' \rangle}\right) \tag{2.6}$$

where $h \in L^2(G)$ is continuous and such that $\hat{h}$ vanishes a.e. outside K'. For all $y \in H_1$, $\langle x_1 - x_2 + y, \eta' \rangle = \langle x_1 - x_2, \eta' \rangle \neq 0$ by hypothesis. Letting $\beta = (1 - e^{2\pi i \langle x_1 - x_2, \eta' \rangle})^{-1}$, we compute the samples

$$h(x_1 + y) = \beta (f - S_M f)(x_1 + y). \tag{2.7}$$

Since $\hat{h}$ vanishes a.e. outside $K' \subseteq R_1$, it follows that $\hat{h}$ vanishes a.e. outside R_1. Then by Theorem 6,

$$h(x) = \sum_{y \in H_1} h(x_1 + y) \phi_{R_1}(x - x_1 - y). \tag{2.8}$$

Substituting (2.7) into (2.8) and applying the result to (2.6) completes the proof. □

To this point we have assumed that the sampled function is bandlimited with bandregion $K \subset \widehat{G}$. The following lemma describes the function $S_M f$ with bandregion R computed from sampled values of a function f that is not necessarily bandlimited with bandregion $K \subseteq R$ but for which the Poisson summation formula holds.

Lemma 16. *Let H be a lattice and R a compact fundamental domain of $H^\perp$. Assume $f \in L^1(G)$ continuous, that the function $y \mapsto f(x_0+y)$ belongs to $L^1(H)$, and the Poisson summation formula (1.9) holds for a.e. $\xi \in R$. Then the function*

$$S_M f(x) = \sum_{y \in H} f(x_0+y)\phi_R(x-x_0-y), \quad x \in G \tag{2.9}$$

with ϕ_R defined in (1.13) is continuous, square integrable, and satisfies $S_M f(w) = f(w)$ for all $w \in M = x_0 + H$. Furthermore,

$$(S_M f)\widehat{\ }(x) = \chi_R(\xi) \sum_{\eta \in H^\perp} \hat{f}(\xi+\eta) e^{2\pi i \langle x_0, \eta \rangle} \tag{2.10}$$

for a.e. $\xi \in R$, where χ_R is the indicator function of R.

Proof. Define for $\xi \in \widehat{G}$ the function

$$h(\xi) = \frac{1}{m_{\widehat{G}}(R)} \chi_R(\xi) \sum_{y \in H} f(x_0+y) e^{-2\pi i \langle x_0+y, \xi \rangle}. \tag{2.11}$$

Then h converges uniformly on $\widehat{G}$ since for arbitrary $H^* \subset H$

$$\begin{aligned} &\Big| h(\xi) - \frac{1}{m_{\widehat{G}}(R)} \chi_R(\xi) \sum_{y \in H^*} f(x_0+y) e^{-2\pi i \langle x_0+y, \xi \rangle} \Big| \\ &\quad = \Big| \frac{1}{m_{\widehat{G}}(R)} \chi_R(\xi) \sum_{y \in H \setminus H^*} f(x_0+y) e^{-2\pi i \langle x_0+y, \xi \rangle} \Big| \\ &\quad \leq \frac{1}{m_{\widehat{G}}(R)} \sum_{y \in H \setminus H^*} |f(x_0+y)|, \end{aligned} \tag{2.12}$$

and the sum can be made arbitrarily small by the appropriate choice of H^*. The hypothesis that the samples $f(x_0+y)$, $y \in H$ are absolutely summable, and the facts $m_{\widehat{G}}(R) < \infty$ and $e^{-2\pi i\langle x_0+y,\xi\rangle}$ bounded imply that $h \in L^2(R) \subset L^1(R)$. It follows that $h \in L^1(\widehat{G}) \cap L^2(\widehat{G})$. Let $S_M f$ be the inverse Fourier transform of h. Then,

$$\begin{aligned} S_M f(x) &= \int_{\widehat{G}} \frac{1}{m_{\widehat{G}}(R)} \chi_R(\xi) \sum_{y\in H} f(x_0+y) e^{-2\pi i\langle x_0+y,\xi\rangle} e^{2\pi i\langle x,\xi\rangle}\, dm_{\widehat{G}}(\xi) \\ &= \frac{1}{m_{\widehat{G}}(R)} \int_R \sum_{y\in H} f(x_0+y) e^{2\pi i\langle x-x_0-y,\xi\rangle}\, dm_{\widehat{G}}(\xi) \\ &= \sum_{y\in H} f(x_0+y) \frac{1}{m_{\widehat{G}}(R)} \int_R e^{2\pi i\langle x-x_0-y,\xi\rangle}\, dm_{\widehat{G}}(\xi) \\ &= \sum_{y\in H} f(x_0+y)\phi_R(x-x_0-y), \end{aligned} \tag{2.13}$$

where the change in the order of summation and integration is due to uniform convergence of h and the fact that multiplication by a bounded function does not effect the convergence. Then $S_M f$ is continuous by construction, and the Plancherel theorem implies $S_M f$ is square integrable on G and $(S_M f)\widehat{\ }(\xi) = h(\xi)$ for a.e. $\xi \in R$. The fact that $S_M f(w) = f(w)$ for $w \in M = (x_0+H)$ follows from the property that $\phi_R(0) = 1$ and $\phi_R(y) = 0$ for $0 \neq y \in H$. Finally, (2.10) is obtained by applying the Poisson summation formula to (2.11) and using $(S_M f)\widehat{\ }(\xi) = h(\xi)$. □

If the function f is not bandlimited with bandregion K then the reconstruction formula in Corollary 15 can be used as an approximate reconstruction formula. We present the following estimate for the aliasing error committed when $\hat{f}$ does not vanish a.e. outside a bounded set $K \subset \widehat{G}$.

Theorem 17. *Let H_1, H_2 be lattices and $R_1 \subseteq R_2$ fundamental domains of $H_1^\perp, H_2^\perp$, respectively. Assume R_2 is contained in a finite number of translates of R_1 by*

elements of $H_1^\perp$ *and define* $K = R_2 \cup (\eta' + R_1)$ *with* $\eta' \in H_1^\perp \cap H_2^\perp$. *Let* $x_1, x_2 \in G$ *be such that* $\langle x_1 - x_2, \eta' \rangle \neq 0$. *Assume* $f \in L^1(G)$ *is continuous and such that* $\hat{f} \in L^1(\widehat{G})$, *the function* $y \mapsto f(x_1+y)$ *belongs to* $L^1(H_1)$, *the function* $z \mapsto f(x_2+z)$ *belongs to* $L^1(H_2)$, *and the Poisson summation formula (1.9) holds for a.e.* $\xi \in R_1$ *with* $H = H_1$ *and* $x = x_1$ *as well as for a.e.* $\xi \in R_2$ *with* $H = H_2$ *and* $x = x_2$. *Define for* $x \in G$,

$$\begin{aligned} Sf(x) = S_M f(x) + \beta \left(1 - e^{2\pi i \langle x - x_2, \eta' \rangle}\right) \\ \times \sum_{y \in H_1} (f - S_M f)(x_1 + y) \phi_{R_1}(x - x_1 - y), \end{aligned} \tag{2.14}$$

with β, $S_M f$, *defined in Corollary 15. Then*

$$|Sf(x) - f(x)| \leq (2 + 4|\beta|) \int_{\widehat{G} \setminus K} |\hat{f}(\xi)| \, dm_{\widehat{G}}(\xi). \tag{2.15}$$

for all $x \in G$.

Proof. Compute the Fourier transform of Sf. Let $g_1(x) = S_M f(x)$,

$$g_2(x) = \beta \left(1 - e^{2\pi i \langle x - x_2, \eta' \rangle}\right) \sum_{y \in H_1} f(x_1 + y) \phi_{R_1}(x - x_1 - y), \tag{2.16}$$

and

$$g_3(x) = -\beta \left(1 - e^{2\pi i \langle x - x_2, \eta' \rangle}\right) \sum_{y \in H_1} S_M f(x_1 + y) \phi_{R_1}(x - x_1 - y). \tag{2.17}$$

Then $(Sf)\widehat{\ } = \widehat{g}_1 + \widehat{g}_2 + \widehat{g}_3$. Applying Lemma 16 with $H = H_1$ or $H = H_2$ accordingly, we obtain

$$\widehat{g}_1(\xi) = \chi_{R_2}(\xi) \sum_{\zeta \in H_2^\perp} \hat{f}(\xi + \zeta) e^{2\pi i \langle x_2, \zeta \rangle}, \tag{2.18}$$

and

$$\begin{aligned} \widehat{g}_2(\xi) = \beta \chi_{R_1}(\xi) \sum_{\eta \in H_1^\perp} \hat{f}(\xi + \eta) e^{2\pi i \langle x_1, \eta \rangle} \\ - \beta e^{-2\pi i \langle x_2, \eta' \rangle} \chi_{R_1}(\xi - \eta') \sum_{\eta \in H_1^\perp} \hat{f}(\xi - \eta' + \eta) e^{2\pi i \langle x_1, \eta \rangle}. \end{aligned} \tag{2.19}$$

Absorbing the $-\eta'$ into the summation over $H_1^\perp$ and using $-\beta e^{2\pi i\langle x_1-x_2,\eta'\rangle} = (1-\beta)$, we obtain

$$\begin{aligned}\widehat{g}_2(\xi) = \beta\chi_{R_1}(\xi)\sum_{\eta\in H_1^\perp}\hat{f}(\xi+\eta)e^{2\pi i\langle x_1,\eta\rangle} \\ + (1-\beta)\chi_{R_1+\eta'}(\xi)\sum_{\eta\in H_1^\perp}\hat{f}(\xi+\eta)e^{2\pi i\langle x_1,\eta\rangle}.\end{aligned} \tag{2.20}$$

Since $(S_M f)\widehat{\ }$ vanishes outside $R_2 \subseteq \cup_{j=1}^P(\eta_j + R_1)$ with $\eta_j \in H_1^\perp$, $j = 1\ldots P < \infty$, Corollary 9 and Lemma 16 imply that $g_3 \in L^2(G)$. Then

$$\begin{aligned}\widehat{g}_3(\xi) = -\beta\chi_{R_1}(\xi)\sum_{\eta\in H_1^\perp}\chi_{R_2}(\xi+\eta)\sum_{\zeta\in H_2^\perp}\hat{f}(\xi+\eta+\zeta)e^{2\pi i\langle x_1,\eta\rangle}e^{2\pi i\langle x_2,\zeta\rangle} \\ - (1-\beta)\chi_{R_1+\eta'}(\xi)\sum_{\eta\in H_1^\perp}\chi_{R_2}(\xi+\eta)\sum_{\zeta\in H_2^\perp}\hat{f}(\xi+\eta+\zeta)e^{2\pi i\langle x_1,\eta\rangle}e^{2\pi i\langle x_2,\zeta\rangle}.\end{aligned} \tag{2.21}$$

We wish to separate terms involving values $\hat{f}(\omega)$ for $\omega \in K = R_1 \cup (\eta' + R_1) \cup (R_2 \setminus R_1)$ from the remaining terms in each summation. This is possible since K is contained in only two translates of R_2 by elements of $H_2^\perp$, and R_2 is contained in only finitely many translates of R_1 by elements of $H_1^\perp$ by hypothesis. It is necessary to identify for each $\xi \in R_1$ the elements of $\{\eta_j\}_{j=1}^P \subset H_1^\perp$ for which $(\xi+\eta_j) \in R_2$. This leads to a partitioning of R_1.

We follow the method used in the discussion prior to Theorem 7 to identify the elements of $H^\perp$ producing the overlapping translates of K in periodic sampling. For each $\xi \in R_1$ define the set $d_\xi = H_1^\perp \cap (R_2 - \xi)$. The fact $R_1 \subset R_2$ implies $0 \in d_\xi \neq \emptyset$ for all $\xi \in R_1$. It follows, since $\eta' \in H_1^\perp \cap H_2^\perp$, that $\eta' \notin d_\xi$ for all $\xi \in R_1$. Since $R_2 \subseteq \cup_{j=1}^P(\eta_j + R_1)$ with $P < \infty$, $d_\xi \subseteq \{\eta_j\}_{j=1,\ldots,P}$ is finite and, as ξ runs through R_2, can assume only finitely many different values $d_1, \ldots, d_L$. Let $m_l = |d_l|$ and $d_l = \{\eta_j^{(l)}\}_{j=0}^{m_l-1}$, $l = 1, \ldots, L$. Without loss of generality, we take $\eta_0^{(l)} = 0$, $l = 1, \ldots, L$. The relation $\xi \equiv \xi' \leftrightarrow d_\xi = d_{\xi'}$ defines an equivalence relation

on R_1 induced by H_1, where the equivalence classes are $R_1^{(l)} = \{\xi \in R_1 : d_\xi = d_l\}$. The sets $R_1^{(l)}$, $l = 1, \ldots, L$ are mutually disjoint and $R_1 = \cup_{l=1}^{L} R_1^{(l)}$. Moreover, we have

$$R_2 = \cup_{l=1}^{L} \cup_{j=0}^{m_l - 1} \left(\eta_j^{(l)} + R_1^{(l)} \right). \tag{2.22}$$

We now decompose the summations in (2.18), (2.20), and (2.21) and separate terms involving $\hat{f}(\xi)$ with $\xi \in K$ from those with ξ outside of K. Then (2.18) is written

$$\begin{aligned} \widehat{g}_1(\xi) &= (\chi_{R_2 \setminus R_1}(\xi)) + \chi_{R_1}(\xi)) \sum_{\zeta \in H_2^\perp} \hat{f}(\xi + \zeta) e^{2\pi i \langle x_2, \zeta \rangle} \\ &= \chi_{R_2 \setminus R_1}(\xi) \left(\hat{f}(\xi) + \sum_{\zeta \in H_2^\perp \setminus \{0\}} \hat{f}(\xi + \zeta) e^{2\pi i \langle x_2, \zeta \rangle} \right) \\ &+ \chi_{R_1}(\xi) \left(\hat{f}(\xi) + \hat{f}(\xi + \eta') e^{2\pi i \langle x_2, \eta' \rangle} + \sum_{\zeta \in H_2^\perp \setminus \{0, \eta'\}} \hat{f}(\xi + \eta) e^{2\pi i \langle x_2, \zeta \rangle} \right). \end{aligned} \tag{2.23}$$

Using the partitioning $R_1 = \cup_{l=1}^{L} R_1^{(l)}$ described previously, (2.20) is written

$$\begin{aligned} \widehat{g}_2(\xi) &= \beta \chi_{R_1}(\xi) \left(\hat{f}(\xi) + \hat{f}(\xi + \eta') e^{2\pi i \langle x_1, \eta' \rangle} \right) \\ &+ \beta \sum_{l=1}^{L} \chi_{R_1^{(l)}}(\xi) \sum_{j=1}^{m_l - 1} \hat{f}(\xi + \eta_j^{(l)}) e^{2\pi i \langle x_1, \eta_j^{(l)} \rangle} \\ &+ \beta \sum_{l=1}^{L} \chi_{R_1^{(l)}}(\xi) \sum_{\eta \in H_1^\perp \setminus (d_l \cup \{\eta'\})} \hat{f}(\xi + \eta) e^{2\pi i \langle x_1, \eta \rangle} \\ &+ (1 - \beta) \chi_{\eta' + R_1}(\xi) \left(\hat{f}(\xi) + \hat{f}(\xi - \eta') e^{-2\pi i \langle x_1, \eta' \rangle} \right) \\ &+ (1 - \beta) \sum_{l=1}^{L} \chi_{\eta' + R_1^{(l)}}(\xi) \sum_{j=1}^{m_l - 1} \hat{f}(\xi + \eta_j^{(l)} - \eta') e^{2\pi i \langle x_1, \eta_j^{(l)} - \eta' \rangle} \\ &+ (1 - \beta) \sum_{l=1}^{L} \chi_{\eta' + R_1^{(l)}}(\xi) \sum_{\eta \in H_1^\perp \setminus (d_l \cup \{\eta'\})} \hat{f}(\xi + \eta - \eta') e^{2\pi i \langle x_1, \eta - \eta' \rangle}. \end{aligned} \tag{2.24}$$

The third and sixth terms involve values $\hat{f}(\omega)$ for which ω falls outside of K. In (2.21), we again use the partitioning $R_1 = \cup_{l=1}^{L} R_1^{(l)}$ but the inner characteristic function, $\chi_{R_2}(\xi+\eta)$, is nonzero for only finitely many elements $\eta_j^{(l)} \in H_1^{\perp}$. We then separate the relevant terms from the sum over $H_2^{\perp}$ and obtain

$$\begin{aligned}
\widehat{g}_3(\xi) = &-\beta\chi_{R_1}(\xi)\left(\hat{f}(\xi)+\hat{f}(\xi+\eta')e^{2\pi i\langle x_2,\eta'\rangle}\right)\\
&-\beta\chi_{R_1}(\xi)\sum_{\zeta\in H_2^{\perp}\setminus\{0,\eta'\}}\hat{f}(\xi+\zeta)e^{2\pi i\langle x_2,\zeta\rangle}\\
&-\beta\sum_{l=1}^{L}\chi_{R_1^{(l)}}(\xi)\sum_{j=1}^{m_l-1}\hat{f}(\xi+\eta_j^{(l)})e^{2\pi i\langle x_1,\eta_j^{(l)}\rangle}\\
&-\beta\sum_{l=1}^{L}\chi_{R_1^{(l)}}(\xi)\sum_{j=1}^{m_l-1}\sum_{\zeta\in H_2^{\perp}\setminus\{0\}}\hat{f}(\xi+\eta_j^{(l)}+\zeta)e^{2\pi i\langle x_1,\eta_j^{(l)}\rangle}e^{2\pi i\langle x_2,\zeta\rangle}\\
&-(1-\beta)\chi_{\eta'+R_1}(\xi)\left(\hat{f}(\xi-\eta')e^{-2\pi i\langle x_1,\eta'\rangle}+\hat{f}(\xi)e^{-2\pi i\langle x_1-x_2,\eta'\rangle}\right)\\
&-(1-\beta)\chi_{\eta'+R_1}(\xi)\sum_{\zeta\in H_2^{\perp}\setminus\{0,\eta'\}}\hat{f}(\xi-\eta'+\zeta)e^{-2\pi i\langle x_1,\eta'\rangle}e^{2\pi i\langle x_2,\zeta\rangle}\\
&-(1-\beta)\sum_{l=1}^{L}\chi_{\eta'+R_1^{(l)}}(\xi)\sum_{j=1}^{m_l-1}\hat{f}(\xi+\eta_j^{(l)}-\eta')e^{2\pi i\langle x_1,\eta_j^{(l)}-\eta'\rangle}\\
&-(1-\beta)\sum_{l=1}^{L}\chi_{\eta'+R_1^{(l)}}(\xi)\sum_{j=1}^{m_l-1}\sum_{\zeta\in H_2^{\perp}\setminus\{0\}}\hat{f}(\xi+\eta_j^{(l)}-\eta'+\zeta)e^{2\pi i\langle x_1,\eta_j^{(l)}-\eta'\rangle}e^{2\pi i\langle x_2,\zeta\rangle}.
\end{aligned} \tag{2.25}$$

Next, using (2.23),(2.24), and (2.25), we compute $(Sf)\widehat{\ } = \widehat{g}_1+\widehat{g}_2+\widehat{g}_3$. We collect terms involving $\hat{f}$ on R_1, $(\eta'+R_1)$, and $(R_2\setminus R_1)$ and observe the cancellation on these sets. We use the facts that $(1-\beta)e^{-2\pi i\langle x_1-x_2,\eta'\rangle} = -\beta$ and that $\beta(e^{2\pi i\langle x_1,\eta'\rangle} - e^{2\pi i\langle x_2,\eta'\rangle}) = -e^{2\pi i\langle x_2,\eta'\rangle}$. and collect the remaining terms involving $\hat{f}$ on translates

of R_1, $(\eta' + R_1)$, and $(R_2 \setminus R_1)$ outside of K. Then $(Sf)\hat{}$ may now be written

$$\begin{aligned}
(Sf)\hat{}(\xi) &= \chi_K(\xi)\hat{f}(\xi) + (1-\beta)\chi_{R_1}(\xi) \sum_{\zeta \in H_2^\perp \setminus \{0,\eta'\}} \hat{f}(\xi+\zeta) e^{2\pi i \langle x_2, \zeta \rangle} \\
&- (1-\beta)\chi_{\eta'+R_1}(\xi) \sum_{\zeta \in H_2^\perp \setminus \{0,\eta'\}} \hat{f}(\xi-\eta'+\zeta) e^{-2\pi i \langle x_1, \eta' \rangle} e^{2\pi i \langle x_2, \zeta \rangle} \\
&+ \chi_{R_2 \setminus R_1}(\xi) \sum_{\zeta \in H_2^\perp \setminus \{0\}} \hat{f}(\xi+\zeta) e^{2\pi i \langle x_2, \zeta \rangle} \\
&+ \beta \sum_{l=1}^{L} \chi_{R_1^{(l)}}(\xi) \sum_{\eta \in H_1^\perp \setminus (d_l \cup \{\eta'\})} \hat{f}(\xi+\eta) e^{2\pi i \langle x_1, \eta \rangle} \\
&+ (1-\beta) \sum_{l=1}^{L} \chi_{\eta'+R_1^{(l)}}(\xi) \sum_{\eta \in H_1^\perp \setminus (d_l \cup \{\eta'\})} \hat{f}(\xi+\eta-\eta') e^{2\pi i \langle x_1, \eta-\eta' \rangle} \\
&- \beta \sum_{l=1}^{L} \chi_{R_1^{(l)}}(\xi) \sum_{j=1}^{m_l-1} \sum_{\zeta \in H_2^\perp \setminus \{0\}} \hat{f}(\xi+\eta_j^{(l)}+\zeta) e^{2\pi i \langle x_1, \eta_j^{(l)} \rangle} e^{2\pi i \langle x_2, \zeta \rangle} \\
&- (1-\beta) \sum_{l=1}^{L} \chi_{\eta'+R_1^{(l)}}(\xi) \sum_{j=1}^{m_l-1} \sum_{\zeta \in H_2^\perp \setminus \{0\}} \hat{f}(\xi+\eta_j^{(l)}-\eta'+\zeta) e^{2\pi i \langle x_1, \eta_j^{(l)}-\eta' \rangle} e^{2\pi i \langle x_2, \zeta \rangle}.
\end{aligned} \tag{2.26}$$

Notice that $(Sf)\hat{}$ vanishes outside K. To compute the aliasing error we use the fact

$$\begin{aligned}
|Sf(x) - f(x)| &\leq \| (Sf)\hat{} - \hat{f} \|_1 \\
&= \int_{\widehat{G}} |(Sf)\hat{}(\xi) - \hat{f}(\xi)| \, dm_{\widehat{G}}(\xi) \\
&= \int_K |(Sf)\hat{}(\xi) - \hat{f}(\xi)| \, dm_{\widehat{G}}(\xi) + \int_{\widehat{G}\setminus K} |\hat{f}(\xi)| \, dm_{\widehat{G}}(\xi)
\end{aligned} \tag{2.27}$$

for all $x \in G$. Substituting (2.26) in the integral over K and using $|1-\beta| = |\beta|$, we

obtain

$$\begin{aligned}\int_K |(Sf)\hat{}(\xi) - \hat{f}(\xi)|\, dm_{\widehat{G}}(\xi) \leq 2|\beta| &\sum_{\zeta\in H_2^\perp\setminus\{0,\eta'\}} \int_{\zeta+R_1} |f(\xi)|\, dm_{\widehat{G}}(\xi) \\ &+ \sum_{\zeta\in H_2^\perp\setminus\{0\}} \int_{\zeta+(R_2\setminus R_1)} |f(\xi)|\, dm_{\widehat{G}}(\xi) \\ &+ 2|\beta| \sum_{l=1}^{L} \sum_{\eta\in H_1^\perp\setminus(d_l\cup\{\eta'\})} \int_{\eta+R_1^{(l)}} |f(\xi)|\, dm_{\widehat{G}}(\xi) \\ &+ 2|\beta| \sum_{l=1}^{L} \sum_{j=1}^{m_l-1} \sum_{\zeta\in H_2^\perp\setminus\{0\}} \int_{\zeta+\eta_j^{(l)}+R_1^{(l)}} |f(\xi)|\, dm_{\widehat{G}}(\xi).\end{aligned} \tag{2.28}$$

The change in the order of summation and integration is due to the convergence of $(Sf)\hat{}$ shown in Lemma 16. Finally, notice that the sets $(\zeta+R_1)$ for $\zeta \in H_2^\perp\setminus\{0,\eta'\}$ and the sets $\cup_{l=1}^{L}\cup_{j=1}^{m_l-1}(\zeta+\eta_j^{(l)}+R_1^{(l)})$ for $\zeta \in H_2^\perp\setminus\{0\}$ interlace to form one complete covering of $\widehat{G}\setminus K$. The sets $\cup_{l=1}^{L}(\eta+R_1^{(l)})$ for $\eta \in H_1^\perp\setminus(d_l\cup\{\eta'\})$ form a second cover of $\widehat{G}\setminus K$. The remaining set, $(\zeta + R_2 \setminus R_1)$ for $\zeta \in H_2^\perp \setminus \{0\}$ does not completely cover $\widehat{G}\setminus K$. Thus

$$\int_K |(Sf)\hat{}(\xi) - \hat{f}(\xi)|\, dm_{\widehat{G}}(\xi) \leq (1+4|\beta|) \int_{\widehat{G}\setminus K} \left|\hat{f}(\xi)\right|\, dm_{\widehat{G}}(\xi). \tag{2.29}$$

Substituting (2.29) into (2.27) completes the proof. □

The result of Theorem 17 implies that $|\beta|$ acts as an amplification factor of the aliasing error committed by (2.4) when $\hat{f}$ does not vanish a.e outside the set K. If x_1, x_2 are such that $\langle x_1 - x_2, \eta'\rangle$ is close to zero, then $|\beta|$ is large, and the interpolation process based on (2.14) may then be unreliable.

We may compare the results of Theorem 17 with the results of Theorem 7 and Theorem 8 in the case $H_1 = H_2 = H$, or periodic sampling. The condition $R_1 \subseteq R_2$

implies that $R_1 = R_2 = R$, thus $R_2 \setminus R_1 = \emptyset$ and the partitioning of R_1 used in (2.22) is trivial. Then (2.14) may be written

$$\begin{aligned} Sf(x) = S_M f(x) &+ \beta\left(1 - e^{2\pi i\langle x-x_2,\eta'\rangle}\right)\sum_{y\in H} f(x_1+y)\phi_R(x-x_1-y) \\ &- \beta\left(1 - e^{2\pi i\langle x-x_2,\eta'\rangle}\right)\sum_{y\in H} S_M f(x_1+y)\phi_R(x-x_1-y). \end{aligned} \tag{2.30}$$

By Lemma 16 and Kluvánek's Theorem 6 we have $\sum_{y\in H} S_M f(x_1+y)\phi_R(x-x_1-y) = S_M f(x)$. Thus

$$\begin{aligned} Sf(x) = \beta&\sum_{y\in H} f(x_1+y)\phi_R(x-x_1-y) \\ &- \beta e^{2\pi i\langle x-x_2,\eta'\rangle}\sum_{y\in H} f(x_1+y)\phi_R(x-x_1-y) \\ &+ (1-\beta)\sum_{y\in H} f(x_2+y)\phi_R(x-x_2-y) \\ &+ \beta e^{2\pi i\langle x-x_2,\eta'\rangle}\sum_{y\in H} f(x_2+y)\phi_R(x-x_2-y). \end{aligned} \tag{2.31}$$

Using the facts $\eta' \in H^\perp$ and $-\beta e^{2\pi i\langle x-x_2,\eta'\rangle} = (1-\beta)e^{2\pi i\langle x-x_1,\eta'\rangle}$ we may rewrite the summations in the form

$$\begin{aligned} Sf(x) = &\sum_{y\in H} f(x_1+y)\left(\beta\phi_R(x-x_1-y) + (1-\beta)\phi_R(x-x_1-y)e^{2\pi i\langle x-x_1-y,\eta'\rangle}\right) \\ &+ \sum_{y\in H} f(x_2+y)\left((1-\beta)\phi_R(x-x_2-y) + \beta\phi_R(x-x_2-y)e^{2\pi i\langle x-x_2-y,\eta'\rangle}\right). \end{aligned} \tag{2.32}$$

Letting

$$\begin{aligned} k_1(z) &= \beta\phi_R(z) + (1-\beta)\phi_R(z)e^{2\pi i\langle z,\eta'\rangle} \\ &= \beta\frac{1}{m_{\widehat{G}}(R)}\int_R e^{2\pi i\langle z,\xi\rangle}\, dm_{\widehat{G}}(\xi) + (1-\beta)\frac{1}{m_{\widehat{G}}(R)}\int_{\eta'+R} e^{2\pi i\langle z,\xi\rangle}\, dm_{\widehat{G}}(\xi) \end{aligned} \tag{2.33}$$

and

$$\begin{aligned} k_2(z) &= (1-\beta)\phi_R(z) + \beta\phi_R(z)e^{2\pi i\langle z,\eta'\rangle} \\ &= (1-\beta)\frac{1}{m_{\widehat{G}}(R)}\int_R e^{2\pi i\langle z,\xi\rangle}\, dm_{\widehat{G}}(\xi) + \beta\frac{1}{m_{\widehat{G}}(R)}\int_{\eta'+R} e^{2\pi i\langle z,\xi\rangle}\, dm_{\widehat{G}}(\xi), \end{aligned} \tag{2.34}$$

we obtain the reconstruction formula

$$Sf(x) = \sum_{n=1}^{2}\sum_{y\in H} f(x_n+y)k_n(x-x_n-y) \tag{2.35}$$

given in Theorem 7 with the index n shifted by one. The weights $\beta_1^{(1)} = \beta_2^{(2)} = \beta$ and $\beta_1^{(2)} = \beta_2^{(1)} = (1-\beta)$ satisfy the systems in (1.18) with $m_1 = m_2 = \overline{m} = 2$ and $\eta_1^{(1)} = \eta'$ and $\eta_1^{(2)} = -\eta'$. It follows that $\gamma = \overline{m}(\max_{l=1,\ldots,L}\sum_{n=1}^{2}|\beta_n^{(l)}|) = 4|\beta|$. Since $R_2 \setminus R_1 = \emptyset$ the corresponding integral in (2.28) vanishes and we obtain

$$\int_K |(Sf)\hat{}(\xi) - \hat{f}(\xi)|\, dm_{\widehat{G}}(\xi) \le \gamma \int_{\widehat{G}\setminus K} \left|\hat{f}(\xi)\right|\, dm_{\widehat{G}}(\xi). \tag{2.36}$$

Substituting (2.36) into (2.27) yields the result of Theorem 8.

2.2 Implementation

We now apply the nonperiodic sampling theorem to obtain an interpolation algorithm which exploits the symmetry property in fan beam CT and accurately determines the values of the data function on a single lattice with twice the density of the standard sampling lattice H_S. The filtered back-projection algorithm is then used to reconstruct the object with higher resolution than the standard reconstruction. The interpolation algorithm involves a novel decomposition of the set K_τ defined in (1.44) such that K_τ is contained in the union of a fundamental domain R of $H_S^\perp$ and a set $(\eta' + K')$ with $K' \subset R$ and $\eta' \in H_S^\perp$.

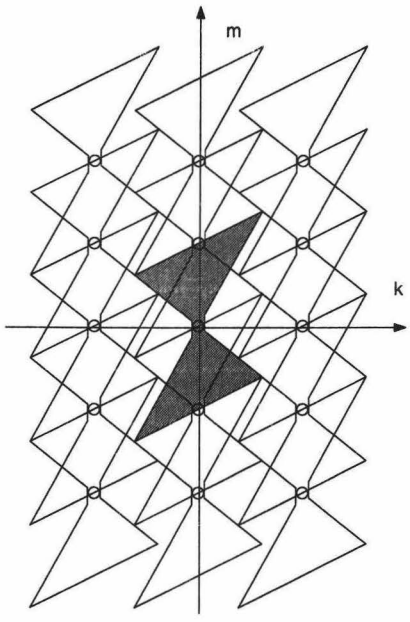

Figure 2.1: Some translates of K_τ by elements of $H_S^\perp$.

Consider the standard sampling scheme on $\mathbb{T}^2$ which undersamples the function $g(u,v)$ with bandregion K_τ by a factor of $1/2$ in the second coordinate, i.e. $N_2 = r\Omega/2$. Then translates of K_τ by elements of $H_S^\perp$ intersect. We may choose N_1 such that intersections involve only translates of K_τ by elements of $H_S^\perp$ which are zero in the first coordinate. The minimum value of N_1 is obtained by observing the coincidence of the boundaries of translates of K_τ and depends on the scanning geometry according to

$$N_1 \geq \begin{cases} N_2\left(\frac{4\vartheta}{1+\vartheta}\right), & 0 < \vartheta \leq 1/3, \\ N_2\left(\frac{2\vartheta}{1-\vartheta}\right), & 1/3 < \vartheta \leq 1/2, \\ N_2\left(\frac{6\vartheta}{1+\vartheta}\right), & 1/2 < \vartheta < 1, \end{cases} \tag{2.37}$$

with $\vartheta = \tau^{-1}(\rho/r)$ [13]. Then translates of K_τ by elements of $(H_S^\perp \setminus \{0\})$ overlap

K_τ in only two regions. They are $K_\tau \cap ((0, N_2)^T + K_\tau)$ and $K_\tau \cap ((0, -N_2)^T + K_\tau)$. See figure 2.1. We will use the values of g on the reflected sampling set, obtained using the symmetry property, and nonperiodic sampling theory to recover $\hat{g}$ on these overlapping regions.

We choose to consider undersampling of g in the direction of the second coordinate for several reasons. In modern CT scanners, the detector consists of a fixed array of cells of finite width. Sampling schemes which involve increasing the number or changing the positions of these cells are difficult, if not impossible, in practice. It is more reasonable to select the number of views taken as the source rotates about the object. Also, with finite detector width, measurements of g consist of averages of integrals over all rays striking a detector. This averaging effectively bandlimits the data function. It can be reasonably argued, however, that the bandwidth is twice that which can be recovered from a set of measurements by adjacent detectors. This is the so-called third generation undersampling problem. By overcoming undersampling of g in the second coordinate, i.e. detector direction, we solve this problem. In addition, due to the interlocking, bow-tie shape of the set K_τ, undersampling g in the first coordinate and allowing only intersections of translates of K_τ by elements of $H_S^\perp$ which are zero in the second coordinate would require oversampling g in the second coordinate. Since the detector array is fixed, oversampling in the detector direction means we must assume a smaller bandregion of g and reduce the resolution of the reconstruction. Since the goal is to reconstruct the object with the highest resolution possible, we do not consider undersampling in the first coordinate. Finally, notice that the annihilators $H_S^\perp$ and $H_R^\perp$ of H_S and H_R, respectively, coincide for all $\eta \in H_S^\perp$ zero on the first coordinate. This allows us to use the simplified version of the nonperiodic sampling theorem presented in

Corollary 15. This is generally not the case for η nonzero in the first coordinate.

Let $\eta' = (0, -N_2)^T$. We may construct fundamental domains R_1 and R_2 of $H_R^\perp$ and $H_S^\perp$, respectively, such that $K_\tau \subseteq R_2 \cup (\eta' + K')$ with $K' \subseteq R_2 \cap R_1$. The exact shapes of R_2 and R_1 are determined by the sampling parameters (N_1, N_2) which, in turn, depend on the parameters r, ρ, Ω, and τ. Before we construct the sets R_1 and R_2, we prove the following claim regarding the canonical fundamental domain of both $H_R^\perp$ and $H_S^\perp$.

Claim 18. *Let N_1, N_2 be integers and let $a =$ mod (N_1, N_2) be the unique integer such that $0 \leq a < N_1$ and $N_1 - a \in N_2\mathbb{Z}$. The set $D = [0, \ldots, N_1 - 1] \times [0, \ldots, N_2 - 1] \subset \mathbb{Z}^2$ is a fundamental domain of both $H_2^\perp = \{(jN_1, lN_2)^T : j, l \in \mathbb{Z}\}$ and $H_1^\perp = \{(jN_1, ja + lN_2)^T : j, l \in \mathbb{Z}\}$.*

Proof. Given $(n_1, n_2)^T \in \mathbb{Z}^2$, let $n_1' =$ mod (n_1, N_1) be the unique integer such that $0 \leq n_1' < N_1$ and $n_1 - n_1' \in N_1\mathbb{Z}$. Then there exists a unique integer j such that $n_1 = n_1' + jN_1$. Now let $n_2' =$ mod (n_2, N_2) be the unique integer such that $0 \leq n_2' < N_2$ and $n_2 - n_2' \in N_2\mathbb{Z}$ and let $n_2'' =$ mod $(n_2 - ja, N_2)$ be the unique integer such that $0 \leq n_2'' < N_2$ and $n_2 - ja - n_2'' \in N_2\mathbb{Z}$. Then there exist unique integers l, l' such that $(n_1, n_2)T = (n_1', n_2')^T + (jN_1, lN_2)^T$ and $(n_1, n_2)^T = (n_1', n_2'')^T + (jN_1, ja + l'N_2)^T$. Thus D is a fundamental domain of both $H_2^\perp$ and $H_1^\perp$. □

We call D the canonical fundamental domain of $H_2^\perp$ and $H_1^\perp$. We may now construct fundamental domains R_2 and R_1 of $H_2^\perp$ and $H_1^\perp$, respectively, buy defining one-to-one mappings of D onto R_2 and R_1.

Proposition 19. *Let r, ρ, Ω, and τ be such that τ is close to 1 and $0 < \vartheta < 1/2$ where $\vartheta = \tau^{-1}\rho/r$ and let $K_\tau(r, \rho, \Omega)$ be defined as in (1.44). Let $N_2 = r\Omega/2$ and*

choose N_1 such that (2.37) is satisfied and N_1 is near the minimum value. Then there exist fundamental domains R_2 and R_1 of $H_2^\perp = \{(jN_1, lN_2)^T : j,l \in \mathbb{Z}\}$ and $H_1^\perp = \{(jN_1, ja+lN_2)^T : j,l \in \mathbb{Z}\}$, respectively, such that $K_\tau(r,\rho,\Omega) \subseteq R_2 \cup (\eta' + K')$ with $\eta' = (0,N_2)^T \in H_2^\perp \cap H_1^\perp$ and $K' \subseteq R_2 \cap R_1$.

We do not mean to suggest that that the result is not true for $1/2 \leq \vartheta < 1$, but that in this case the construction of the sets R_1 and R_2 differs somewhat from the construction of R_1 and R_2 in the case $0 < \vartheta \leq 1/2$. In many, if not all, practical situations, $\vartheta < 1/2$. For this reason, we omit the discussion of the case $1/2 < \vartheta < 1$.

Proof. We construct sets R_1 and R_2 by defining one-to-one mappings p_1 and p_2 from the canonical fundamental domain D of both $H_1^\perp$ and $H_2^\perp$ onto the sets R_1 and R_2, respectively. The mappings p_1 and p_2 involve only translations of the elements of D by elements of $H_1^\perp$ and $H_2^\perp$, respectively. It follows that R_1 and R_2 are fundamental domains of $H_1^\perp$ and $H_2^\perp$, respectively. We then show that the set K_τ in (1.44) is contained in both $(R_2 \cup (\eta' + R_2))$ and $(R_2 \cup (\eta' + R_2))$. It follows that $K_\tau \subseteq (R_2 \cup (\eta' + K'))$ with $K' \subseteq R_1 \cap R_2$.

Define for each $(n_1,n_2)^T \in D$ the mapping $p_2(n_1,n_2) = (n_1,n_2)^T + \eta_{n_1,n_2}$ where: $\eta_{n_1,n_2} = (-N_1,0)^T$ if $(n_2 - N_2) < (1/2)(n_1 - N_1)$ and

$$\begin{cases} 0 \leq n_2 < N_2/3 \text{ and } (n_2 + N_2) \leq n_1(2N_2/N_1), \text{ or} \\ N_2/3 \leq n_2 < 2N_2/3 \text{ and } (n_2 - N_2) \geq n_1(-N_2/N_1), \text{ or} \\ 2N_2/3 \leq n_2 < N_2 \text{ and } n_2 \leq n_1(2N_2/N_1); \end{cases} \tag{2.38}$$

and $\eta_{n_1,n_2} = (-N_1,-N_2)^T$ if $(n_2 - N_2) \geq (1/2)(n_1 - N_1)$ and

$$\begin{cases} 0 \leq n_2 < N_2/3 \text{ and } (n_2 + N_2) \leq n_1(2N_2/N_1), \text{ or} \\ N_2/3 \leq n_2 < 2N_2/3 \text{ and } (n_2 - N_2) \geq n_1(-N_2/N_1), \text{ or} \\ 2N_2/3 \leq n_2 < N_2 \text{ and } n_2 \leq n_1(2N_2/N_1); \end{cases} \tag{2.39}$$

and $\eta_{n_1,n_2} = (0, N_2)^T$ if $n_2 < (1/2)n_1$ and

$$\begin{cases} 0 \le n_2 < N_2/3 \text{ and } (n_2 + N_2) > n_1(2N_2/N_1), \text{ or} \\ N_2/3 \le n_2 < 2N_2/3 \text{ and } (n_2 - N_2) < n_1(-N_2/N_1), \text{ or} \\ 2N_2/3 \le n_2 < N_2 \text{ and } n_2 > n_1(2N_2/N_1); \end{cases} \tag{2.40}$$

and $\eta_{n_1,n_2} = (0,0)^T$, otherwise. Then the set $R_2 = \{p_2(n_1, n_2) : (n_1, n_2) \in D\}$ is a fundamental domain of R_2.

If $0 < \vartheta < 1/3$, then by (2.37), $a =$ mod $(N_1, N_2) = N_1$. Let $m_1 = (a + N_2)/N_1$ and $m_2 = (a - 2N_2)/N_1$ and let $c_1 = (2a - N_2)/3$ and $c_2 = (a + N_2)/3$. Define for each $(n_1, n_2)^T \in D$ the mapping $p_1(n_1, n_2) = (n_1, n_2)^T + \zeta_{n_1,n_2}$ where: $\zeta_{n_1,n_2} = (-N_1, -a + N_2)^T$ if $(n_2 - a) < (1/2)(n_1 - N_1)$ and

$$\begin{cases} 0 \le n_2 < c_1 \text{ and } (n_2 + N_2) \le m_1 n_1, \text{ or} \\ c_1 \le n_2 < c_2 \text{ and } (n_2 - N_2) \ge m_2 n_1, \text{ or} \\ c_2 \le n_2 < N_2 \text{ and } n_2 \le m_1 n_1; \end{cases} \tag{2.41}$$

and $\zeta_{n_1,n_2} = (-N_1, -a)^T$ if $(n_2 - a) \ge (1/2)(n_1 - N_1)$ and

$$\begin{cases} 0 \le n_2 < c_1 \text{ and } (n_2 + N_2) \le m_1 n_1, \text{ or} \\ c_1 \le n_2 < c_2 \text{ and } (n_2 - N_2) \ge m_2 n_1, \text{ or} \\ c_2 \le n_2 < N_2 \text{ and } n_2 \le m_1 n_1; \end{cases} \tag{2.42}$$

and $\zeta_{n_1,n_2} = (0, N_2)^T$ if $n_2 < (1/2)n_1$ and

$$\begin{cases} 0 \le n_2 < c_1 \text{ and } (n_2 + N_2) > m_1 n_1, \text{ or} \\ c_1 \le n_2 < c_2 \text{ and } (n_2 - N_2) < m_2 n_1, \text{ or} \\ c_2 \le n_2 < N_2 \text{ and } n_2 > m_1 n_1; \end{cases} \tag{2.43}$$

and $\zeta_{n_1,n_2} = (0,0)^T$, otherwise. Then the set $R_1 = \{p_1(n_1, n_2) : (n_1, n_2) \in D\}$ is a fundamental domain of R_1.

If $1/3 \leq \vartheta < 1/2$, then by (2.37), $a = \mod(N_1, N_2) = N_1 - N_2$. Let $m_1 = (a+2N_2)/N_1$ and $m_2 = (a-N_2)/N_1$ and let $c_1 = (2a+N_2)/3$ and $c_2 = (a+2N_2)/3$. Define for each $(n_1, n_2)^T \in D$ the mapping $p_1(n_1, n_2) = (n_1, n_2)^T + \zeta_{n_1,n_2}$ where: $\zeta_{n_1,n_2} = (-N_1, -a)^T$ if $(n_2 - a) \geq (1/2)(n_1 - N_1)$ and

$$\begin{cases} 0 \leq n_2 < c_1 \text{ and } (n_2 + N_2) \leq m_1 n_1, \text{ or} \\ c_1 \leq n_2 < c_2 \text{ and } (n_2 - N_2) \geq m_2 n_1, \text{ or} \\ c_2 \leq n_2 < N_2 \text{ and } n_2 \leq m_1 n_1; \end{cases} \tag{2.44}$$

and $\zeta_{n_1,n_2} = (-N_1, -a + N_2)^T$ if $(n_2 - a) < (1/2)(n_1 - N_1)$ and

$$\begin{cases} 0 \leq n_2 < c_1 \text{ and } (n_2 + N_2) \leq m_1 n_1, \text{ or} \\ c_1 \leq n_2 < c_2 \text{ and } (n_2 - N_2) \geq m_2 n_1, \text{ or} \\ c_2 \leq n_2 < N_2 \text{ and } n_2 \leq m_1 n_1; \end{cases} \tag{2.45}$$

and $\zeta_{n_1,n_2} = (0, N_2)^T$ if $n_2 < (1/2)n_1$ and

$$\begin{cases} 0 \leq n_2 < c_1 \text{ and } (n_2 + N_2) > m_1 n_1, \text{ or} \\ c_1 \leq n_2 < c_2 \text{ and } (n_2 - N_2) < m_2 n_1, \text{ or} \\ c_2 \leq n_2 < N_2 \text{ and } n_2 > m_1 n_1; \end{cases} \tag{2.46}$$

and $\zeta_{n_1,n_2} = (0, 0)^T$, otherwise. Then the set $R_1 = \{p_1(n_1, n_2) : (n_1, n_2) \in D\}$ is a fundamental domain of R_1.

To show that $K_\tau \subseteq R_2 \cup (\eta' + R_2)$ and $K_\tau \subseteq R_2 \cup (\eta' + R_1)$ and, hence, $K_\tau \subseteq R_2 + (\eta' + K')$ with $K' \subseteq R_2 \cap R_1$, it suffices to show that the boundaries of the set K_τ are contain the boundaries of the sets $R_2 \cup (\eta' + R_2)$ and $R_1 \cup (\eta' + R_1)$ and that the sets R_2 and $\eta' + R_1$ are disjoint.

For $0 < \vartheta < 1/2$, we may express the boundaries of the bowtie shaped set K_τ by the lines $m = k(\vartheta - 1)/(2\vartheta)$, $m = k(\vartheta + 1)/(2\vartheta)$, $m = N_2 + (1/2)k$, and

$m = -N_2 + (1/2)k$. With τ chosen close to 1 we need not consider the boundaries $|k| = (1-\tau)\rho\Omega$.

If $0 < \vartheta < 1/3$ then by (2.37), $N_1 \geq N_2(4\vartheta)/(1+\vartheta)$. The set R_2 has a boundary with slope $2N_2/N_1 \leq 2N_2/(N_2(4\vartheta)/(1+\vartheta)) = (\vartheta+1)/(2\vartheta)$. The corresponding boundaries of $R_2 \cup (\eta' + R_2)$ then contain the boundaries of K_τ with slope $(\vartheta + 1)/(2\vartheta)$. The set R_2 has a boundary with slope $-N_2/N_1 \geq -N_2/(N_2(4\vartheta)/(1+\vartheta)) = (-\vartheta 11)/(2\vartheta) = (2\vartheta - 2)/(4\vartheta) + (1-3\vartheta)/(4\vartheta) > (\vartheta - 1)/(2\vartheta)$, since $\vartheta < 1/3$. The corresponding boundaries of $R_2 \cup (\eta' + R_2)$ then contain the boundaries of K_τ with slope $(\vartheta - 1)/(2\vartheta)$. By construction, the set $R_2 \cup (\eta' + R_2)$ also has boundaries with slope $1/2$ which coincide exactly with those of K_τ.

The set R_1 has a boundary with slope $(a + N_2)/N_1 = (N_1 + N_2)/N_1 = 1 + N_2/N_1 \leq (5\vartheta + 1)/(4\vartheta) = (2\vartheta + 2)/(4\vartheta) - (1 - 3\vartheta)/(4\vartheta) \leq (\vartheta + 1)/(2\vartheta)$. The corresponding boundaries of $R_1 \cup (\eta' + R_1)$ then contain the boundaries of K_τ with slope $(\vartheta + 1)/(2\vartheta)$ since $\vartheta < 1/3$. The set R_1 has a boundary with slope $(a - 2N_2)/N_1 = 1 - 2N_2/N_1 \geq 1 - (1+\vartheta)/(2\vartheta) = (\vartheta - 1)/(2\vartheta)$. The corresponding boundaries of $R_1 \cup (\eta' + R_1)$ then contain the boundaries of K_τ with slope $(\vartheta - 1)/(2\vartheta)$. By construction, the set $R_1 \cup (\eta' + R_1)$ also has boundaries with slope $1/2$ which coincide exactly with those of K_τ.

Also by construction, both sets are bounded by the the lines $m = (1/2)k$ and $m = N_2 + (1/2)k$. Since $\eta' = (0, -N_2)^T$, the sets R_2 and $(\eta' + R_1)$ are disjoint. Therefore, there exists $K' \subseteq R_1 \cap R_2$ such that $K_\tau \subseteq (R_2 \cup (\eta' + K'))$.

The argument is similar for the case $1/3 \leq \vartheta < 1/2$ using the fact that satisfying (2.37) implies $a = (N_1 - N_2)$ and the slopes $(a + 2N_2)/N_1$ and $(a - N_2)/N_1$ of the boundaries of R_1. □

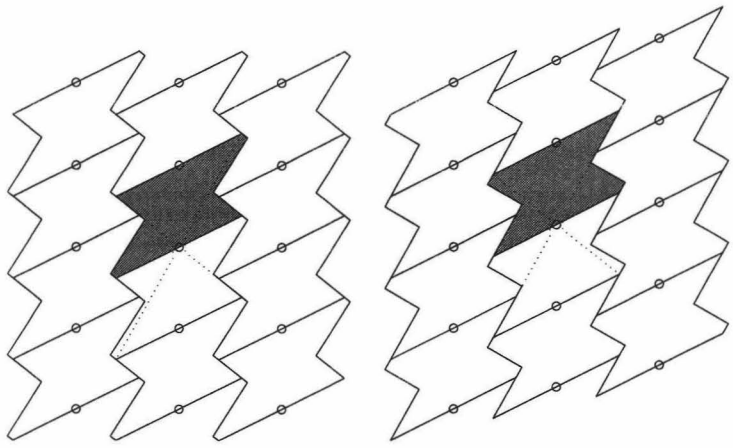

(a) (b)

Figure 2.2: Fundamental domains (a) R_2 of $H_S^\perp$ and (b) R_1 of $H_R^\perp$ and translates for $1/3 < \vartheta \leq 1/2$.

The set $R_2 \cup (\eta' + K')$ is larger then K_τ, containing a large region about the origin. See figure 2.2. According to (1.44), $|\hat{g}|$ is negligible on most of this region, so there is no advantage in recovering $\hat{g}$ here. However, since the lattices $H_S^\perp$ and $H_R^\perp$ have the same density, $m_{\widehat{G}}(R_2) = m_{\widehat{G}}(R_1)$ and there is no reason to construct R_2 and R_1 such that $K' \subseteq R_2 \cap R_1$ is smaller. Also, notice $R_1 \not\subseteq R_2$ so the results of Theorem 17 do not strictly apply. Since $|\hat{g}|$ is negligible outside $K' \cup (\eta' + K')$, we do not expect to observe a significant increase in the aliasing error.

We now compute the values of g on a dense uniform set suitable for use in the (FBP) Algorithm 14. For convenience we compute only the "missing" data in the standard sampling scheme with twice the density in the direction of the second coordinate as the original standard sampling scheme. The missing data lie on a second coset of the standard sampling lattice H_S shifted by an additional $1/(2N_2)$

in the second coordinate. Let $x'_S = (0, (\delta + 1/2)/N_2)^T$ and choose $\delta = 1/4$. Then for all $x \in x'_S + H_S$, $(1 - e^{2\pi i \langle x - x_S, \eta' \rangle}) = 2$ and $\beta = (1 - e^{2\pi i \langle x_R - x_S, \eta' \rangle})^{-1} = 1/2$. An interpolation formula follows from Corollary 15 applied to $g(u, v)$ with x_2, H_2, x_1, H_1 equal to x_S, H_S, x_R, H_R, respectively, and with R_2 and R_1 defined above.

$$Sg(x'_S+z) = S_M g(x'_S+z) + \sum_{y \in H_R} (g(x_R+y) - S_M g(x_R+y)) \phi_{R_1}(x'_S+z-x_R-y) \quad (2.47)$$

with

$$S_M g(x) = \sum_{y \in H_S} g(x_S + y) \phi_{R_2}(x - x_S - y) \quad (2.48)$$

for $z \in H_S$, where $M = x_S + H_S$. The interpolation process can be viewed as first computing an approximation $S_M g$ with bandregion R_2 from samples of g on $(x_S + H_S)$ then adding a correction function with bandregion R_1 computed from samples of $(g - S_M g)$ on $(x_R + H_R)$. If g is bandlimited with bandregion R_2 then $g = S_M g$ and the correction function is identically zero.

It is not practical to compute Sg in (2.47) directly by evaluating the interpolating functions ϕ_{R_2} and ϕ_{R_1}. Instead, we compute $(Sg)\hat{}$ by Lemma 16 and the Poisson summation formula. Then we may recover Sg by the inverse Fourier transform. In this way, we may take advantage of MATLAB's fast Fourier techniques. Though this method proves to be computationally less expensive, it is challenging to implement in two dimensions. The difficulty is in adapting MATLAB's built-in algorithms to produce the correct Fourier transforms which vanish outside the fundamental domains R_2 and R_1 of $H_S^{\perp}$ and $H_R^{\perp}$, respectively, that are not the canonical fundamental domains, i.e. $[0, N_1 - 1] \times [0, N_2 - 1]$, and computed from values on the sets $(x_S + H_S)$ and $(x_R + H_R)$, where H_R is generally not rectangular.

We follow the methods in [8, Section 4] and present an algorithm for evaluating the function $S_M f$ in Lemma 16 with bandregion R on the set $(x_2 + H_2)$ from samples

of f on the set $(x_1 + H_1)$, with $H_1 = [W_1\mathbb{Z}^2]$ and $H_2 = [W_2\mathbb{Z}^2]$ where W_1 and W_2 are 2×2, nonsingular, upper-triangular matrices. This approach is less general than the approach in ([8, Section 4]) in that we do not attempt to characterize the sampling lattices and their generating matrices. Since both W_S and W_R are upper triangular, we devise a method suitable for this case. This algorithm is then used to evaluate $S_M g$ with bandregion R_2 from samples of g on $(x_2 + H_S)$ as well as the correction function with bandregion R_1 from samples of $(g - S_M g)$ on $(x_1 + H_R)$.

Algorithm 20. *Let H_1, H_2 be lattices in $\mathbb{T}^2$ such that $H_1 = [W_1\mathbb{Z}^2]$ and $H_2 = [W_2\mathbb{Z}^2]$ where W_1 and W_2 are 2×2, nonsingular, upper-triangular matrices with diagonals $(1/N_1, 1/N_2)$ and $(1/N_1', 1/N_2')$, respectively with N_1, N_2, N_1', N_2' integers and choose $x_1, x_2 \in \mathbb{T}^2$. Assume the hypotheses of Lemma 16 hold for f with $G = \mathbb{T}^2$ and $H = H_1$ and let $f_{j,l}$ be the values $f([x_1 + W_1(j-1, l-1)^T])$, $j = 1, \ldots, N_1$, $l = 1, \ldots, N_2$, and define*

$$DFT(f_{j,l})_{n_1,l} = \sum_{j=1}^{N_1} f_{j,l} e^{-2\pi i (j-1)(n_1-1)/N_1}, \quad n_1 = 1, \ldots, N_1,\ l = 1, \ldots, N_2$$

and

$$IDFT(g_{n_1,l})_{j,l} = (1/N_1) \sum_{n_1=1}^{N_1} g_{n_1,l} e^{2\pi i (j-1)(n_1-1)/N_1}, \quad j = 1, \ldots, N_1,\ l = 1, \ldots, N_2.$$

Perform the following:

1. *For each $n_1 = 1, \ldots, N_1$, and $n_2 = 1, \ldots, N_2$, let $E_1 = e^{-2\pi i \langle x_1, (n_1-1, n_2-1)\rangle}$ and $E_2 = e^{-2\pi i (n_1-1)(l-1)(W_1)_{1,2}}$ for $l = 1 \ldots N_2$ and compute*

$$(g_1)_{n_1,n_2} = E_1 \times DFT(E_2 \times DFT(f_{j,l})_{n_1,l})_{n_1,n_2}. \tag{2.49}$$

2. *Identify for each (n_1, n_2) the unique element $\eta_{n_1,n_2} \in H_1^{\perp}$ such that $((n_1 - 1, n_2 - 1) + \eta_{n_1,n_2}) \in R$ and compute*

$$(g_2)_{n_1,n_2} = (g_1)_{n_1,n_2} e^{-2\pi i \langle x_1, \eta_{n_1,n_2}\rangle}. \tag{2.50}$$

3. *For each* $n_1' = 1, \ldots, N_1'$, *and* $n_2' = 1, \ldots, N_2'$, *identify all* $(\zeta_{n_1',n_2'})_p \in H_2^{\perp}$ *and all pairs* $(n_1, n_2)_p$ *such that* $(n_1'-1, n_2'-1) = ((n_1-1, n_2-1)_p + \eta_{(n_1,n_2)_p} - (\zeta_{n_1',n_2'})_p)$ *and compute*

$$(g_3)_{n_1'n_2'} = \left(\frac{N_1'N_2'}{N_1N_2}\right) \sum_p (g_2)_{(n_1,n_2)_p} e^{2\pi i \langle x_2, (\zeta_{n_1',n_2'})_p \rangle}. \tag{2.51}$$

4. *For each* $n_1' = 1, \ldots, N_1'$, *and* $n_2' = 1, \ldots, N_2'$, *Let* $E_3 = e^{2\pi i \langle x_2, (n_1'-1, n_2'-1) \rangle}$ *and* $E_4 = e^{2\pi i (n_1'-1)(l'-1)(W_2)_{1,2}}$ *for* $l' = 1 \ldots N_2'$ *and compute for each* $j' = 1, \ldots, N_1'$ *and* $l' = 1, \ldots, N_2'$

$$(g_4)_{j',l'} = IDFT(E_4 \times IDFT(E_3 \times (g_3)_{n_1',n_2'})_{n_1',l'})_{j',l'}. \tag{2.52}$$

Then the function $S_M f$ *evaluated on the set* $([x_2 + W_2(j'-1, l'-1)^T])$ *is given by the values* $(g_4)_{j',l'}$.

The interpolation algorithm above and the reconstruction formula (2.47) lead to an algorithm for exploiting the symmetry property in fan beam CT to accurately compute the values of g on $(x_S' + H_S)$ from samples of g on $(x_S + H_S)$.

Algorithm 21. *Let* $g_{j,l} = Df((j-1)2\pi/N_1, (l-1+\delta)\pi/N_2 - \pi/2)$ *for* $j = 1 \ldots N_1$ *and* $l = 1 \ldots N_2$.

1. *Evaluate* $(S_M g_1)_{j',l'} = S_M g([x_S' + W_S(j'-1, l'-1)^T])$, $j' = 1 \ldots N_1$, $l' = 1 \ldots N_2$ *and* $(S_M g_2)_{\tilde{j},\tilde{l}} = S_M g([x_R + W_R(\tilde{j}-1, \tilde{l}-1)^T])$ *for* $\tilde{j} = 1 \ldots N_1$, $\tilde{l} = 1 \ldots N_2$ *from the samples* $g_{j,l}$.

2. *Let* $\tilde{g}_{\tilde{j},\tilde{l}} = g_{\tilde{j},N_2-\tilde{l}+1}$, $\tilde{j} = 1 \ldots N_1$, $\tilde{l} = 1 \ldots N_2$ *and evaluate the correction function* $h_{j',l'} = h([x_S' + W_S(j'-1, l'-1)^T])$, $j' = 1 \ldots N_1$, $l' = 1 \ldots N_2$ *from samples* $(\tilde{g}_{\tilde{j},\tilde{l}} - (S_M g_2)_{\tilde{j}\tilde{l}})$, $\tilde{j} = 1 \ldots N_1$, $\tilde{l} = 1 \ldots N_2$.

Then the values of g on the standard sampling scheme with twice the density in the second coordinate as the original is given by $\bar{g}_{(2j-1),(2l-1)} = g_{j,l}$, $j = 1 \dots N_1$, $l = 1 \dots N_2$ *and* $\bar{g}_{(2j'),(2l')} = ((Sg_1)_{j',l'} + h_{j',l'})$, $j' = 1 \dots N_1$, $l' = 1 \dots N_2$.

2.3 Numerical Results

We present numerical experiments to illustrate the performance of Algorithm 21 with both simulated and real CT data. The images are reconstructed using the FBP Algorithm 14 at the highest reasonable cut-off frequency b. All algorithms are implemented in Matlab version 6.

The simulated CT data is computed using a common mathematical phantom attributed to Shepp and Logan [37] and modified by Rowland [34]. It consists of a superposition of ellipses of various sizes, shapes, and densities and simulates CT data of a head section. We assume an object radius of $\rho = 1$ and choose a scanning radius of $r = 2.868$. We choose $\tau = 0.99$ and note $1/3 < \vartheta < 1/2$. We choose $N_1 = 392$ equispaced views per rotation and $N_2 = 360$ rays per fan, satisfying condition (2.37). A quarter-detector offset, $\delta = 1/4$, is employed. The images are reconstructed on a 512×512 grid and displayed in gray scale which sets values below 1.0 to black and values above 1.05 to white.

In the first experiment, we compare the reconstruction from the interpolated data set with those from the standard data set with the same data and a standard reconstruction from twice as much measured data. Figure 2.3(a) shows the reconstruction with cut-off frequency $b = 360$ from the standard data set measured with $N_2 = 360$. Figure 2.3(b) shows the reconstruction with cut-off frequency $b = 720$ from the interpolated data set. The boundaries of the ellipses are sharper and fine

Table 2.1: Shepp-Logan head phantom.

ellipse	density	center	e1	e2	rotation
1.	2.0	(0,0)	0.69	0.92	0
2.	-0.98	(0,-0.184)	0.6624	0.874	0
3.	-0.02	(0.22,0)	0.11	0.31	-18°
4.	-0.02	(-0.22,0)	0.16	0.41	18°
5.	0.01	(0,0.35)	0.21	0.25	0
6.	0.01	(0,0.1)	0.046	0.046	0
7.	0.01	(0,-0.1)	0.046	0.046	0
8.	0.01	(-0.08,-0.605)	0.046	0.023	0
9.	0.01	(0,-0.605)	0.023	0.023	0
10.	0.01	(0.06,-0.605)	0.023	0.046	0
11.	0.03	(0.5538,0.3858)	0.0333	0.206	-18°

details, such as the spaces between the small ellipses, appear better resolved. Figure 2.3(c) shows the reconstruction with cut-off frequency $b = 720$ from a standard data set measured with $N_2 = 720$ rays per fan. The image in figure 2.3 (b) is comparable in quality and uses only half the measured data. Figure 2.3(d) shows cross sections of the reconstructions from the standard and interpolated data through the centers of the small ellipses. The reconstruction from the interpolated data more accurately recovers the true value of the density over the width of the objects.

In the second experiment, we model some physical properties of real CT scanners. A finite detector width is modeled by averaging the integrals over 5 rays

equispaced over the width of the detector. The value is considered to be sampled at the center of the detector. We model signal noise by adding to each measurement a normally distributed pseudo-random number with mean zero and standard deviation 1/3000. This is intended to simulate a noise level of at most 0.1% of the maximum measured value. We repeat the first experiment with the noisy data. Figure 2.4(a) shows the reconstruction with cut-off frequency $b = 360$ from the standard data set measured with $N_2 = 360$. Figure 2.4(b) shows the reconstruction with cut-off frequency $b = 720$ from the interpolated data set. Again, the boundaries of the ellipses are sharper but not as sharp as in figure 2.4(b) due to the finite detector width. Reconstruction artifacts are diminished but the image in (b) is more "grainy", suggesting noise amplification predicted by Theorem 17. Figure 2.4(c) shows the reconstruction with cut-off frequency $b = 720$ from a standard data set measured with $N_2 = 720$ rays per fan. This image is sharper than the image in figure 2.4(b) due to averaging rays over smaller detectors. It also less grainy. Figure 2.4(d) shows a crossection of the reconstructions from the standard and interpolated data through the centers of the small ellipses. Again, the reconstruction from the interpolated data more accurately recovers the true value of the density over the width of the objects but fails to fully recover the small gap between the ellipses.

The final experiment uses real data acquired by a Siemens CT scanner. The data set consists of $N_1 = 720$ views per rotation with $2q = 512$ beams per view crossing the unit disc. The scanning radius is $r = 2.868$ and the object is essentially contained in a disc of radius $\rho = .28$ centered at the origin. By trial it is determined that a detector offset of $\delta = +1/4$ gives the best reconstruction from the standard data, and it is therefore assumed to have been scanned with positive quarter-detector offset. Beyond this, not much is known about the data. In particular, we do not

know to what extent the data has been pre-filtered or otherwise manipulated, and we do not know the noise level in the data.

We approximate the scanning parameter N_2 by $N_2 \approx q\pi/\arcsin(1/r)$ for $q = 256$ and $r = 2.868$ and obtain $N = 2258$. To satisfy condition (2.37) with $\vartheta < 1/3$ requires a minimum of $N_1 = 804$ views per rotation. It is not possible to reduce the object size ρ any further without suffering severe artifacts. Instead, assume Ω is such that $r\Omega/2 < N_2$ and translates of the set $K_\tau(r, \rho, \Omega)$ by elements of $H_S^\perp$, nonzero in the first component, do not intersect and reduce the cut-off frequency b of the reconstruction from the interpolated data. We interpolate the missing values in a data set with $N_1 = 720$ views per rotation and $2q = 1024$ rays per view crossing the unit disc. The images are reconstructed on a 512×512 grid and displayed in gray scale with values below 1×10^4 set to black and values above 1.6×10^4 set to white. Figure 2.5(a) shows the reconstruction with cut-off frequency $b = 2258$ from the standard data set. Figure 2.5(b) shows the reconstruction with cut-off frequency $b = (1.75)2258$ from the interpolated data set. Again, the interpolated data appears to produce a sharper image but suffers from possible noise amplification. Over all, there is at least a qualitative improvement over the standard reconstruction. Having little information about the actual data, the results are encouraging. Figures 2.5(c) and 2.5(d) show reconstructions of the small hole in the light rectangle from standard and interpolated data sets, respectively. The images are reconstructed on a 128×128 grid with the same gray scale as before. The reconstruction from interpolated data shows a darker, more defined object but the graininess distorts the shape which is assumed to be a circle. Figure 2.5(e) shows crossections through the center of the small hole in (c) and (d). The edges of the hole in the reconstruction from interpolated data are clearly steeper then those in the standard reconstruction and

the the minimum value at the center of the hole, assumed to be the density of the medium $\approx 1.31 \times 10^4$, is better achieved. This has proved to be the case with all the details observed in the reconstruction. However, the ill effects possibly due to amplified noise in the interpolated data make it difficult to resolve the true value of the density in the small, low-contrast holes in the dark rectangle.

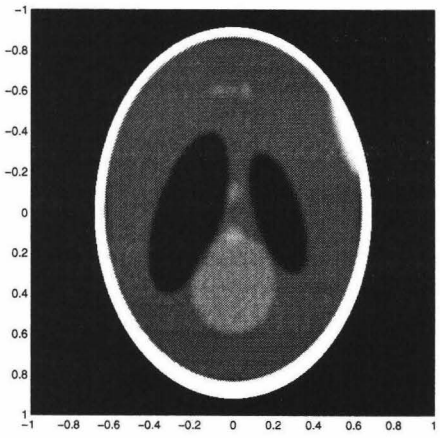

(a) Standard: $N_2 = 360$.

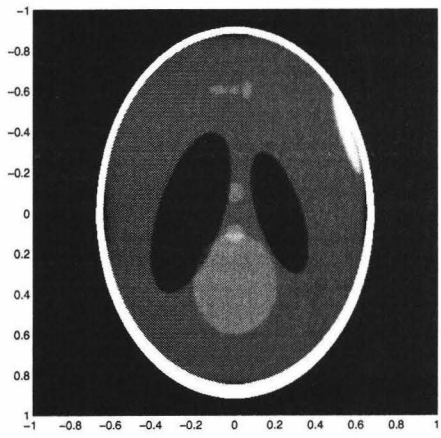

(b) Interpolated: $N_2 = 360$.

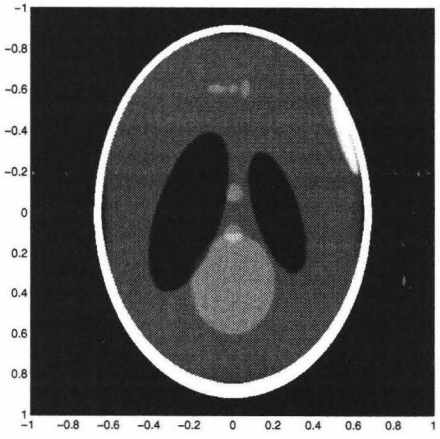

(c) Standard: $N_2 = 720$.

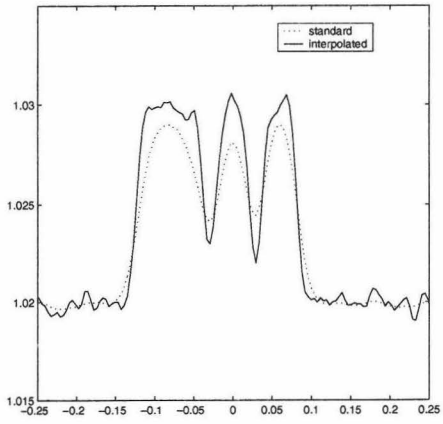

(d) Cossection of small ellipses.

Figure 2.3: Reconstruction of the Shepp-Logan phantom.

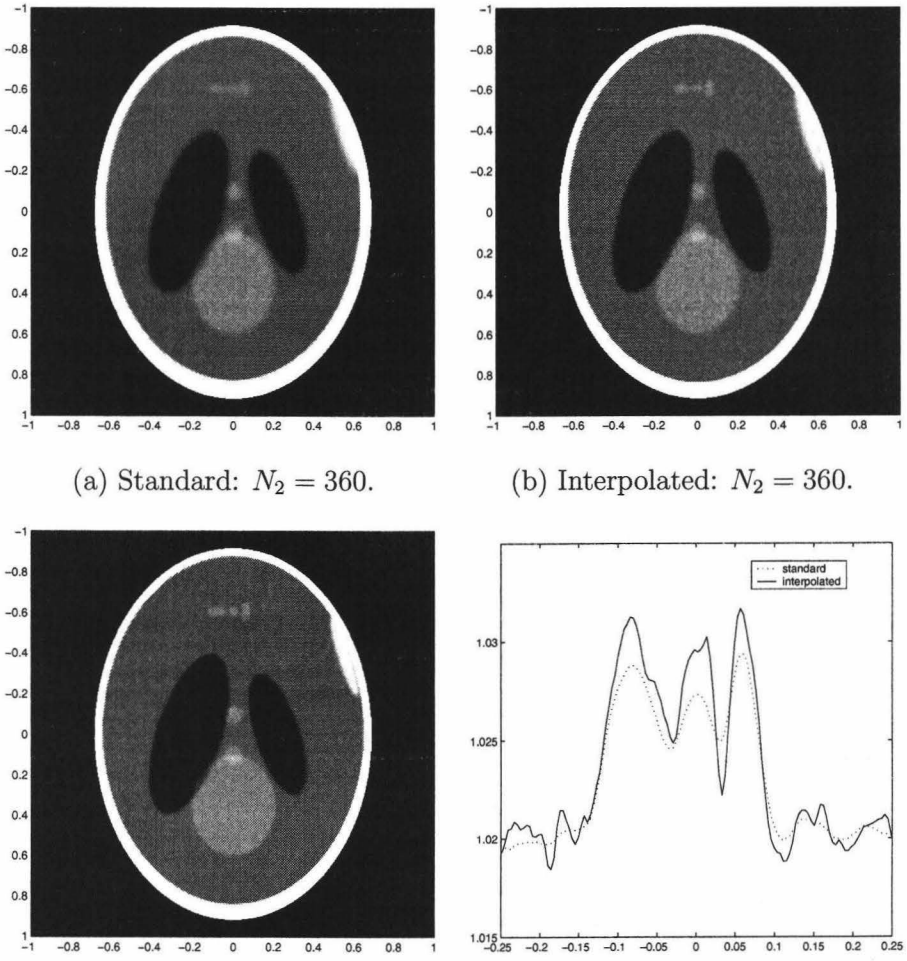

(a) Standard: $N_2 = 360$.

(b) Interpolated: $N_2 = 360$.

(c) Standard: $N_2 = 720$.

(d) Crossection of small ellipses.

Figure 2.4: Reconstruction of the Shepp-Logan phantom with finite detector width and noise.

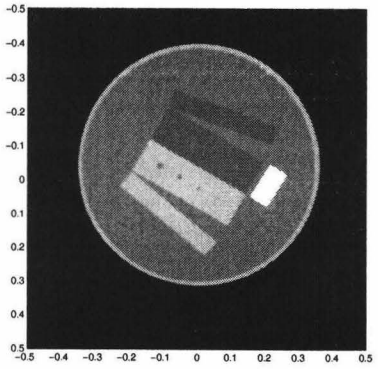

(a) Standard

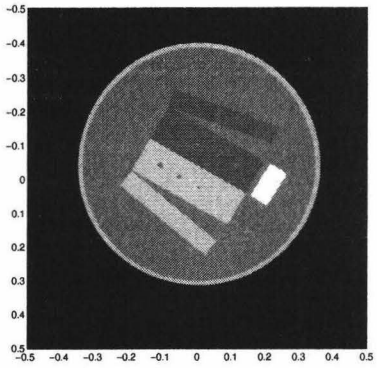

(b) Interpolated

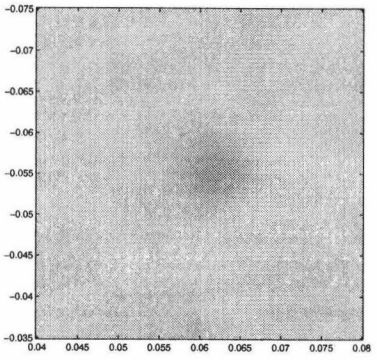

(c) Standard

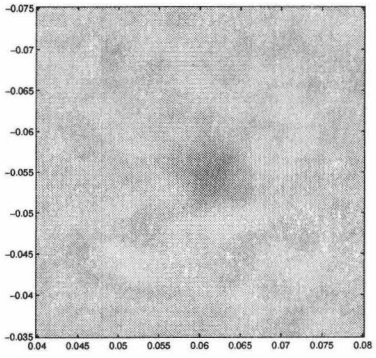

(d) Interpolated

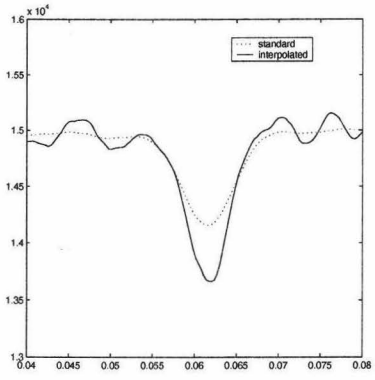

(e) Crossection of small hole.

Figure 2.5: Reconstruction of Siemens phantom.

3 PREFERRED HELICAL PITCH IN MULTISLICE HELICAL CT

The x-ray transform, Pf, (1.33) of a function f on $\mathbb{R}^3$ is a function on $S^2 \times \mathbb{R}^2$. We then expect the problem of reconstructing f on $\mathbb{R}^3$ from its set of line integrals to be overdetermined. It is reasonable to expect that we may reconstruct f from measurements of Pf on a suitably chosen subset of $S^2 \times \mathbb{R}^2$. For practical reasons we consider a geometry in which rays emanate from source points on a path in $\mathbb{R}^3$.

Assume $f \in C_0^\infty(\mathbb{R}^3)$ and define a coordinate system in $\mathbb{R}^3$ such that f is contained in the unit cylinder about the z-axis. Consider a scanning geometry in which two-dimensional fan beam projections, or slices, are measured in planes orthogonal to the z-axis. We extend the divergent beam transform (1.39) to three dimensions by

$$Df(\beta, \alpha, z) = \int_0^\infty f(a + t\theta)\, dt \tag{3.1}$$

where

$$a = (r\cos\beta, r\sin\beta, z)^T, \quad \text{and} \quad \theta = -(\cos(\beta+\alpha), \sin(\beta+\alpha), 0)^T, \tag{3.2}$$

with $r > 1$, $0 \le \beta < 2\pi$, $-\pi/2 \le \alpha < \pi/2$, and $z \in \mathbb{R}$.

In practice, x-ray projection data are measured by a detector array composed of cells of finite width. The data measured by an individual cell is the net effect of all rays incident to the cell. Let $\Delta\alpha$ be the width of a detector cell within the slice and let D be the slice thickness measured in the direction of the z-axis. Since rays emanate from a point source, all rays within a slice are not orthogonal to the z-axis, and the actual thickness of the slice is not constant. Since it is assumed that the scanning radius $r \gg D$, it is reasonable to neglect the small cone angle. In practice,

the slice thickness is measured at the point where the slice intersects the z-axis. We model the data function $g(\beta, \alpha, z)$ by the convolutions

$$g(\beta, \alpha, z) = \int_{-D/2}^{D/2} a_1(z-t) \int_{-\Delta\alpha/2}^{\Delta\alpha/2} a_2(\alpha-\omega) Df(\beta, \omega, t)\, d\omega\, dt \tag{3.3}$$

where the functions a_1 and a_2 describe the response of the detector to the incident rays in the z and α directions, respectively. (See e.g. [29].) We assume uniform response functions, that is

$$a_1(z) = \begin{cases} 1/D & \text{for} \quad -D/2 < z < D/2, \\ 0 & \text{otherwise,} \end{cases} \tag{3.4}$$

and

$$a_2(\alpha) = \begin{cases} (1/\Delta\alpha) & \text{for} \quad -\Delta\alpha/2 < \alpha < \Delta\alpha/2, \\ 0 & \text{otherwise.} \end{cases} \tag{3.5}$$

The two-dimensional fan beam version of the FBP Algorithm 14 may be used to reconstruct f on the plane $z = z'$ from measurements of $g(\beta, \alpha, z')$. A three-dimensional reconstruction of f is obtained, slice-by-slice, by repeating the two-dimensional reconstruction process on a sequence of equispaced parallel planes.

3.1 Sampling and Reconstruction

In the standard sampling scheme the object is positioned so that the fan of x-rays illuminates a portion of the object, then the source and detector array make a complete revolution about the object capturing M equispaced views. The object is then translated a distance Δz in the direction of the z-axis, orthogonal to the projection plane, and the process is repeated. It is convenient to use a coordinate

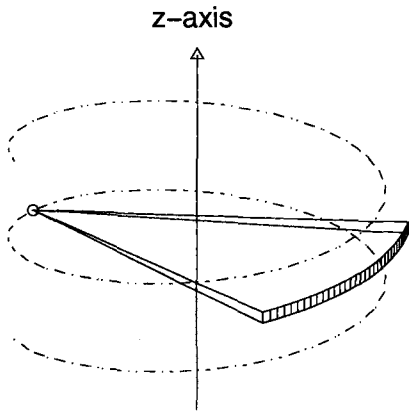

Figure 3.1: Helical CT geometry.

system in which the object is at rest. Then the standard sampling scheme measures the values $g(\beta_\mu, \alpha_\nu, z_k)$ where

$$\beta_\mu = \frac{2\pi\mu}{M}, \quad \mu = 0, \ldots, M-1, \quad \alpha_\nu = \frac{\pi(\nu+\delta)}{N}, \quad \nu = -q, \ldots, q-1, \quad \text{and}$$
$$z_k = k\Delta z, \quad k = 0, \ldots, \overline{k}, \tag{3.6}$$

with $M, N, \overline{k}$ integers, $\Delta z \in \mathbb{R}$, $0 \leq \delta < 1$, and $q \in \mathbb{Z}$ such that $N \arcsin(1/r)/\pi \leq q \leq N/2$. This is referred to as the "step-and-shoot" sampling method.

In practice, it is desirable to translate the object continuously while the source and detector array are rotating about the z-axis. See [16] and [3]. In a coordinate system in which the object is at rest, the source points lie on a helical path about the z-axis. See figure 3.1. We call the z-axis the longitudinal axis of the helix. In

this helical sampling scheme we measure $g(\beta_\mu, \alpha_\nu, z_{\mu,k})$ where

$$\beta_\mu = \frac{2\pi\mu}{M}, \quad \mu = 0, \ldots, M-1, \quad \alpha_\nu = \frac{\pi(\nu+\delta)}{N}, \quad \nu = -q, \ldots, q-1, \quad \text{and}$$
$$z_{\mu,k} = \Delta z \left(k + \frac{\mu}{M}\right), \quad k = 0, \ldots, \overline{k}, \tag{3.7}$$

with $M, N, \overline{k}$ integers, $\Delta z \in \mathbb{R}$, $0 \leq \delta < 1$, and $q \in \mathbb{Z}$ such that $N \arcsin(1/r)/\pi \leq q \leq N/2$. Here Δz is the longitudinal distance traveled by the source and detector array with respect to a stationary object during one complete revolution. In this scheme we measure only one view per longitudinal position. To reconstruct f on the plane $z = z'$ using the two-dimensional FBP algorithm, it is necessary to interpolate the values of g on a complete set of M fan beam projections, each in the plane $z = z'$. We consider only those helical sampling schemes that permit one-dimensional interpolation between corresponding rays in the longitudinal direction. It is then convenient to write $g_{\mu,\nu}(z) = g(\beta_\mu, \alpha_\nu, z)$. For an analysis of more general three-dimensional sampling schemes, see [5].

An important parameter in helical CT is the helical pitch. It is defined as the ratio of the longitudinal distance traveled by the source and detector array per rotation to the slice thickness [36]. We can then express the distance Δz traveled per rotation by the source and detector array in terms of the helical pitch P and slice thickness D by $\Delta z = PD$. For fixed β_μ and α_ν we measure the data function $g_{\mu,\nu}(z)$ once per rotation. Therefore, we sample $g_{\mu,\nu}(z)$ on a coset $(x_0 + H)$ of the lattice $H = (PD)\mathbb{Z}$ shifted by $x_0 = PD(\mu/M)$.

By the convolution theorem, the one-dimensional Fourier transform of the data function $g_{\mu,\nu}(z)$ in (3.3) may be written

$$\hat{g}_{\mu,\nu}(\xi) = \hat{a}_1(\xi)(a_2 * Df)\hat{}\,(\beta_\mu, \alpha_\nu, \xi), \quad \xi \in \mathbb{R}, \tag{3.8}$$

where the Fourier transform on the right hand side is with respect to the third variable z. The averaging of integrals over the thickness of the slice effectively bandlimits the data function. It is reasonable to assume as the bandwidth of $g_{\mu,\nu}(z)$ the first zero of $\widehat{a}_1$ [15, p. 187]. The Fourier transform of (3.4) yields $\hat{a}_1(\xi) = \sin(\pi D\xi))/(\pi D\xi)$ for $\xi \neq 0$ and $\hat{a}_1(0) = 1$. It follows that the essential bandwidth of $g_{\mu,\nu}$ is $b = 1/D$. That is, we assume for all $\mu = 0, \ldots, M-1$ and $\nu = -q, \ldots, q-1$ that $|\hat{g}_{\mu,\nu}(\xi)|$ is small for a.e. ξ outside the interval

$$K = [-b, b) \quad \text{with} \quad b = 1/D. \tag{3.9}$$

The interval $R = [-1/(2PD), 1/(2PD))$ is a fundamental domain of the annihilator $H^\perp = (1/(PD))\mathbb{Z}$ of the sampling lattice $H = (PD)\mathbb{Z}$. According to the classical sampling theorem, Theorem 6, given $z' \in \mathbb{R}$ we can accurately reconstruct each $g_{\mu,\nu}(z')$ for $\mu = 0, \ldots, M-1$ and $\nu = -q, \ldots, q-1$ from samples of each $g_{\mu,\nu}(z)$ on a coset of H if $K = [-b, b) \subseteq R$. This implies a helical pitch of $P \leq 1/2$. This means that the source and detector must make a least two complete revolutions while the object is translated the distance of only a single slice thickness.

For a choice of helical pitch $P > 1/2$, translates of the set K by elements $H^\perp$ intersect, and sampling $g_{\mu,\nu}(z)$ on $H = (PD)\mathbb{Z}$ leads to undersampling. For each $\xi \in K$ let $\overline{M}_\xi = H^\perp \cap (K - \xi)$. Since $H^\perp$ is discrete and the set $(K - K)$ is bounded, the sets $\overline{M}_\xi$ are finite and assume only finitely many values as ξ runs through the set K. Let $\overline{m}$ be the smallest integer larger than or equal to $2P$, that is $\overline{m} - 1 < 2P \leq \overline{m}$, and let $L = 2\overline{m} - 1$. Then the sets $\overline{M}_\xi$ assume L distinct values $\overline{M}^{(1)}, \ldots, \overline{M}^{(L)}$ as ξ runs through all of K. The relation $\xi \equiv \xi' \leftrightarrow \overline{M}_\xi = \overline{M}_{\xi'}$ is an equivalence relation induced by the subgroup H. The intersections of the set K with its translates by elements of $H^\perp$ then partition K into a union of disjoint subsets

$K_l, \quad l = 1, \ldots, L$, where $K_l = \{\xi \in K : \overline{M}_\xi = \overline{M}^{(l)}\}$. The subsets K_l, $l = 1, \ldots, L$ can be expressed explicitly by

$$K_l = \begin{cases} \left[-b + \frac{(l-1)}{PD}, b - \frac{(\overline{m}-l)}{PD}\right), & l = 1, \ldots, \overline{m}, \\ \left[b - \frac{(2\overline{m}-l)}{PD}, -b + \frac{(l-\overline{m})}{PD}\right), & l = \overline{m}+1, \ldots, 2\overline{m}-1. \end{cases} \tag{3.10}$$

For integral and half-integral values of helical pitch, the sets K_l for $l = \overline{m} + 1, \ldots, 2\overline{m} - 1$ have zero measure in $\mathbb{R}$ and so do not contribute to the aliasing error. In these cases we may assume only $\overline{m}$ subsets of K.

Let $m_l = |\overline{M}^{(l)}|$, $l = 1, \ldots, L$. Then, with the subsets K_l, $l = 1, \ldots, L$ expressed as above, we have $m_l = \overline{m}$ for $l = 1, \ldots, \overline{m}$ and $m_l = \overline{m} - 1$ for $l = \overline{m} + 1, \ldots, 2\overline{m} - 1$. We may express the sets $\overline{M}^{(l)}$, $l = 1, \ldots, L$ explicitly by

$$\overline{M}^{(l)} = \left\{\eta_j^{(l)}\right\}_{j=1}^{m_l} = \begin{cases} \left\{\frac{(j-l)}{PD}\right\}_{j=1}^{\overline{m}}, & l = 1, \ldots, \overline{m}, \\ \left\{\frac{(j+\overline{m}-l)}{PD}\right\}_{j=1}^{\overline{m}-1}, & l = \overline{m}+1, \ldots, 2\overline{m}-1. \end{cases} \tag{3.11}$$

For example, if we let $P = 4/3$ then $\overline{m} = 3$ and the sets K_l, $l = 1, \ldots, 5$ are

$$\begin{aligned} K_1 &= [-1/D, -1/2D), \quad K_2 = [-1/4D, 1/4D), \\ K_3 &= [1/2D, 1/D), \\ K_4 &= [-1/2D, -1/4D), \quad K_5 = [1/4D, 1/2D). \end{aligned}$$

The sets $\overline{M}^{(l)}$, $l = 1, \ldots, 5$ are

$$\begin{aligned} \overline{M}^{(1)} &= (1/(PD))\{0, 1, 2\}, \quad \overline{M}^{(2)} = (1/(PD))\{-1, 0, 1\}, \\ \overline{M}^{(3)} &= (1/(PD))\{-2, -1, 0\}, \\ \overline{M}^{(4)} &= (1/(PD))\{0, 1\}, \quad \overline{M}^{(5)} = (1/(PD))\{-1, 0\}. \end{aligned}$$

Additional samples of $g_{\mu,\nu}(z)$ are necessary to overcome the undersampling on H and accurately recover $\hat{g}_{\mu,\nu}(\xi)$ for $\xi \in K$.

We extend the symmetry property (2.1) of the two-dimensional divergent beam transform to three dimensions by

$$Df(\beta, \alpha, z) = Df(\beta + 2\alpha + \pi, -\alpha, z). \tag{3.12}$$

It follows from (3.3) that $g(\beta, \alpha, z) \approx g(\beta + 2\alpha + \pi, -\alpha, z)$, where the approximate equality is due to the fact that the rays emanate from source points, and the rays involved in the convolution over the small fan angle $\Delta\alpha = \pi/N$ for source angle β do not diverge from a point corresponding to angle $(\beta + 2\alpha + \pi)$. Nevertheless, if the scanning radius r is sufficiently large, we may use the symmetry property to assume the values of the data function $g(\beta, \alpha, z)$ on an additional set of points in the sampling domain.

If the sampling parameters M and N are chosen such that for every $\mu = 0, \ldots, M-1$ and $\nu = 0, \ldots, N-1$ the source angle $(\beta_\mu + 2\alpha_\nu + \pi) = \beta_{\mu'}$ and the fan angle $-\alpha_\nu = \alpha_{\nu'}$ for some integers $0 \leq \mu' \leq M-1$ and $0 \leq \nu' \leq N-1$, then the set of directly sampled rays and the set of reflected rays obtained by the symmetry property are redundant with respect to the first two coordinates. That is, the direct sampling scheme and the reflected sampling scheme involve the same set of source and fan angles (β_μ, α_ν) for $\mu = 0, \ldots, M-1$ and $\nu = 0, \ldots, N-1$. This redundancy will occur if and only if one of the following holds:

$$\begin{array}{llllll} (i) & \delta = 0, & M \text{ even}, & \text{and} & \sigma = M/N \text{ integer}, & \\ (ii) & \delta = 1/2, & M \text{ even}, & \text{and} & \sigma = M/N \text{ even}, & \text{or} \\ (iii) & \delta = 1/2, & M \text{ odd}, & \text{and} & \sigma = M/N \text{ odd}. & \end{array} \tag{3.13}$$

(cf. [27].) If the parameters r and τ are such that $\vartheta = \tau^{-1}(1/r) = 1/3$, then we may choose $M = N$ and satisfy both the above condition with $\delta = 0$ as well as the two dimensional sampling conditions in (1.49) with $N = r\Omega$. Unless otherwise stated,

we will assume condition (i) in (3.13) holds for the reminder of the chapter.

The direct rays and the reflected rays may be redundant with respect to the first two coordinates, but with source points on a helical path, the reflected rays are shifted with respect to the corresponding direct rays in the direction of the z-axis by a distance of nearly $PD/2$. In particular, if for fixed (β_μ, α_ν) we sample the data function $g_{\mu,\nu}(z)$ on a coset $(x_0 + H)$ of $H = (PD)\mathbb{Z}$ with $x_0 = PD(\mu/M)$ then by symmetry and satisfying (3.13) we may assume the values of $g_{\mu,\nu}(z)$ on a second coset of H shifted by $PD(\mu/M + \nu/N + 1/2) = PD(\mu + \sigma\nu + M/2)/M$ with respect to $(x_0 + H)$.

Multislice CT scanners use a two dimensional detector array consisting of a limited number of rows of cells. This allows for the simultaneous measurement of multiple adjacent slices per view. Again, since the rays emanate from a point source, slices are not parallel and normal to the z-axis. If the scanning radius is sufficiently large, and the number of slices is relatively few, then we may neglect the cone angle and assume the slices are parallel [36]. Each slice is shifted with respect to its neighbor by a distance D in the direction of the z-axis. In addition, the symmetry property (3.12) may be used to assume values of additional samples for each slice. Therefore, if the redundancy condition (3.13) is satisfied, a multislice helical CT scanner with S slices measures for each fixed (β_μ, α_ν) for $\mu = 0, \ldots, M-1$ and $\nu = -q, \ldots, q-1$, the function $g_{\mu,\nu}(z)$ on the set $\cup_{n=0}^{2S-1}(x_n + H)$ with

$$\begin{aligned} x_n &= \left(nD + PD\left(\frac{\mu}{M}\right)\right), \quad \text{and} \\ x_{n+S} &= \left(nD + PD\left(\frac{\mu'}{M}\right)\right), \quad n = 0, \ldots, S-1, \end{aligned} \tag{3.14}$$

where $\mu' = (\mu + \sigma\nu + M/2)$ with $\sigma = M/N$ integer. This sampling set is generally nonuniform but periodic. That is, the sample points occur in a repeating

pattern. The period of the sampling pattern depends on the helical pitch P and the distribution of points within one cycle varies with fan angle α_ν. Thus, interpolating the values of $g_{\mu,\nu}(z)$ in the direction of the z-axis for each $\mu = 0, \ldots, M-1$ and $\nu = -q, \ldots, q-1$ amounts to solving a collection of one-dimensional nonuniform but periodic sampling problems. A one-dimensional version of Theorem 7 may be applied to compute a sampled versions of $g_{\mu,\nu}(z') = g(\beta_\mu, \alpha_\nu, z')$ for each $\mu = 0, \ldots, M-1$, $\nu = -q, \ldots, q-1$ from the samples of $g_{\mu,\nu}(z)$ on $\cup_{n=0}^{2S-1}(x_n + H)$. Then the two-dimensional FBP algorithm is used to reconstruct f on the plane $z = z'$.

Suppose M, N are chosen such that the redundancy condition (i) in (3.13) is satisfied. Using the shifts $\{x_n\}$, $n = 0, \ldots, 2S-1$, given in (3.14) and the sets $\overline{M}^{(l)}$, $l = 1, \ldots, \overline{m}$, given in (3.11), the systems in (1.18) become for $l = 1, \ldots, \overline{m}$,

$$\begin{aligned}
&\sum_{n=0}^{S-1} \left(\beta_n^{(l)} + \beta_{n+S}^{(l)} \right) = 1, \\
&\sum_{n=0}^{S-1} \left(\beta_n^{(l)} e^{2\pi i (j-l)(n/P + \mu/M)} + \beta_{n+S}^{(l)} e^{2\pi i (j-l)(n/P + \mu'/M)} \right) = 0, \quad j = 1, \ldots, \overline{m},\ j \neq l,
\end{aligned} \tag{3.15}$$

where $\mu' = (\mu + \sigma\nu + M/2)$ with $\sigma = M/N$ integer. We see from (3.11) that $\overline{M}^{(\overline{m}+l)} \subset \overline{M}^{(l)}$ for $l = 1, \ldots, \overline{m}-1$. In fact, we have that $\overline{M}^{(\overline{m}+l)} = \overline{M}^{(l)} \cap \overline{M}^{(l+1)}$ for $l = 1, \ldots, \overline{m}-1$. Therefore, the systems (1.18) using shifts (3.14) and sets (3.11) for $l = \overline{m}+1, \ldots, 2\overline{m}-1$, are identical to those for $l = 1, \ldots, \overline{m}-1$, with the exception of one less row. Solutions of the systems (3.15) for $l = 1, \ldots, \overline{m}-1$ will then also be solutions of the corresponding systems for $l = \overline{m}+1, \ldots, 2\overline{m}-1$. Thus, it suffices to consider only solutions of (3.15) for $l = 1, \ldots, \overline{m}$ and assume the solutions for $l = \overline{m}+1, \ldots, 2\overline{m}-1$.

If for each $\mu = 0, \ldots, M-1$ and $\nu = 0, \ldots, N-1$, the systems (3.15) admit solutions $\beta_n^{(l)}$, $n = 0, \ldots, 2S-1$ for each $l = 1, \ldots, 2\overline{m}-1$ then, by Theorem 7, we compute the sampled version $Sg_{\mu,\nu}(z)$ of $g_{\mu,\nu}(z)$ by

$$Sg_{\mu,\nu}(z) = \sum_{n=0}^{2S-1} \sum_{y \in H} g_{\mu,\nu}(x_n + y) k_n(z - x_n - y), \tag{3.16}$$

with

$$k_n(z) = (PD) \sum_{l=1}^{2\overline{m}-1} \beta_n^{(l)} \int_{K_l} e^{2\pi i \langle z, \xi \rangle} \, d\xi,$$

where K_l, $l = 1, \ldots, 2\overline{m}-1$ given in (3.10).

Notice that the systems in (3.15) consist of $\overline{m}$ rows and $2S$ columns. Recall that $\overline{m} = \max_l |\overline{M}^{(l)}|$ is such that $\overline{m} - 1 < 2P \leq \overline{m}$. This means that, theoretically, we may choose helical pitch $P \leq S$ and obtain solutions $\beta_n^{(l)}$, $l = 1, \ldots, 2\overline{m}-1$ to compute $Sg_{\mu,\nu}$ for each $\mu = 0, \ldots, M-1$ and $\nu = 0, \ldots, N-1$ by (3.16). That is, we may now, in principle, translate the object up to S times the slice thickness in a single revolution of the scanner. This is the advantage that multislice helical scanning offers over the step-and-shoot method. However, all periodic sets are not equal. In particular, the distribution of sample points in the scheme $\cup_{n=0}^{2S-1}(x_n + H)$ with x_n given by (3.14) depends on the fan angle α_ν. Given a choice of helical pitch P there may exist α_ν such that the systems (3.15) do not admit solutions, or admit undesirable solutions. An S-slice helical scanner may have a so-called preferred helical pitch for which the systems (3.15) admit desirable solutions for all α_ν. We now describe what is meant by "desirable" solutions and discuss preferred helical pitch further.

3.2 Preferred Helical Pitch

To accurately reconstruct the function f slice-by-slice, we must stably interpolate the values of $g_{\mu,\nu}(z')$ for each β_μ, α_ν in the 2D fan beam projections in the plane $z = z'$. The estimate for the aliasing error given in Theorem 8 gives a measure γ of the stability of the interpolation process. If the shifts, $\{x_n\}$ in (3.14) are such that the sampling points are bunched closely together, the systems (3.15) will tend to admit solutions for which $\gamma = \overline{m}(\max_l \sum_n |\beta_n^{(l)}|)$ is large. Then values of $\hat{g}_{\mu,\nu}(\xi)$ for ξ outside of $K = [-b, b)$ are amplified in the reconstruction, and the interpolation process based on the reconstruction formula (3.16) is unreliable. We consider the slice thickness D to be a fixed parameter. The choice of helical pitch P and the particular fan angle α_ν determine the distribution of points in the sampling set according to (3.14). The challenge is to choose a helical pitch P such that the systems (3.15) admit solutions for which the corresponding value of γ is uniformly low for all α_ν. We call the largest of these the preferred helical pitch of the system.

In S-slice CT we always sample $2S$ cosets of H regardless of the value of helical pitch. For all but the largest allowed values of pitch the $\overline{m} \times 2S$ systems (3.15) are generally underdetermined. We may then choose a suitable solution. Selecting a low helical pitch is advantageous in that it permits greater flexibility in the solutions of the systems in (3.15). For some choice of pitch P and at some fan angle α_ν, it may be that at least two cosets $(x_n + H)$ and $(x_{n'} + H)$ of H are identical and the samples on $(x_n + H)$ and $(x_{n'} + H)$ are redundant. Then the resulting system (3.15) contains duplicate columns. Since the systems are generally underdetermined, however, they may still admit solutions for which the amplification factor γ is low. This may be achieved by either letting $\beta_{n'}^{(l)} = 0$ and disregarding the samples on $(x_{n'} + H)$, or by

letting $\beta_{n'}^{(l)} = \beta_n^{(l)}$ and effectively averaging the two sets of samples. If, however, we select a large pitch and too many of the sets of data are redundant, then the systems (3.15) may become overdetermined and not admit solutions. Near these situations, when many cosets of H nearly coincide, the systems tend to admit solutions with large positive and negative values. The corresponding value of γ can be quite large, and the helical pitch is not preferred.

We consider some circumstances under which the cosets $(x_n + H)$ of H for $N = 0, \ldots, 2S - 1$ may not be well distributed in $\mathbb{R}$. First, for integer values of pitch $P < S$ we see from (3.14) that as sets $(x_n + H) = (x_{n+P} + H)$ and $(x_{n+S} + H) = (x_{n+P+S} + H)$ for $n = 0, \ldots, S - P - 1$ and for each (μ, ν). That is, all of the rays measured by slice n, after one rotation of the helix will coincide with the rays measured by slice $n + P$ on the previous rotation and when the rays measured by slices n and $n + P$ coincide, so do the corresponding reflected rays. The resulting systems (3.15) have, at best, $2P$ independent columns. Since P is an integer, $\overline{m} = 2P$ and the systems (3.15) may still be consistent, provided no other coincidences occur.

Now suppose, at helical pitch P, there exist shifts x_{n_1}, x_{n_2} such that as sets $(x_{n_2} + H) = (x_{n_1+S} + H)$ for some α_ν. Then $(n_2 D + PD(\mu/M)) = (n_1 D + PD(\mu + \sigma\nu + M/2)/M)$, and for each $l = 1, \ldots, 2\overline{m} - 1$

$$e^{2\pi i(j-l)(n_1/P+(\mu+\sigma\nu+M/2)/M)} = e^{2\pi i(j-l)(n_2/P+\mu/M)} \tag{3.17}$$

for all $j = 1, \ldots, \overline{m}$. Thus the corresponding columns of the systems (3.15) are identical. Given the helical pitch P we can identify the fan angles $\alpha^{(p)}$ for which this coincidence will occur by

$$\left|\alpha^{(p)}\right| = \pi \left|\frac{2p - P}{2P}\right|, \qquad p = 1, \ldots, S - 1. \tag{3.18}$$

Then the resulting system will have at most $S + p$ independent columns. A choice of P for which $\alpha^{(p)}$ is near a measured fan angle and $S + p < \overline{m}$ would not be a good choice of helical pitch. Furthermore, any integral pitch P for which $\alpha^{(p)}$ is near a measured fan angle would not be suitable. With this in mind, a choice of P for which $S + p \geq \overline{m}$ for all $\alpha^{(p)}$ near measured fan angles, or an integral choice of P for which no $\alpha^{(p)}$ is near a measured fan angle would be a candidate for preferred helical pitch.

We assume a scanning geometry suitable for medical applications. The object is contained in a cylinder with unit radius, and the source points lie on a circle of radius $r = 3$ about the z-axis. We need only measure rays for fan angles $|\alpha| \leq \arcsin(1/3)$ and may acquire $S = 4$ slices without regard for the cone angle. To identify candidates for preferred pitch, we compute solutions of the systems in (3.15) and corresponding γ's for equally spaced $0 \leq \alpha_\nu \leq \arcsin(1/3)$ and for choices of $1 \leq P \leq 4$ at increments of 0.1.

MATLAB provides two options for solving a system $Ax = y$. The "\" command, $x = A\backslash y$, returns a least squares solution with at most $\overline{m}$ nonzero entries. This method would perform the interpolation using only data from select cosets and ignoring others. For each problem in the collection, however, data from different cosets may be selected. While all of the acquired data may not be used in the interpolation for a particular fan angle α_ν, over the entire fan it may be that data on each coset of H is utilized at least once.

Alternatively, the "pinv" command, $x = \text{pinv}(A) * y$ computes the pseudoinverse and returns the minimal 2-norm solution which potentially utilizes all measured data for each interpolation problem. The definition of the stability factor in (1.24) suggests that we choose the minimal 1-norm solution. By the triangle and

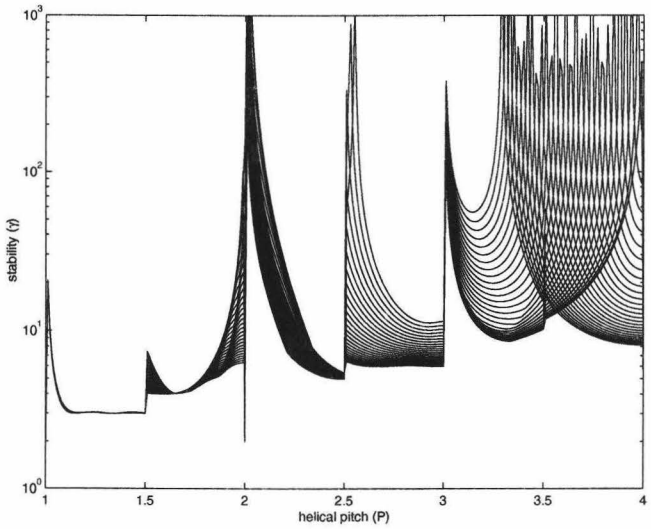

Figure 3.2: Gamma vs. Pitch for $0 \leq \alpha_\nu \leq 7\pi/64$.

Schwarz inequalities for $x \in \mathbb{R}^{2N}$ we have $\|x\|_2 \leq \|x\|_1 \leq \sqrt{2N}\|x\|_2$, so for small N, minimizing the 2-norm will suffice. We choose to use the "pinv" solution. In numerical tests, the two methods produce similar results but the "pinv" solution reduces effects that the "\" command produces by sudden changes in the selected data set.

Each curve in Figure 3.2 gives the amplification factor γ as a function of helical pitch P for 32 equispaced fan angles $0 \leq |\alpha_\nu| \leq \arcsin(1/3)$ in the collection of sampling problems. Values of P for which the curves are low and close together produce sets of stable interpolation and uniform aliasing error over all sampled rays. Sharp peaks and a wide range in the value of γ indicate a choice of P resulting in unstable interpolation for some α_k and a varying aliasing error. The results, particularly the range in values of γ for each choice of helical pitch P, remain the same for more fan angles $0 \leq |\alpha_\nu| \leq \arcsin(1/3)$.

We see that a helical pitch of just less than 2.5 should produce excellent results while helical pitch just less than 3.0 should produce good results. The choice $P \approx 3.15$ may produce good results if $|\hat{g}_{\mu,\nu}(\xi)|$ is small outside of K. In addition we see that a helical pitch near $P = 2$ is a poor choice of helical pitch, as is any choice $P > 3.15$.

3.3 Numerical Results

To test the performance of the interpolation formula (3.16), multislice helical CT data was simulated for a radially uniform cylindrical square wave phantom. The object is composed of a sequences of adjacent discs of alternating density. Each disc has radius 0.95 and width 0.05 in the z-direction. The high and low densities are 1.0 and 0.3 respectively. This is similar to the object used to study longitudinal aliasing in [44] and [20].

We choose a scanning radius of $r = 3$ and compute line integrals for $M = 180$ views per rotation with $S = 4$ parallel slices per view. With the object contained in the unit cylinder and satisfying the conditions in [26] we compute 54 equally spaced rays with $-7\pi/64 \leq \alpha_k < 7\pi/64$. We use a slice thickness $D = 0.0537$. The partial volume effect in the z-direction is modeled by computing, for each ray, the average of 11 line integrals over the span of the slice. Due to this partial volume effect we do not expect to recover the true magnitude of the densities but should be able to identify the positions of the individual discs. In addition we add 1% relative random noise to the computed data. The helical scan covers the entire length of the object.

The reconstruction algorithm is as follows: For each view, $0 \leq \beta_\mu < 2\pi$

1. Use (3.16) to interpolate the values $g(\beta_\mu, \alpha_\nu, z_k)$, $k = 0, \ldots, \overline{k}$, for each α_ν, $\nu = -q, \ldots, q-1$, and obtain one complete fan-beam projection in each reconstruction plane $z = z_k$, $k = 0, \ldots, \overline{k}$.

2. Compute the contribution to the image made by the data $g(\beta_\mu, \alpha_\nu, z_k)$, $\nu = -q, \ldots, q-1$, $k = 0, \ldots, \overline{k}$, using the fan-beam version of the FBP algorithm.

The longitudinal interpolation is performed using reconstruction formula given in (3.16). We refer to this as the PSTI method. For comparison, we also perform a simple linear interpolation (LI) method. Helical scan and reconstruction were performed for helical pitches $P = 2.50$, 3.00, 3.15, and 3.50. The results are displayed in Figures (3.3)-(3.6). For reference we compare the reconstructions from interpolated data to those from measured data using the step and shoot method. As predicted, the data obtained with pitches $P = 2.50$, 3.00, and 3.15 each produce comparably good results in the reconstruction, while the images produced from data obtained with pitch $P = 3.5$ how increased aliasing error.

In the first experiment, we reconstruct the disc phantom from data obtained with helical pitch $P = 2.50$. Figure 3.3(a) shows the sagittal slice through the reconstruction from the data obtained by the PSTI method. Figure 3.3(b) shows the sagittal slice through the reconstruction from the data obtained by the LI method. Figure 3.3c shows the magnitude of the reconstructed function at the center, $\rho = 0$ and figure 3.3d shows the magnitude of the reconstructed function near the edge, $\rho \approx 0.9$. The solid lines correspond to the reconstruction from data obtained using PSTI method and the dotted lines correspond to the reconstruction from data obtained using the LI method. The results from each method are comparably good over the width of the object. Figure 3.3e gives the value of γ for each interpolation problem

over the radius of the object. The low and uniform value indicates that stable interpolation is possible over the scanner field of view. Figure 3.3f gives the l^1-type error in the longitudinal direction in the reconstructions from interpolated data as compared to the step-and-shoot method for both the PSTI and LI methods. Again, the solid line corresponds to the reconstruction from data obtained using PSTI method and the dotted line corresponds to the reconstruction from data obtained using the LI method. As predicted by the value of γ, the error remains nearly uniform over the width of the object.

In the second experiment, we reconstruct the disc phantom from data obtained with helical pitch $P = 3.00$. Figure 3.4(a) shows the sagittal slice through the reconstruction from the data obtained by the PSTI method. Figure 3.4(b) shows the sagittal slice through the reconstruction from the data obtained by the LI method. Figure 3.4c shows the magnitude of the reconstructed function at the center, $\rho = 0$ and figure 3.4d shows the magnitude of the reconstructed function near the edge, $\rho \approx 0.9$. The solid lines correspond to the reconstruction from data obtained using PSTI method and the dotted lines correspond to the reconstruction from data obtained using the LI method. The results from each method are comparably good at the center of the object, while the PSTI method produces superior results near the edge of the object. Figure 3.4e gives the value of γ for each interpolation problem over the radius of the object. The value is low but grows toward the edge of the object, indicating growing instability of the interpolation process nearer the outer edge of the object. Figure 3.4f gives the l^1-type error in the longitudinal direction in the reconstructions from interpolated data as compared to the step-and-shoot method for both the PSTI and LI methods. Again, the solid line corresponds to the reconstruction from data obtained using PSTI method and the dotted line

corresponds to the reconstruction from data obtained using the LI method. The error in the reconstruction using the LI method grows toward the edge of the object while the error in the reconstruction using the PSTI method remains nearly uniform over the width of the object. The increased value of γ does significantly amplify the aliasing error in the PSTI method.

In the third experiment, we reconstruct the disc phantom from data obtained with helical pitch $P = 3.15$. Figure 3.5(a) shows the sagittal slice through the reconstruction from the data obtained by the PSTI method. Figure 3.5(b) shows the sagittal slice through the reconstruction from the data obtained by the LI method. Figure 3.5c shows the magnitude of the reconstructed function at the center, $\rho = 0$ and figure 3.5d shows the magnitude of the reconstructed function near the edge, $\rho \approx 0.9$. The solid lines correspond to the reconstruction from data obtained using PSTI method and the dotted lines correspond to the reconstruction from data obtained using the LI method. The results from each method are comparably good at the center of the object, while the PSTI method produces superior results near the edge of the object. Figure 3.5e gives the value of γ for each interpolation problem over the radius of the object. The value is higher than in this case than for $P = 3.00$ and grows significantly toward the edge of the object, indicating possible instability of the interpolation process nearer the outer edge of the object. Figure 3.5f gives the l^1-type error in the longitudinal direction in the reconstructions from interpolated data as compared to the step-and-shoot method for both the PSTI and LI methods. Again, the solid line corresponds to the reconstruction from data obtained using PSTI method and the dotted line corresponds to the reconstruction from data obtained using the LI method. The error in the reconstruction using the LI method grows sharply toward the edge of the object while the error in the reconstruction using the

PSTI method remains nearly uniform over most of the width of the object, growing larger only at the edge. The value of γ seems to reach a threshold where it begins to significantly amplify the aliasing error in the PSTI method.

In the final experiment, we reconstruct the disc phantom from data obtained with helical pitch $P = 3.50$. This choice of helical pitch is expected to produce poor results. Figure 3.6(a) shows the sagittal slice through the reconstruction from the data obtained by the PSTI method. Figure 3.6(b) shows the sagittal slice through the reconstruction from the data obtained by the LI method. Figure 3.6c shows the magnitude of the reconstructed function at the center, $\rho = 0$ and figure 3.6d shows the magnitude of the reconstructed function near the edge, $\rho \approx 0.9$. The solid lines correspond to the reconstruction from data obtained using PSTI method and the dotted lines correspond to the reconstruction from data obtained using the LI method. The results from each method are comparably good at the center of the object. At the the edge the object, however, the LI method results in reduced resolution while the PSTI method results in catastrophic errors. Figure 3.6e gives the value of γ for each interpolation problem over the radius of the object. The value is higher than in this case than for $P = 3.00$ and grows to a sharp peak near $\rho = 0.67$ before falling again. This indicates an unstable interpolation process in the sampling problems corresponding to α_ν such that $|r \sin \alpha_\nu| \approx 0.67$. Figure 3.6f gives the l^1-type error in the longitudinal direction in the reconstructions from interpolated data as compared to the step-and-shoot method for both the PSTI and LI methods. Again, the solid line corresponds to the reconstruction from data obtained using PSTI method and the dotted line corresponds to the reconstruction from data obtained using the LI method. The error in the reconstruction using the LI method grows until $\rho \approx 0.67$ then levels off or decreases. The error in the

reconstruction using the PSTI method grows extremely large near $\rho = 0.67$ and does not decrease. The catastrophic error in the PSTI method caused by the significantly amplified aliasing error in the interpolation process corresponding to α_ν such that $|r \sin \alpha_\nu| \approx 0.67$ corrupts the reconstruction at all points near or outside the radius $\rho = 0.67$.

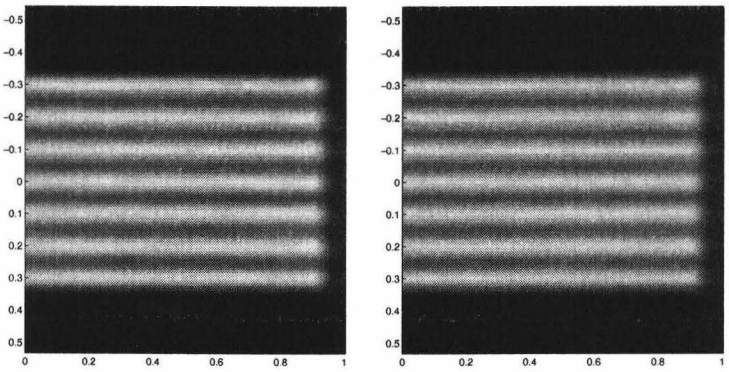

(a) PSTI.

(b) LI.

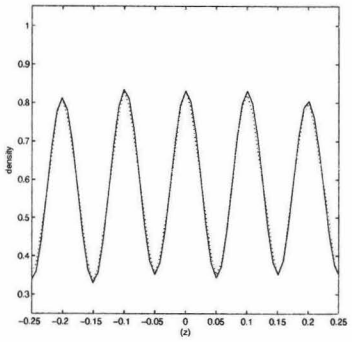

(c) Center.

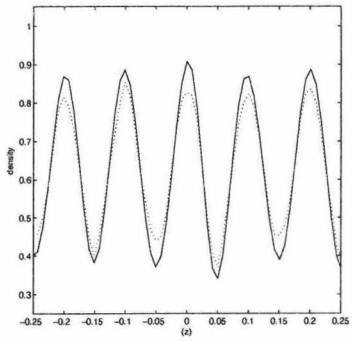

(d) Edge.

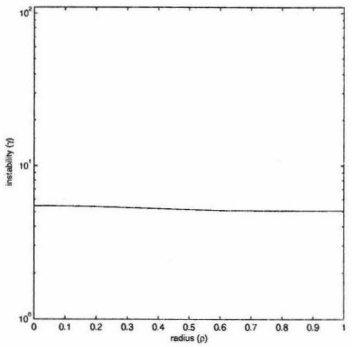

(e) Gamma.

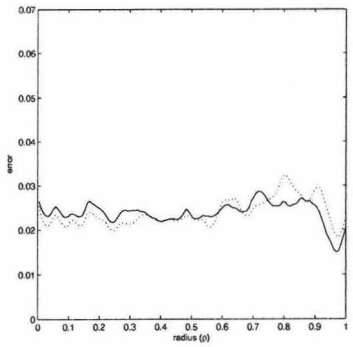

(f) l^1-type Error.

Figure 3.3: Reconstruction of the Disc phantom with $P = 2.50$.

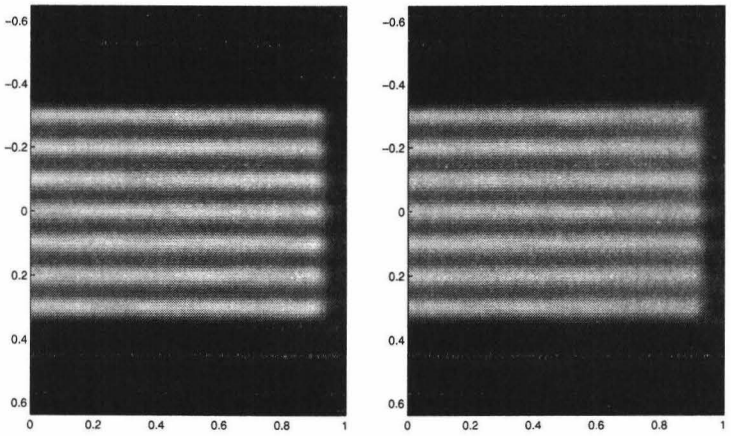

(a) PSTI. (b) LI.

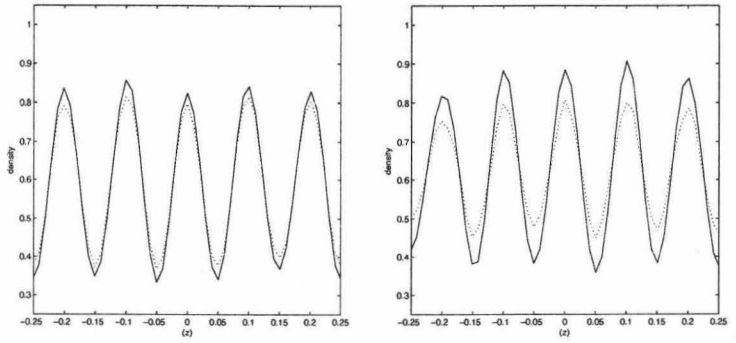

(c) Center. (d) Edge.

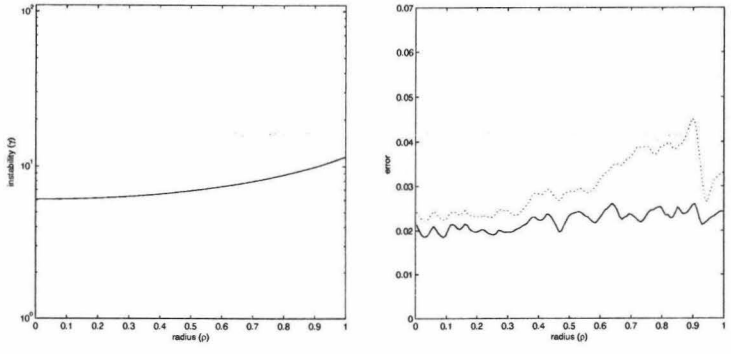

(e) Gamma. (f) l^1-type Error.

Figure 3.4: Reconstruction of the Disc phantom with $P = 3.00$.

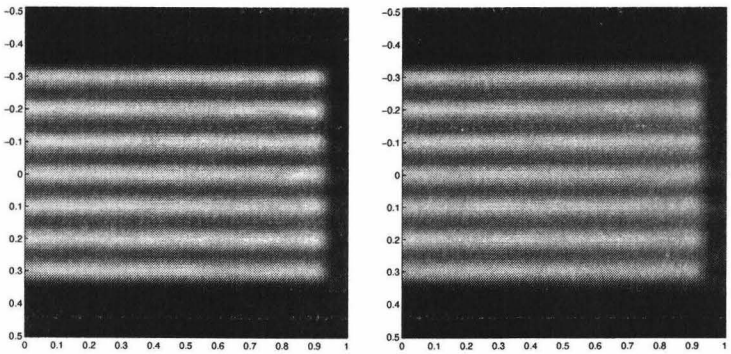

(a) PSTI. (b) LI.

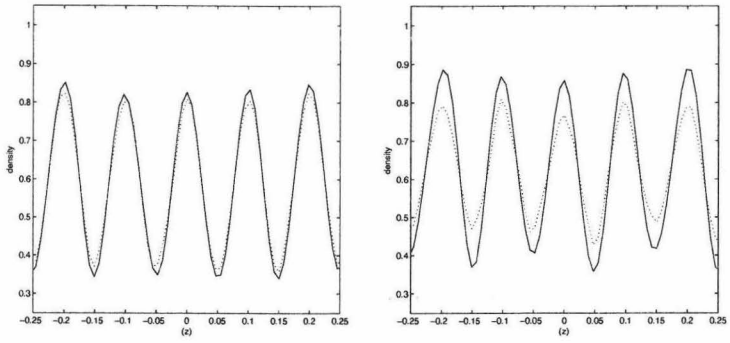

(c) Center. (d) Edge.

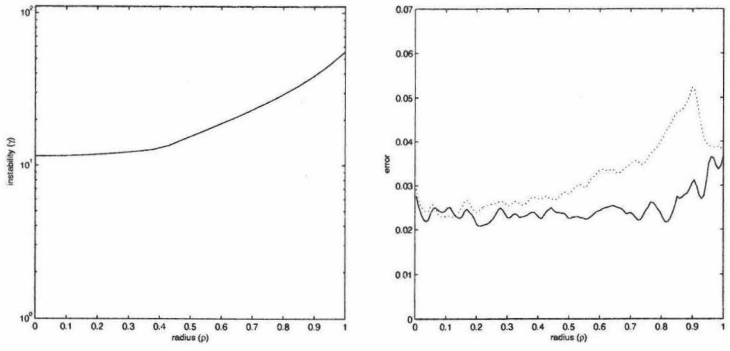

(e) Gamma. (f) l^1-type Error.

Figure 3.5: Reconstruction of the Disc phantom with $P = 3.15$.

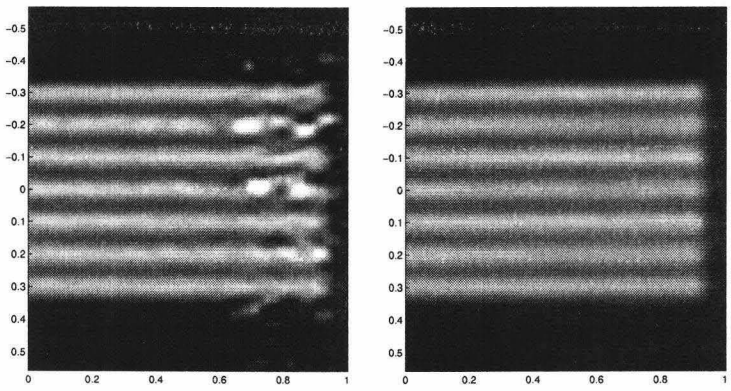

(a) PSTI. (b) LI.

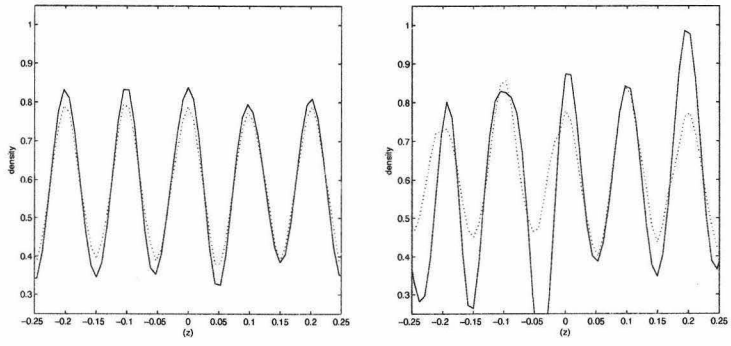

(c) Center. (d) Edge.

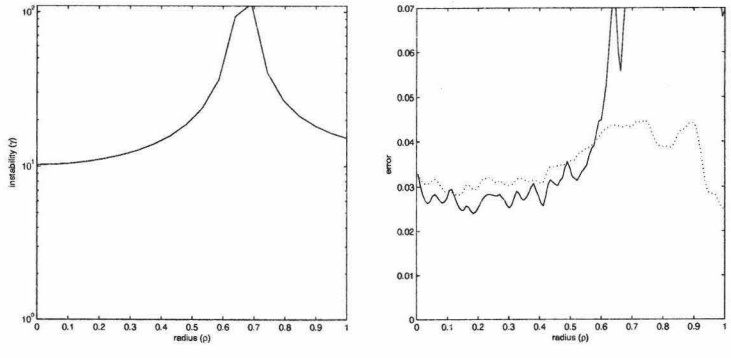

(e) Gamma. (f) l^1-type Error.

Figure 3.6: Reconstruction of the Disc phantom with $P = 3.50$.

4 CONCLUSIONS

We have considered two problems in x-ray computed tomography that involve reconstructing images from nonuniformly sampled data. In each case, the problem arose from an effort to exploit all available information obtained by a sampling scheme devised to satisfy certain physical and practical constraints. We have shown that an appropriate mathematical treatment of the problem allows for the development and application of sampling theorems which permit accurate interpolation as well as theoretical analysis of the outcome.

We showed that, in two-dimensional fan beam computed tomography, the union of the standard sampling set and the reflected sampling set obtained by exploiting the symmetry property forms a nonuniform and generally nonperiodic set. Treating the sampling set as a union of two cosets of different lattices, and applying the theorem of Behmard and Faridani [1], we presented an interpolation algorithm to accurately evaluate the data function on a dense uniform set suitable for the standard reconstruction algorithm. We proved an estimate for the aliasing error committed in the case of non-bandlimited data and showed that the interpolation process is stable for practical applications. We presented numerical evidence of the performance of the interpolation algorithm by reconstructing images with increased resolution from real and simulated data.

We presented the problem of longitudinal interpolation in multislice helical CT as a collection of one-dimensional, nonuniform, but periodic sampling problems. In this framework we shed considerable light on the role of helical pitch in the resolution of the reconstruction and presented an accurate interpolation algorithm

based on the periodic sampling theorem. Using an estimate by Faridani for the aliasing error committed by the interpolation process in the case of nonbandlimited data, we identified the choices of helical pitch $P = 2.50$, $P = 3.00$, and $P = 3.15$ as large values of helical pitch which produce sets of stable interpolation across the scanner field of view, and thus candidates for the preferred helical pitch of a four-slice scanner. Numerical results from simulated data verified the theoretical predictions and supported the commonly accepted value 3.00 as the preferred helical pitch but suggested that a helical pitch of 3.15 may produce comparable results when using the accurate interpolation scheme with data containing a low level of noise.

BIBLIOGRAPHY

1. Behmard H. and Faridani A. (2002) Sampling of Bandlimited Functions on Unions of Shifted Lattices *J. Fourier Anal. Appl.* **8** 43-58

2. Cormack A.M. (1978) Sampling the Radon transform with beams of finite width *Phys. Med. Biol.* **23** 1141-1148

3. Crawford C.R. and King K.F. (1990) Computed tomography scanning with simultaneous patient translation *Med. Phys.* **17** 967-982

4. Desbat L. (1993) Efficient sampling on course grids in tomography *Inverse Problems* **9** 251-269

5. Desbat L., Roux S., Grangeat P. and Koenig A. (2004) Sampling conditions of 3D parallel and fan-beam x-ray CT with applications to helical tomography *Phys. Med. Biol* **49** 2377-2390

6. Faridani A. (1990) An Application of a Multidimensional Sampling Theorem to Computed Tomography *Contemp. Math.* **113** 65-80

7. Faridani A. (1991) Reconstruction from efficiently sampled data in parallel-beam computed tomography *Inverse Problems and Imaging (Pitman Res. Notes Math. Ser.* **245** G.F. Roach (ed.) Longman, London 68-102

8. Faridani A. (1994) A Generalized Sampling Theorem for Locally Compact Abelian Groups *Math. of Comp.* **63** 307-327

9. Faridani A. (1998) Sampling in parallel beam tomography *Inverse Problems, Tomography, and Image Processing* A.G. Ramm (ed.) Plenum, New York 33-53

10. Faridani A. and Ritman E. (2000) High-resolution computed tomography from efficient sampling *Inverse Problems* **16** 635-650

11. Faridani A. (2005) Fan-beam tomography and sampling theory. To appear in *Proc. Symp. in Appl. Math.*

12. Hu H. (1999) Multi-slice Helical CT: Scan and Reconstruction *Med. Phys.* **26** 5-18

13. Izen S.H., Rohler D.P. and Sastry K.L.A. (2005) Exploiting symmetry in fan beam CT: Overcoming third generation undersampling *SIAM J. Appl. Math.* **65** 1027-1052

14. Izen S.H. (2005) An analysis of the fan beam CT reconstruction kernel, talk presented at the Special Session on Radon Transform and Inverse Problems, AMS National Meeting, Atlanta, January 2005

15. Kak A.C. and Slaney M. (1988) *Principles of Computerized Tomographic Imaging* (New York: IEEE Press)

16. Kalender W.A., Seissler W., Klotz E. and Vock P. (1990) Spiral volumetric CT with single-breath-hold technique, continuous transport, and continuous scanner rotation *Radiology* **176** 181-183

17. Kluvánek I. (1965) Sampling theorem in abstract harmonic analysis *Mat. Casopis Sloven. Akad. Vied* **15** 43-48

18. Kohlenberg A. (1953) Exact interpolation of bandlimited functions *J. Appl. Phys.* **24** 1432-1436

19. La Rivière P.J. and Pan X. (2000) Longitudinal Sampling and Aliasing in Multi-slice Helical CT *Proc. IEEE Nuc. Sci. Symp. Med. Imag. Conf.* **2** 15_79-15_83

20. La Rivière P.J. and Pan X. (2002) Pitch Dependence of Longitudinal Sampling and Aliasing Effects in Multi-slice Helical Computed Tomography (CT) *Med. Phys. Biol.* **47** 2797-2810

21. La Rivière P.J. and Pan X. (2002) Longitudinal aliasing in multislice helical computed tomography: sampling and cone-beam effects in *IEEE Trans. Med. Imag.* **21** 1366-1373

22. Marks II R.J. (1991) *Introduction to Shannon Sampling and Interpolation Theory* Springer, New York

23. Marks II R.J. (ed.) (1993) *Advanced Topics in Shannon Sampling and Interpolation Theory* Springer, New York

24. Mitchell N.E. (2005) Multi-dimensional sampling in fan beam tomography M.A. Thesis, Dept. of Mathematics, Oregon State University, Corvallis, OR 97331

25. Natterer F. (1986) *The Mathematics of Computerized Tomography* Wiley, New York

26. Natterer F. (1993) Sampling in fan-beam tomography *SIAM J. Appl. Math.* **53** 358-380

27. Natterer F. (1998) Sampling of Functions with Symmetries (preprint) `http://wwwmath1.uni-muenster.de/num/Preprints/1999/natterer_1`

28. Natterer F. and Wübbeling F. (2001) *Mathematical Methods in Image Reconstruction* SIAM, Philadelphia

29. Natterer F., Cheney M. and Borden B. (2003) Resolution for radar and x-ray tomography *Inverse Problems* **19** S55-S63

30. Palamodov V.P. (1995) Localization of harmonic decomposition of the Radon transform *Inverse Problems* **11** 1025-1030

31. Papoulis A. (1977) Generalized sampling expansion *IEEE Trans. Circuits Syst.* **CAS-24** 652-654

32. Petersen D.P. and Middleton D. (1962) Sampling an Reconstruction of Wave-Number-Limited Functions in N-Dimensional Euclidean Spaces *Inform Control* **5** 279-323

33. Rattey P.A. and Lindgren A.G. (1981) Sampling the 2-D Radon transform *IEEE Trans. Acoust. Speech Signal Process.* **29** 994-1002

34. Rowland S.W. (1979) Computer Implementation of Image Reconstruction Formulas *Image Reconstructions from Projections* G.T. Herman (ed.) Springer, New York

35. Rudin W. (1962) *Fourier analysis on groups* Wiley, New York

36. Schaller S., Flohr T., Klingenbeck K., Krause K., Fuchs T. and Kalender W.A. (2000) Spiral Interpolation Algorithm for Multislice Spiral CT - Part I: Theory *IEEE Trans. Med. Imag.* **19** 822-834

37. Shepp L.A. and Logan B.F. (1974) The Fourier reconstruction of a head section *IEEE Trans. Nucl. Sci.* **NS-21** 21-43

38. Sloan I. and Kachoyan P. (1987) Lattice methods for multiple integration: theory, error analysis and examples *SIAM J. Numer. Anal.* **24** 116-128

39. Smith K.T., Solmon D.C., and Wagner S.L. (1977) Practicle and mathematical aspects of the problem of reconstructing a function from radiographs *Bull. AMS*,**83** 1227-1270

40. Taguchi K. and Aradate H. (1998) Algorithm for Image Reconstruction in Multi-slice Helical CT *Med. Phys.* **25** 550-561

41. Walnut D. (1996) Nonperiodic sampling of bandlimited functions on unions of rectangular lattices *J. Fourier Anal. Appl.* **2** 435-452

42. Wang G. and Vannier M.W. (1999) The Effect of Pitch in Multislice Spiral/Helical CT *Med. Phys.* **26** 2648-2653

43. Yen J.L. (1956) On nonuniform sampling of bandwidth-limited signals *IRE Trans. Circuit Theory* **CT-3** 251-257

44. Yen S.Y., Yan C.H., Rubin G.D. and Napel S. (1999) Longitudinal Sampling and Aliasing in Spiral CT *IEEE Trans. Med. Imag.* **18** 43-58

45. Yen S.Y., Rubin G.D. and Napel S. (1999) Spatially Varying Longitudinal Aliasing and Resolution in Spiral Computed Tomography *Med. Phys.* **26** 2617-2625

APPENDIX

The following MATLAB programs were used to generate the numerical results in Chapters 2 and 3.

```
%%%%%%%%%%%%%%%%%%%%%%%%%%%%%%%%%%%%%%%%%%%%%%%%%%%%%%%%%%%%%%%%%%%%%%%%%%%%
%  This programs uses a method based on nonperiodic sampling   %
%  theorem to exploit the symmetry property in fan beam CT.    %
%  Simulated data for the Shepp-Logan phantom is used.         %
%%%%%%%%%%%%%%%%%%%%%%%%%%%%%%%%%%%%%%%%%%%%%%%%%%%%%%%%%%%%%%%%%%%%%%%%%%%%
%
'  (1)  Setup'
%
%  scanning parameters
%
r = 2.868;
rho = 1;
N = 360;
d = 1/4;
tau = 0.99;
theta = rho/(r*tau);
q = ceil(N*asin(1/r)/pi);
alphamax = (pi/N)*q;
Omega = 2*N/r;
%
if theta <= 1/3
    M = ceil(N*4*theta/(1+theta));
elseif (theta>1/3)*(theta<=1/2)
    M = ceil(N*2*theta/(1-theta));
else
    M = ceil(N*6*theta/(1+theta));
end
a = mod(M,N);
%
%  sampling lattices
%
W1 = [[1/M 0];[0 1/N]];
W1p = [[M 0];[0 N]];
W2 = [[1/M -1/N];[0 1/N]];
W2p = [[M 0];[a N]];
x1 = [0 d/N];
x2 = [d/N -d/N];
x3 = x1 + [0 1/(2*N)];
```

```
j = [1:M]'*ones(1,N); j = j(:);
k = ones(M,1)*[1:N];  k = k(:);
%
'  (2)  Measure Data'
%
Df1 = zeros(M,N);
Df8 = zeros(M,2*N);
index1 = N/2+[-q:q-1]+1;
index2 = N+[-2*q:2*q-1]+1;
% Compute Shepp-Logan phantom
p = 5;   noise = 0.001;
Df1(:,index1) = SLphantom(M,q,alphamax,r,d,p,noise);
Df8(:,N+[-2*q:2*q-1]+1)=SLphantom(M,2*q,alphamax,r,2*d,p,noise);
%
'  (3)  Extract Reflected Rays'
%
Df2 = zeros(M,N);
kp = mod(N-k+1,N);
Df2(:) = Df1(j+M*(kp));
%
'  (4)  Interpolate Missing Data'
%
%  define the bandregion K \subset R2 \cup (\eta' + R1)
%
k = [-M:M-1]'*ones(1,4*N);
m = ones(2*M,1)*[-2*N:2*N-1];
%
%  define R1
%
c1 = (-N+a)/M;  c2 = (2*N+a)/M;
chiR1 = (m >= c1*k).*(m > c2*k);
chiR1 = chiR1 + (m <= N + c2*k).*(m < N + c1*k);
chiR1 = chiR1.*(m < N + k/2).*(m >= k/2);
chiR1 = chiR1.*(m <= 2*N + c1*k).*(m < 2*N + c2*k);
chiR1 = chiR1.*(m >= -N + c1*k).*(m > -N + c2*k);
chiR1 = (chiR1 > 0);
%
%  define R2
%
c1 = -N/M;  c2 = 2*N/M;
chiR2 = (m >= c1*k).*(m > c2*k);
```

```
chiR2 = chiR2 + (m <= N + c2*k).*(m < N + c1*k);
chiR2 = chiR2.*(m < N + k/2).*(m >= k/2);
chiR2 = chiR2.*(m <= 2*N + c1*k).*(m < 2*N + c2*k);
chiR2 = chiR2.*(m >= -N + c1*k).*(m > -N + c2*k);
chiR2 = (chiR2 > 0);
%
'  (4.1)  Compute sampled versions from direct rays'
%
g1 = Sg(Df1,M,N,x1,W1,W1p,x3,W1,W1p,chiR2);
g2 = Sg(Df1,M,N,x1,W1,W1p,x2,W2,W2p,chiR2);
%
'  (4.2)  Compute correction function'
%
h = Sg((Df2-g2),M,N,x2,W2,W2p,x3,W1,W1p,chiR1);
%
'  (4.3)  Compute interpolated data'
%
beta = 1/(1-exp(4*pi*i*d));
Df3 = real(g1 + 2*beta*h);
%
'  (5)  Combine Measured and Interpolated Data'
%
Df = zeros(M,2*N);
Df(:,2*[1:N]-1) = Df1;
Df(:,2*[1:N]) = Df3;
%
'  (6)  reconstruct images'
%
P1 = fanFBP3(M,q,alphamax,r,d,Df1(:,index1),N,512,512);
P2 = fanFBP3(M,2*q,alphamax,r,2*d,Df(:,index2),2*N,512,512);
P3 = fanFBP3(M,2*q,alphamax,r,2*d,Df8(:,index2),2*N,512,512);
%
'  (7)  Display Output'
%
x = 2*[0:511]/511-1;
figure(1), colormap gray,
imagesc(x,-x,P1,[1 1.05]), axis image
figure(2), colormap gray,
imagesc(x,-x,P2,[1 1.05]), axis image
figure(3), colormap gray,
imagesc(x,-x,P3,[1 1.05]), axis image
```

```
figure(4)
plot(x,P1(412,:),'k:',x,P2(412,:),'k')
axis([-.25 .25 1.015 1.035])
'  The End'
%
%%%%%%%%%%%%%%%%%%%%%%%%%%%%%%%%%%%%%%%%%%%%%%%%%%%%%%%%%%%%%%%%%%%%%%%%
%  This programs uses a method based on nonperiodic sampling   %
%  theorem to exploit the symmetry property in fan beam CT.    %
%  Real data from SEIMENS test phantom is used.                %
%%%%%%%%%%%%%%%%%%%%%%%%%%%%%%%%%%%%%%%%%%%%%%%%%%%%%%%%%%%%%%%%%%%%%%%%
%
'  (1)  Setup'
%
%  scanning parameters
%
M = 720;
q = 256;
N = 2258;
r = 2.868;
d = 1/4;
alphamax = asin(1/r);
rho = 0.28;
theta = rho/r;
Omega = min(2*N/r,M*(1+theta)/(2*rho));
%
a = M;
%
%  sampling lattices
%
W1 = [[1/M 0];[0 1/N]];
W1p = [[M 0];[0 N]];
W2 = [[1/M -1/N];[0 1/N]];
W2p = [[M 0];[a N]];
x1 = [0 d/N];
x2 = [d/N -d/N];
x3 = x1 + [0 1/(2*N)];
j = [1:M]'*ones(1,N); j = j(:);
k = ones(M,1)*[1:N];  k = k(:);
%
'  (2)  Measure Data'
%
```

```
Df1 = zeros(M,N);
index1 = N/2+[-q:q-1]+1;
index2 = N+[-2*q:2*q-1]+1;
%
% read CT data
%
fid = fopen('phantom2.ctd','r');
G = fread(fid,[512,720],'integer*2');
fclose(fid);
Df1(:,index1) = G';
%
'  (3)  Extract Reflected Rays'
%
Df2 = zeros(M,N);
kp = mod(N-k+1,N);
Df2(:) = Df1(j+M*(kp));
%
'  (4)  Interpolate Missing Data'
%
%  define the bandregion K \subset R2 \cup (\eta' + R1)
%
k = [-M:M-1]'*ones(1,4*N);
m = ones(2*M,1)*[-2*N:2*N-1];
%
%  define R1 = R2 = R
%
chiR = (m < N + k/2).*(m >= k/2);
chiR = chiR.*(k >= -M/2).*(k < M/2);
%
'  (4.1)  Compute sampled versions from direct rays'
%
g1 = Sg(Df1,M,N,x1,W1,W1p,x3,W1,W1p,chiR);
g2 = Sg(Df1,M,N,x1,W1,W1p,x2,W2,W2p,chiR);
%
'  (4.2)  Compute correction function'
%
h = Sg((Df2-g2),M,N,x2,W2,W2p,x3,W1,W1p,chiR);
%
'  (4.3)  Compute interpolated data'
%
beta = 1/(1-exp(4*pi*i*d));
```

```
Df3 = real(g1 + 2*beta*h);
%
'  (5)  Combine Measured and Interpolated Data'
%
Df = zeros(M,2*N);
Df(:,2*[1:N]-1) = Df1;
Df(:,2*[1:N]) = Df3;
%
'  (6)  reconstruct images'
%
P1 = fanFBP3(M,q,alphamax,r,d,Df1(:,index1),N, % remove CR
             512,512,[-.5 .5 -.5 .5],1);
P2 = fanFBP3(M,2*q,alphamax,r,2*d,Df(:,index2),(1.75)*N,
             512,512,[-.5 .5 -.5 .5],1);
P3 = fanFBP3(M,q,alphamax,r,d,Df1(:,index1),N,
             128,128,[0.04 0.08 -.075 -.035],0);
P4 = fanFBP3(M,2*q,alphamax,r,2*d,Df(:,index2),(1.75)*N,
             128,128,[0.04 0.08 -.075 -.035],0);
%
'  (7)  Display Output'
%
x = [0:511]/511-.5;
figure(1), colormap gray,
imagesc(x,x,P1,[1e4 1.6e4]), axis image
figure(2), colormap gray,
imagesc(x,x,P2,[1e4 1.6e4]), axis image
x = 0.04*[0:127]/127+0.04;
y = 0.04*[0:127]/127-0.075;
figure(3), colormap gray,
imagesc(x,y,P3,[1e4 1.6e4]), axis image
figure(4), colormap gray,
imagesc(x,y,P4,[1e4 1.6e4]), axis image
figure(5)
plot(x,P3(64,:),'k:',x,P4(64,:),'k')
axis([0.04 0.08 1.3e4 1.6e4])
%
'  The End'
%
%%%%%%%%%%%%%%%%%%%%%%%%%%%%%%%%%%%%%%%%%%%%%%%%%%%%%%%%%%%%%%%
%  Computes projection data for Shepp-Logan phantom           %
%%%%%%%%%%%%%%%%%%%%%%%%%%%%%%%%%%%%%%%%%%%%%%%%%%%%%%%%%%%%%%%
```

```
%
function Df = SLphantom(M,q,alphamax,r,d,p,noise)
%
w = 1;  %  ratio of detector width to spacing
%
%
%  Specify parameters of ellipses for mathematical phantom.
%  x = vector of x-coordinates of centers
%  y = vector of y-coordinates of centers
%  a = vector of first half axes
%  b = vector of second half axes
%  psi = vector of rotation angles (degrees)
%  rho = vector of densities
%
%  Shepp-Logan phantom
%
x=[0 0 0.22 -0.22 0 0 0 -0.08 0 0.06 0.5538];
y=[0 -0.0184 0 0 0.35 0.1 -0.1 -0.605 -0.605 -0.605 -0.3858];
e1=[0.69 0.6624 0.11 0.16 0.21 0.046 0.046 0.046 0.023 0.023
    0.0333];
e2=[0.92 0.874 0.31 0.41 0.25 0.046 0.046 0.023 0.023 0.046
    0.206];
psi=[0 0 -18 18 0 0 0 0 0 0 -18];
rho=[2 -0.98 -0.02 -0.02 0.01 0.01 0.01 0.01 0.01 0.01 0.03];
psi = pi*psi/180;
%
h = alphamax/q;
alpha = h*([-q:q-1]+d);
%
Df = zeros(M,2*q);
%
c = w*(h/p)*([0:p-1]-(p-1)/2);  %  detectorlets
a = ones(1,p)/p;                %  detector response function
%
for j = 1:M
    j
    beta = 2*pi*(j-1)/M;
    for k = 1:2*q
        t = (j-1)*M + k;
        for l = 1:p
            phi = beta + alpha(k) + c(l) - pi/2;
```

```
            Theta = [cos(phi);sin(phi)];
            s = r*sin(alpha(k) + c(l));
            Df(j,k)=Df(j,k)+a(l)*Rad(Theta,phi,s,x,y,
                                    e1,e2,psi,rho);
        end  %  l-loop
        Df(j,k) = max(0,Df(j,k)+noise*randn/3);  %  add noise
    end  %  k-loop
end  %  j-loop
%
%%%%%%%%%%%%%%%%%%%%%%%%%%%%%%%%%%%%%%%%%%%%%%%%%%%%%%%%%%%%%%%%%%%%%%%%
%  Computes the values of SMf on (x_2 + H_2)                              %
%  where SMf is the version of f sampled on (x_1 + H_1).                  %
%  f(j,k) = f(x_1 + W1*[j-1,k-1]')                                        %
%  SMf(j',k') = SMf(x_2 + W2*[j'-1,k'-1]')                                %
%  R is the selected fundamental domain of H_1^\perp, and                 %
%  chiR is the indicator function of R.                                   %
%  The algorithm is as follows:                                           %
%    (1)  Use fft to compute SMfhat on standard F.D.                      %
%    (2)  Map standard F.D. of H_1^\perp into R                           %
%         and scale SMfhat.                                               %
%    (3)  Map R into standard F.D. of H_2^\perp                           %
%         applying Poisson summation formula.                             %
%    (4)  Use ifft to compute SMf on H_2.                                 %
%%%%%%%%%%%%%%%%%%%%%%%%%%%%%%%%%%%%%%%%%%%%%%%%%%%%%%%%%%%%%%%%%%%%%%%%
function SMf = Sg(f,M,N,x1,W1,W1p,x2,W2,W2p,chiR)
%
%  Compute the Fourier transform on the standard F.D.
%  of H_1^\perp from samples of f on (x1 + H1).
%
m = [0:M-1]'*ones(1,N);  %  standard F.D. of H_1^\perp
n = ones(M,1)*[0:N-1];
E1 = exp(-2*pi*i*(x1(1)*m + x1(2)*n));
E2 = exp(-2*pi*i*W1(1,2)*(m.*n));  % n = k
SMfhat = E1.*fft((E2.*fft(f,[],1)),[],2);
%
%  Map the standard F.D. into R by elements of H_1^\perp
%  and scale the Fourier transform.  Note that if R does not
%  fill F.D. then some information is lost.
%
ghat = zeros(size(chiR));
eta = W1p*[[-1 -1 -1 0 0 0];[-1 0 1 -1 0 1]];
```

```
t1 = [0:M-1]+M+1;
t2 = [0:N-1]+2*N+1;
for j = 1:6
E3=exp(-2*pi*i*dot(x1,eta(:,j)))*chiR(t1+eta(1,j),t2+eta(2,j));
ghat(t1+eta(1,j),t2+eta(2,j)) = E3.*SMfhat;
end
%
%  Map R into standard F.D. by elements of H_2^\perp.
%  Perform Poisson summation as if sampling g on H_2.
%  (redefine m, n, t1, t2, eta and SMfhat)
%
m = [0:M-1]'*ones(1,N);  %  standard F.D. of H_2^\perp
n = ones(M,1)*[0:N-1];
SMfhat = zeros(M,N);
eta = W2p*[[-1 -1 -1 0 0 0];[-1 0 1 -1 0 1]];
t1 = [0:M-1]+M+1;
t2 = [0:N-1]+2*N+1;
for j = 1:6
    E3 = exp(2*pi*i*dot(x2,eta(:,j)));
    SMfhat = SMfhat + E3*ghat(t1+eta(1,j),t2+eta(2,j));
end
%
%  Finally, compute inverse Fourier transform of SMfhat
%
E1 = exp(2*pi*i*(x2(1)*m + x2(2)*n));
E2 = exp(2*pi*i*W2(1,2)*(m.*n));  % n = k
SMf = ifft(E2.*ifft(E1.*SMfhat,[],2),[],1);
%
%%%%%%%%%%%%%%%%%%%%%%%%%%%%%%%%%%%%%%%%%%%%%%%%%%%%%%%%%%%%%%%
%  Computes the reconstruction from fan-beam data               %
%  for MX by MY points in roi.                                  %
%  Uses factor (alpha/sin(alpha))^2 in filter step              %
%  2pi/M = source position increment.                           %
%  alphamax/q = fan angle increment.                            %
%  R = scanning radius (object radius assumed to be 1).         %
%  DF = data, size(DF) = M by 2q.                               %
%  b = bandwidth of filter (standard: b = N).                   %
%  MX by MY = reconstruction grid.                              %
%%%%%%%%%%%%%%%%%%%%%%%%%%%%%%%%%%%%%%%%%%%%%%%%%%%%%%%%%%%%%%%
%
function P = fanFBP3(M,q,alphamax,r,d,DF,b,MX,MY,roi,circle)
```

```
%
if nargin==9
    roi=[-1  1 -1  1]; %roi=[xmin xmax ymin ymax]
                       %region of interest where
                       %reconstruction is computed
    circle = 1; % If circle = 1 image computed only inside
                % circle inscribed in roi.
end
%
if MX > 1
 hx = (roi(2)-roi(1))/(MX-1);
 xrange = roi(1) + hx*[0:MX-1];
else
 hx = 0; xrange = roi(1);
end
%
if MY > 1
 hy = (roi(4)-roi(3))/(MY-1);
 yrange = flipud((roi(3) + hy*[0:MY-1])');
else
 hx = 0; yrange = roi(3);
end
%
center = [(roi(1)+roi(2)), (roi(3)+roi(4))]/2;
x1 = ones(MY,1)*xrange; %x-coordinate matrix
x2 = yrange*ones(1,MX); %y-coordinate matrix
if circle == 1
  re = min([roi(2)-roi(1),roi(4)-roi(3)])/2;
  chi = ((x1-center(1)).^2 + (x2-center(2)).^2 <= re^2);
else
  chi = isfinite(x1);
end
x1 = x1(chi); x2 = x2(chi);
P = zeros(MY,MX);Pchi = P(chi);
%
rps=1/b;
h = alphamax/q;
alpha = h*([-q:q-1]+d);
%bs = b*sin(h*([-2*q:2*q-1]));
bs = b*h*([-2*q:2*q-1]);
wb = slkernel(bs)/(rps^2);   %discrete convolution kernel.
```

```
wb = wb./(sinc(h*([-2*q:2*q-1])/pi).^2);
for j = 1:M
    if (j==2 | mod(j,100)==1)
        j
    end
    beta = 2*pi*(j-1)/M;
    theta = [cos(beta),sin(beta)];
    T = DF(j,:);
    %
    %    convolution
    %
    T = T.*cos(alpha);
    C = conv(T,wb);
    Q = h*C(2*q+1:4*q); Q(2*q+1)=0;
    %
    %    interpolation and backprojection
    %
    Q = [real(Q)'; 0];
    a = r*theta;    % source position vector
    d1 = a(1)-x1;  d2 = a(2)-x2;       % (d1,d2) = a-x
    t = real(acos((d1*a(1)+d2*a(2))./  %  remove CR
               (r*abs(sqrt(d1.^2+d2.^2)))));
    t = t.*(ones(size(x1))-2*((x2*a(1)-x1*a(2))>0));% sign conv.
    %
    k1 = floor(t/h-d);
    u = (t/h-d-k1);
    k = max(1,k1+q+1); k = min(k,2*q);
    Pupdate = ((1-u).*Q(k)+u.*Q(k+1))./(d1.^2+d2.^2);
    Pchi = Pchi + Pupdate;
    %
end   % j-loop
%
P(chi) = Pchi*r*(2*pi/M);
P = real(P);
%
%%%%%%%%%%%%%%%%%%%%%%%%%%%%%%%%%%%%%%%%%%%%%%%%%%%%%%%%%%%%%%%%%
%  This function computes the Radon transform of ellipses       %
%  centered at (x,y) with major axis u, minor axis v,           %
%  rotated through angle alpha, with weight rho.                %
%%%%%%%%%%%%%%%%%%%%%%%%%%%%%%%%%%%%%%%%%%%%%%%%%%%%%%%%%%%%%%%%%
%
```

```
function [RF] = Rad(theta,phi,s,x,y,u,v,psi,rho)
%
RF = zeros(size(s));
for mu = 1:max(size(x))
   a = (u(mu)*cos(phi-psi(mu)))^2+(v(mu)*sin(phi-psi(mu)))^2;
   test = a-(s-[x(mu);y(mu)]'*theta).^2;
   ind = test>0;
   RF(ind) = RF(ind)+rho(mu)*(2*u(mu)*v(mu)*sqrt(test(ind)))/a;
end  % mu-loop
%
%%%%%%%%%%%%%%%%%%%%%%%%%%%%%%%%%%%%%%%%%%%%%%%%%%%%%%%%%%%%%%%%
%  Shepp-Logan convolution kernel                              %
%%%%%%%%%%%%%%%%%%%%%%%%%%%%%%%%%%%%%%%%%%%%%%%%%%%%%%%%%%%%%%%%
%
function u = slkernel(t)
%
u = zeros(size(t));
i1 = abs(abs(t)-pi/2)<=1.e-6;
u(i1) = ones(size(u(i1)))/pi;
t1 = t(abs(abs(t)-pi/2)>1.e-6);
v = (pi/2 - t1.*sin(t1))./((pi/2)^2 - t1.^2);
u(abs(abs(t)-pi/2)>1.e-6) = v;
u = u/(2*pi^3);
```

```
%%%%%%%%%%%%%%%%%%%%%%%%%%%%%%%%%%%%%%%%%%%%%%%%%%%%%%%%%%%%%%%%%
% This program computes helical CT data for a DISC phantom,      %
% interpolates the data in the standard, step-and-shoot,         %
% sampling scheme, and reconstructs the image slice by slice     %
% using FBP Algorithm.                                            %
%%%%%%%%%%%%%%%%%%%%%%%%%%%%%%%%%%%%%%%%%%%%%%%%%%%%%%%%%%%%%%%%%
%
N = 4;      % # of slices
M = 180;    % # views per rotation
P = 3.5;    % helical pitch
R = 3;      % scanning radius (object radius assumed 1)
%
phi = 2*pi/M*[0:M-1];         % source angles
alphamax = asin(1/R);
q = floor(M*alphamax/pi);     % # of measured rays
D = R*alphamax/q;                 % slice thickness
alpha = alphamax/q*[-q:q-1];    % measured rays
r = R*sin(alpha);
%
MX = 256;  % reconstruction grid MX by MY by MZ
MY = 3;
MZ = 128;
roi = [-1 1 -1 1 -.5 .5];  % region of interest
circle = 1;
%
Fsbs = zeros(MY,MX,MZ);
Flin = zeros(MY,MX,MZ);
Fpst = zeros(MY,MX,MZ);
%
b = 2*pi/D;
d = P*D;
h1 = floor(roi(5)/d);
h2 = floor(roi(6)/d);
H = d*[h1:h2];
zn = D*[0:N-1];
%
t = d*length(H)/MZ;
x3 = d*h1 + t*[0:MZ-1];
%
```

```
Gsbs = zeros(MZ,length(alpha));
Glin = zeros(MZ,length(alpha));
Gpst = zeros(MZ,length(alpha));
gamma = zeros(size(alpha));
%
for j = 0:M-1;
    j
    beta = j*2*pi/M;
    for k = 1:length(alpha)
        dz = d*(pi-2*alpha(k))/(2*pi);
        z = [zn,zn+dz] + d*j/M;
        z = mod(z,d);
        Z = ones(2*N,1)*H + (z')*ones(size(H));
        %
        %  Compute data
        %
        Gsbs(:,k) = DiscScan(x3',R,D,alpha(k));  %slice-by-slice
        %
        g = DiscScan(Z,R,D,alpha(k));   %  helical
        %
        %  Interpolate
        %
        Glin(:,k) = LINint(g,Z,x3);   %  LI
        %
        [Gpst(:,k),gamma(k)] = PST1Dint(g',d,z,1/D,x3');%  PSTI
        %
    end  %  k-loop
    %
    Gpst = real(Gpst);
    %
    %  Reconstruction Update
    %
    for l = 1:MZ
        %
        P=DivFBPup(beta,q,alphamax,R,Gsbs(l,:),MX,MY,roi(1:4));
        Fsbs(:,:,l) = Fsbs(:,:,l) + P;
        P=DivFBPup(beta,q,alphamax,R,Glin(l,:),MX,MY,roi(1:4));
        Flin(:,:,l) = Flin(:,:,l) + P;
        P=DivFBPup(beta,q,alphamax,R,Gpst(l,:),MX,MY,roi(1:4));
        Fpst(:,:,l) = Fpst(:,:,l) + P;
        %
```

```
    end  %  l-loop
    %
end  %  j-loop
%
Fsbs = real(Fsbs)*R*2*pi/M;
Flin = real(Flin)*R*2*pi/M;
Fpst = real(Fpst)*R*2*pi/M;
%
%  Display output
%
hx = (roi(2)-roi(1))/(MX-1);
x1 = roi(1) + hx*[0:MX-1];
C = find(x1>=0);
%
Tsbs = zeros(length(C),MZ);
Tlin = zeros(length(C),MZ);
Tpst = zeros(length(C),MZ);
%
Temp = Fsbs(2,C,:);
Tsbs(:) = Temp(:);
Tsbs = Tsbs';
Temp = Flin(2,C,:);
Tlin(:) = Temp(:);
Tlin = Tlin';
Temp = Fpst(2,C,:);
Tpst(:) = Temp(:);
Tpst = Tpst';
ERRlin = sum(abs(Tlin-Tsbs))/MZ;
ERRpst = sum(abs(Tpst-Tsbs))/MZ;
%
figure(1)
imagesc(x1(C),x3,Tpst,[0 1])
colormap gray
axis image, %axis off
%
figure(2)
imagesc(x1(C),x3,Tlin,[0 1])
colormap gray
axis image, %axis off
%
figure(3)
```

```
plot(x3,Tpst(:,1),'k',x3,Tlin(:,1),'k:')
axis([-.25 .25 0.25 1.05])
xlabel('(z)')
ylabel('density')
axis square
%
t = find(x1(C)<=0.9);
t = max(t);
figure(4)
plot(x3,Tpst(:,t),'k',x3,Tlin(:,t),'k:')
axis([-.25 .25 0.25 1.05])
xlabel('(z)')
ylabel('density')
axis square
%
t=find(r<=0);
figure(5)
semilogy(-r(t),gamma(t),'k')
axis([0 1 1 110])
xlabel('radius (\rho)')
ylabel('instability (\gamma)')
axis square
%
figure(6)
plot(x1(C),ERRpst,'k',x1(C),ERRlin,'k:')
axis([0 1 0 .07])
xlabel('radius (\rho)')
ylabel('error')
%legend('PSTI','LI')
axis square
%
%%%%%%%%%%%%%%%%%%%%%%%%%%%%%%%%%%%%%%%%%%%%%%%%%%%%%%%%%%%%%
%  Computes x-ray transform of disc phantom for rays        %
%  with direction \alpha and positions Z.  Rays are         %
%  then averaged over slice thickness D.                    %
%%%%%%%%%%%%%%%%%%%%%%%%%%%%%%%%%%%%%%%%%%%%%%%%%%%%%%%%%%%%%
%
function g = DiscScan(Z,R,D,alpha)
%
r = .95;             % radius
w = 0.05;            % width and separation
```

```
c = 2*w*[-3:3];     % centers
d1 = 0.3;
d2 = 0.7;      % densities
%
g = zeros(size(Z));
s = 5;
t = D/2*([-s:s-1]+.5)/s;
T = Z(:)*ones(size(t)) + ones(size(Z(:)))*t;
G = zeros(size(T));
G = d1*(T>=(min(c)-w/2)).*(T<(max(c)+w/2));
for j = 1:length(c)
    G = G + d2*((T-c(j))>=(-w/2)).*((T-c(j))<(w/2));
end
g(:) = sum(G,2)/(2*s+1);
g = g*2*sqrt(r^2-(R*sin(alpha))^2)*(abs(sin(alpha))<=r/R);
noise = 2*r*(d1+d2)*(1e-2)*randn(size(g));
g = g + noise;
%
%%%%%%%%%%%%%%%%%%%%%%%%%%%%%%%%%%%%%%%%%%%%%%%%%%%%%%%%%%%%%
%  This program performs Liner Interpolation of data        %
%%%%%%%%%%%%%%%%%%%%%%%%%%%%%%%%%%%%%%%%%%%%%%%%%%%%%%%%%%%%%
%
function Sf = LINint(f,x,z)
%
x = x(:);  f = f(:);
Z = x*ones(size(z)) - ones(size(x))*z;
%  Locate nearest lower data pt. (may be more than one)
M1 = -Z.*(Z<=0) + 100*(Z>0);
v = min(M1);  V = ones(size(x))*v;
I1 = (M1==V);
s = sum(I1);  S = ones(size(x))*(1./s);  %  Duplicity
I1 = I1.*S;
%  Locate nearest higher data pt. (may be more than one)
M2 = Z.*(Z>0) + 100*(Z<=0);
v = min(M2);  V = ones(size(x))*v;
I2 = (M2==V);
s = sum(I2);  S = ones(size(x))*(1./s);  %  Duplicity
I2 = I2.*S;
%  Calculate weights
c = sum((M2.*I2)+(M1.*I1));  C = ones(size(x))*c;
C1 = ones(size(I1)).*I1 - (M1.*I1)./C;
```

```
C2 = ones(size(I2)).*I2 - (M2.*I2)./C;
%  Interpolate
Sf = (C1'+C2')*f;
%
%%%%%%%%%%%%%%%%%%%%%%%%%%%%%%%%%%%%%%%%%%%%%%%%%%%%%%%%%%%%%%%%
%  1-D interpolation based on periodic sampling theorem        %
%%%%%%%%%%%%%%%%%%%%%%%%%%%%%%%%%%%%%%%%%%%%%%%%%%%%%%%%%%%%%%%%
%
function [g,gamma] = PST1Dint(f,h,x,b,z)
%
% f = function values on (x+H).
% h = lattice spacing H = hZ.
% x = coset shifts.
% b = assumed bandwidth of f.
% z = location of interpolated values f(z).
% Must have length(z) > size(f,1).
%
N1 = size(f,1);
N2 = length(z);
M = ceil(2*b*h);
K = [-N2/2:N2/2-1]'/(h*N1);
w = 2*pi/(h*N1);
mu = zeros(1,2*M-1);
%
ghat = zeros(size(K));
fhat = (1/N1)*fft(f,[],1);
fhat = fftshift(fhat,1);
%
for l = 1:M
    d = zeros(M,1); d(l) = 1;
    eta = (1/h)*(l-1-[0:M-1]');
    A = exp(-i*2*pi*eta*x);
    beta = pinv(A)*d;
    Kl = (K >= -b + (l-1)/h).*(K < b + (l-M)/h);
    index = find(Kl);
    if (1 - isempty(index))
        c = mod(N1,2);
        t = (1-c)*floor((N2-N1)/2) + c*ceil((N2-N1)/2);
        temp = mod(index-1-t,N1)+1;
        T = exp(-i*2*pi*K(index)*x);
        ghat(index) = (fhat(temp,:).*T)*beta;
```

```
    end  %  if
    mu(l) = sum(abs(beta));
end  %  l-loop
%
for l = M+1:2*M-1;
    d = zeros(M-1,1); d(l-M) = 1;
    eta = (1/h)*(l-1-M-[0:M-2]');
    A = exp(-i*2*pi*eta*x);
    beta = pinv(A)*d;
    Kl = (K >= b + (l-2*M)/h).*(K < -b + (l-M)/h);
    index = find(Kl);
    if (1-isempty(index))
        c = mod(N1,2);
        t = (1-c)*floor((N2-N1)/2) + c*ceil((N2-N1)/2);
        temp = mod(index-1-t,N1)+1;
        T = exp(-i*2*pi*K(index)*x);
        ghat(index) = (fhat(temp,:).*T)*beta;
    end  %  if
    mu(l) = sum(abs(beta));
end  %  l-loop
%
ghat = fftshift(ghat,1);
g = real(ifft(N2*ghat));
gamma = M*max(mu);
%
%%%%%%%%%%%%%%%%%%%%%%%%%%%%%%%%%%%%%%%%%%%%%%%%%%%%%%%%%%%%%%%%
%  Singe step of Divergent-Beam FBP Algorithm                  %
%%%%%%%%%%%%%%%%%%%%%%%%%%%%%%%%%%%%%%%%%%%%%%%%%%%%%%%%%%%%%%%%
%
function P = DivFBPup(phi,q,alphamax,R,Df,MX,MY,roi)
%  G = Divergent-Beam CT Data,
%      size(G) = [length(phi),length(alpha)],
%              = [p,2q],
%  phi = source positions,
%  alpha = fan angles,
%  R = scanning radius,
%  MX = number of columns in image,
%  MY = number of rows in image.
%  NOTE:  It is assumed that the object is contained in
%        the unit circle and that alpha = asin(1/R)/q*[-q:q-1].
%  roi=[-1  1 -1  1]; %roi=[xmin xmax ymin ymax]
```

```
%                       %region of interest where
%                       %reconstruction is computed
circle = 1; % If circle = 1 image computed only inside
%           % circle inscribed in roi.
%
if MX > 1
 hx = (roi(2)-roi(1))/(MX-1);
 xrange = roi(1) + hx*[0:MX-1];
else
 hx = 0; xrange = roi(1);
end
%
if MY > 1
 hy = (roi(4)-roi(3))/(MY-1);
 yrange = flipud((roi(3) + hy*[0:MY-1])');
else
 hx = 0; yrange = roi(3);
end
%
center = [(roi(1)+roi(2)), (roi(3)+roi(4))]/2;
x1 = ones(MY,1)*xrange; %x-coordinate matrix
x2 = yrange*ones(1,MX); %y-coordinate matrix
if circle == 1
  re = min([roi(2)-roi(1),roi(4)-roi(3)])/2;
  chi = ((x1-center(1)).^2 + (x2-center(2)).^2 <= re^2);
else
  chi = isfinite(x1);
end
x1 = x1(chi); x2 = x2(chi);
%
b = pi*q/asin(1/R);
rps=1/b;
h = alphamax/q;
alpha = h*[-q:q-1];
%bs = b*sin(h*([-2*q:2*q-1]));
bs = b*h*([-2*q:2*q-1]);
wb = slkernel(bs)/(rps^2);   %discrete convolution kernel.
wb = wb./(sinc(h*([-2*q:2*q-1])/pi).^2);
%
P = zeros(MY,MX);  Pchi = P(chi);
theta = [cos(phi);sin(phi)];
```

```
%
%    convolution
%
Df = Df.*cos(alpha);
C = conv(Df,wb);
Q = h*C(2*q+1:4*q); Q(2*q+1)=0;
%
%    interpolation and backprojection
%
Q = [real(Q)'; 0];
a = R*theta;    % source position vector
d1 = a(1)-x1;  d2 = a(2)-x2;     % (d1,d2) = a-x
t = acos((d1*a(1)+d2*a(2))./(R*abs(sqrt(d1.^2+d2.^2))));
t = t.*(ones(size(x1))-2*((x2*a(1)-x1*a(2))<0));
k1 = floor(t/h);
u = (t/h-k1);
k = max(1,k1+q+1);  k = min(k,2*q);  k = real(k);
Pupdate = ((1-u).*Q(k)+u.*Q(k+1))./(d1.^2+d2.^2);
Pchi = Pchi + Pupdate;
%
P(chi) = Pchi;
P = real(P);
```